GENERAL MOTORS CORPORATION

SUMMARY REPORT OF

RESEARCH ON THE PROPERTIES
OF OPTIMUM METEOROID SHIELDS

N 65-33856

(ACCESSION NUMBER)	(THRU)
/08	
(PAGES)	(CODE)
CR-64934	32
(NASA CR OR TMX OR AD NUMBER)	(CATEGORY)

FACILITY FORM 602

GM DEFENSE RESEARCH LABORATORIES

SANTA BARBARA, CALIFORNIA

⊗

AEROSPACE OPERATIONS DEPARTMENT

TR64-48
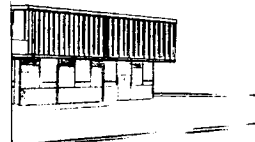
SEPTEMBER 1964

Rqt 29474

GENERAL MOTORS CORPORATION

SUMMARY REPORT OF

RESEARCH ON THE PROPERTIES OF OPTIMUM METEOROID SHIELDS

Prepared for
GEORGE C. MARSHALL SPACE FLIGHT CENTER
Huntsville, Alabama
CONTRACT NO. NAS8-11118

Principal Investigators
C.L. Meyers
J.A. Charest

Research Managers
J.W. Gehring
C.J. Maiden

GM DEFENSE RESEARCH LABORATORIES

SANTA BARBARA, CALIFORNIA

AEROSPACE OPERATIONS DEPARTMENT

TR64-48   SEPTEMBER 1964

TR64-48

ABSTRACT

Detailed diagnostic techniques have been applied to the direct measurement of the parameters associated with a more complete understanding of the impact-cratering process. Experimental studies have been conducted on the measurement of shock-pressure maximum amplitudes, on the measurement of momentum transfer, and on a phenomenological model of crater formation.

The phenomenological model of crater formation has been divided into four regimes: 1) the initial transient regime of cratering, including impact flash; 2) the primary penetration regime of cratering covering the period in which the projectile acts on the target as a causative force; 3) the cavitation regime of cratering covering the period during which the pressure on the crater surface decreases to a value giving maximum cratering dimensions; and lastly, the recovery regime of cratering, including surface spallation and release of pressure on the crater walls. This report presents detailed experimental data covering the last three of the four regimes described above; in each case the data are directly related to the extent to which it contributes to the cratering process and to the relationship of this portion of the phenomena to the theoretical models of impact cratering.

The experimental results, which represent only nine months effort on a program which was originally planned for twenty-four months, have been organized into three separate discussions of the principal topical areas studied: shock-pressure measurements; momentum-transfer (with mass-loss) measurements; and crater-growth measurements. In addition, the materials (physical, mechanical and metallurgical properties) and the experimental equipment used (generally common to each of the above topical areas) are described in appendixes to the report.

CONTENTS

TR64-48

ILLUSTRATIONS

TR64-48

TABLES

TR64-48

INTRODUCTION

An understanding of hypervelocity impact phenomena is most desirable due to the hazard presented by the impact of meteoroids on space vehicles. Although a vast amount of experimental information has been obtained, it is felt that no completely adequate empirical or theoretical model has been formulated from which a complex space vehicle hull can be designed to afford reliable protection against this hazard.

An earlier paper[1]* presented a phenomenological model of hypervelocity impact which has been extended in the present report. A recent study conducted for the NASA by GM Defense Research Laboratories,[2] in which more than 300 references were reviewed, attempted to present a broad analysis of the phenomena of hypervelocity impact. The hypervelocity impact "hazard, " especially as it concerns meteoroids, was treated in enough detail to show that it warrants special attention by the vehicle designer. The lack of accurate, quantitative data on the mass and velocity distribution of meteoroids near Earth and in interplanetary space was emphasized. In fact, very recent estimates of average meteoroid density (0.44 gm/cm^3) and mean velocity (22 km/sec) by Whipple[3] illustrated the continuous revisions that are being made of the meteoroid environment by the many investigators in the field. The trend in recent years has been to lower the mass frequency distribution curves, i. e. , to subordinate the meteoroid hazard, especially in cislunar and interplanetary space.

The impact hazard is far from being eliminated, however, not only with respect to meteoroids but in military applications of hypervelocity projectiles. Accordingly, a method was presented in the NASA report for determining how thick a

---

* Raised numbers in parentheses indicate references listed at the end of this report.

TR64-48

vehicle skin must be in order to prevent perforation by a hypervelocity pro-
jectile under given impact conditions, even though estimates of the meteoroid
hazard and of mission requirements may change. It should be emphasized,
however, that the example considered in that report was for an _elemental_
single-skin hull of homogenous material. Practical applications to structures
more representative of actual spacecraft would require consideration of factors
such as spall, multiple-sheet targets, laminates, pressure vessels, etc. These
require the use of different penetration laws, derived either experimentally or
theoretically, to account for the behavior of complex targets under conditions
of hypervelocity impact.

The more basic problem of hypervelocity impact into semi-infinite targets was
treated in more detail, both empirically and theoretically, in the NASA report.
The reasonable accuracy with which some investigators have been able to pre-
dict impact damage was illustrated. Extrapolation of the wealth of experimental
data available for velocities below 10 km/sec into the meteoroid range (11 − 72
km/sec) is possible, and some estimates of damage can be made with reason-
able assurance. However, experimental data in the velocity range of 10 − 40
km/sec would greatly improve the accuracy of these estimates.

The referenced theoretical treatment of hypervelocity impact has described the
basic mechanisms involved and has reviewed several of the models and methods
used in describing and analyzing hypervelocity cratering. These include hydro-
dynamic theory, visco-plastic theory, explosion theory, and blast-wave analysis.
The influence of such variables as strength, density, wave velocity, crystal
structure, anisotropy, ductility, and, of course, impact velocity was considered.
During the course of this work, however, it became apparent that although there
is a general understanding of the basics involved in hypervelocity impact, there
is a decided lack of detailed knowledge concerning such specifics as impact
radiation, target strength effects, projectile density effects, and elastic-plastic
deformation including high-strain-rate properties of materials.

2

One of the mechanical properties of materials that has been useful in analyzing impact damage to thick targets is hardness, and in particular, the Brinell hardness number. Cratering efficiency in terms of projectile energy/unit crater volume has been found to be directly proportional to target hardness in a wide range of materials and values of hardness. For a given target material, crater volume has been found to increase with target temperature in a manner related to decreases in target hardness and to material phase changes.

Although the original report concentrated on materials, properties, and shapes of targets, the projectile is also of interest. In the case of meteoroid impacts where impact velocities can be expected to be in the range of 11 – 72 km/sec, both the density and shape of the meteoroid may be unimportant since the shape will probably be approximately spherical. Meteoroid density may also be unimportant; however, because of the wide range of meteoroid density estimates (0.05 to 8.0 gm/cm^3), and the lack of quantitative data on projectile density effects on meteoroid velocities, an evaluation of the meteoroid hazard should make allowance for possible effects of density. From the military standpoint, where impact velocities could range from 1 to 12 km/sec, projectile shape and density are important enough in some cases to be the controlling factor in impact damage. Obviously, projectile mass is significant in all cases.

From the review of hypervelocity impact information made in conjunction with the previous report, it became apparent that many aspects of the problem are being investigated. Several organizations are carrying out extensive research programs which cover such areas as multiple-sheet targets, impact radiation, theoretical models, and specific materials and structures (including space radiators, laminates, pressure vessels, simulated lunar materials, and filler materials). Studies directed at more specific areas, such as reentry materials, ablatives, thin targets, and cratering theory, are being made by many other organizations.

As a result of the recommendations made in Reference 2, a basic research program was undertaken to develop a more thorough understanding of the properties of materials under the exceedingly high strain rates associated with

TR64-48

hypervelocity impact. This program included the effect of material strength on crater formation in various metals, and the importance of material strength to the decay of shock waves. The experimental data on crater formation derived from this program have been interpreted in the light of the previously proposed phenomenological model, which is reviewed in the next section.

MODEL OF CRATER FORMATION IN SEMI-INFINITE TARGETS

First Regime of Impact Cratering

A model evolved from the combined theoretical and experimental studies of many researchers [4-15] is illustrated schematically (as impact pressure vs time after impact) in Figure 1. The process is dynamically illustrated (Figure 2) with selected frames of a Beckman & Whitley framing-camera record of the impact of a projectile on an aluminum target. The projectile can be seen approaching the target at a velocity greatly in excess of the wave-propagation velocity in either the impacting particle or the target material. Immediately after the projectile's contact with the target material, the first regime or transient state begins (in which the pressure at the interface pertains to a plain one-dimensional impact). For the case of a flat-ended projectile this transient regime is extremely brief, possibly as short as 10^{-9} seconds (the time required to move a dislocation). On the other hand, for the case of impact of a sphere, this transient regime lasts at least as long as it takes the sphere to penetrate to a depth equal to the diameter of the sphere.

The plot shown in Figure 1, in which the pressure is noted as a function of time after impact, is certainly an exaggerated view of the time scale. Characteristically, Regime 1 will last for a period of less than a microsecond for most impact cases. It has been suggested that a pressure spike could exist during the establishment of the steady-state Hugoniot conditions of Regime 2, if one considers certain materials on a microscopic scale. This consideration implies that, prior to the establishment of the steady-state regime, one should consider the density and the compressibility of individual elements of the total target; that is, not merely considering the bulk density or bulk compressibility of the entire target material.

4
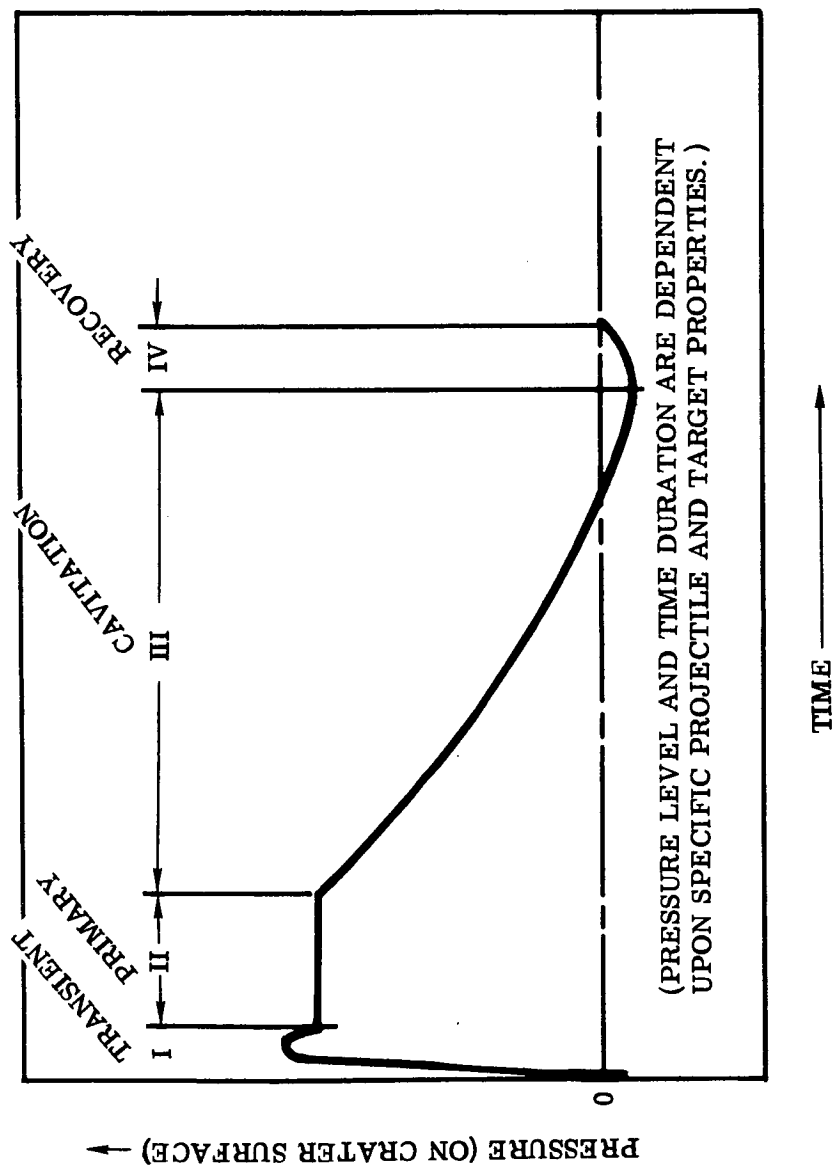
Figure 1 Impact Cratering Regimes on a Pressure-Time Basis

TR64-48
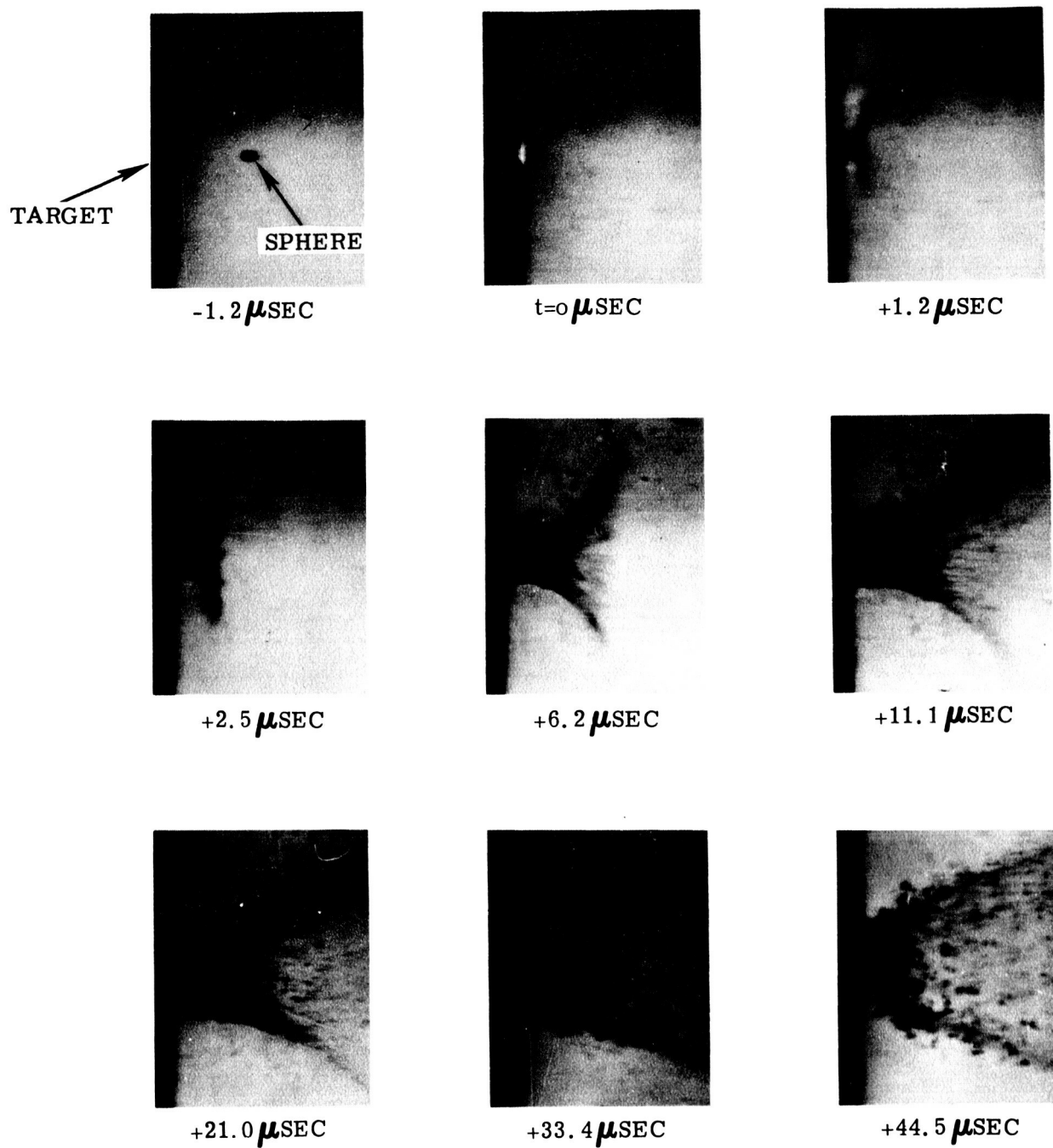
Figure 2 Framing-Camera Sequence of a 1/8-in. Glass Sphere
Impacting a Cast Aluminum Block at 7. 0 km/sec

Shock waves propagate a short distance from the contact surface in both the projectile and the target, and then rarefactions released at the boundary of the projectile start a lateral flow of both materials. During the first regime, an impact flash lasts for only a brief period (approximately 1 microsecond, as seen in the B & W camera frames of Figure 2). During the initial stages of the process, some fusion and ionization of both the projectile material and target material may occur. Although neither phenomenon has been observed to have a detectable effect on the correlations obtained, several significant observations should be noted.

The appearance of radiant emission in the form of an intense flash of light upon impact of the projectile is a result of the conversion of thermal energy of the shock-heated material into electromagnetic energy.[16] Most certainly the energy of the projectile is expended in a number of possible reactions, among which are the generation of heat, the initiation of radiation (possibly over a large spectrum from the gamma rays to microwaves but primarily between 2000A and 10,000A.) and the mechanical work done in forming the impact crater. Since the target reacts to the impact in a manner dictated by the magnitude of the pressure pulse, it may be reasonable to relate the intensity of impact flash to the properties of the shocked materials after collision. A process by which luminosity is derived from the rapid application of pressure is not yet available, although a theoretical study is presently being conducted by GM DRL. Consequently, a causal relationship between an impact-generated pressure and luminous radiation cannot be established by these experiments. (Of a more complex nature and much more difficult to define is the excitation energy of atoms under compression and the multiple electron problem in which electrons of different binding energies react in many different ways.)

Recent experiments conducted by both GM DRL and the Utah Research and Development Company have shown that the impact flash does indeed diminish in intensity as the ambient pressure of the surrounding gas is reduced. However,

TR64-48

at pressures less than approximately 200 mm of mercury and down to less than 10^{-4} mm of mercury the intensity of the flash remains essentially constant and the intensity of the radiation is a function of the impact velocity. Analysis of these results suggests a mechanism in which the atoms of a material are raised to their excited states. Recent considerations of the impact flash have extended beyond the empirical relationship for predicting impact flash, given in Reference 16, and have theoretically considered the possibility of establishing thermal equilibrium on an atom-to-atom level. From impact conditions in which pressures are raised as high as several megabars, attempts are being made to calculate the number of atoms ionized, the energy levels which can be established, and the percentage of the original projectile energy which has been dissipated in the form of impact-induced radiation.

Reviewing the model which covers the first regime of penetration described above, it appears probable that the microscopic properties of the impacting projectile and the impacted target are important during the first stage of crater formation.

Second Regime of Impact Cratering

During the second, steady-state stage, the densities and compressibilities of the projectile and target material as well as the velocity and the dimensions of the projectile all enter into any evaluation of the intensity and the duration of the pressure pulse produced. This second stage, commonly called the primary penetration stage, is that period during which the projectile acts as a causative force while its kinetic energy is dissipated in a fluid-flow process. The lateral dimensions relative to length of the projectile will determine the length of time required to achieve an equilibrium condition that is typical of the second stage. If the projectile length is very small compared to the smallest lateral dimension, the steady regime will be unimportant; the energy will be dissipated during the

transient regime and a broad, shallow crater will be obtained instead of the classical hemisphere. During this transient stage, shock waves are propagated from the contact surface into both the projectile and the target. At the same time, the pressure is released at the boundary of the projectile, initiating lateral flow of both materials. With projectiles whose length is significantly greater than their lateral dimensions, the process of the steady-state stage is far more important; and the crater formation resembles that of shaped-charge jet penetration. These phenomena have been experimentally verified.[6]

During this second stage, the region of compressed material is confined to a thin shell with extremely high energy density adjacent to the crater surface. For example, a meteoroid 1 mm in length striking a body of equal density at a velocity of 40 km/sec would produce a steady-state regime lasting only 0.05 microseconds and would penetrate a distance of 1 mm into the body during that time.

Third Regime of Impact Cratering

After the impacting body has been completely deformed and has been removed as a causative force from the system, the shock wave continues to expand and with it the crater. This is the third, or cavitation, stage of crater formation. Although the rate of crater expansion and the intensity and velocity of the shock decrease, the crater surface undergoes a more rapid decrease in velocity. Therefore, the thickness of the shell of compressed target material increases. These phenomena are shown to be experimentally verified later in this report.

During the second and third stages of crater formation, shear deformation takes place parallel to the walls of the expanding crater. The flow velocity is so high that the projectile material and the target material are both ejected from the crater with considerable velocity. It is only at relatively low speeds that the pellet material is found plated or scattered as small particles over the surface of the final crater. The amount of shear that occurs at extremely high strain rates is responsible for the classification of target materials into two groups — ductile and frangible.

TR64-48

The ductile materials flow for a much longer time after impact, apparently because of the decrease in their resistance to deformation at extremely high strain rates.[17] This behavior is not clearly understood, but it is similar to that used in some new impact-extrusion processes. The frangible materials include the long chain polymers, siliceous materials, and stones; in addition to their brittleness, they share a common monotonic increase in resistance to deformation with increasing strain rate, even at the very high strain rates involved in hypervelocity impact. As a result, the crater stops expanding in lucite earlier than in aluminum despite the relative magnitudes of their static shear strength.

These peculiarities of ductile and brittle materials have been one of the main sources of difficulty in formulating a complete theory. Hydrodynamic calculations, which yield accurate predictions for the initial stages of the process, must be normalized to predict final crater dimensions since they take no account of the stage in which high-strain-rate properties affect material flow. Since it is during this stage that a significant fraction of crater expansion takes place, calculation and experiment disagree in regard to depth of penetration and crater volume.

In developing the theoretical aspects of the third, or cavitation stage, the profiles of the pressure wave developed during the first two stages are of importance. In practice, as long as the pressures are high enough, the hydrodynamic approximation is accurate. (The resistance of the target material is significant only during the waning stages of the pressure pulse.) The cavitation stage of the process becomes so dominant in very-high-speed impacts on ductile materials that neither the density, compressibility, nor even the dimensions of the projectile can be detected in empirical correlations. At low impact velocities (say 4.0 km/sec), however, both the density and the shape of the projectile influence the crater volume and the shape of the crater.

In summary, the third or cavitation stage continues until the energy density behind the shock wave becomes too small to overcome the intrinsic resistance

to deformation of the material; at this point the shock wave continues to expand as a low-intensity plastic and/or elastic wave (the crater in ductile material may shrink somewhat from plastic and elastic recovery). In brittle materials, the tensile stresses produced by reflection of the shock wave from free surfaces will produce fracture and spall that may, in extreme cases, entirely obscure the form of the crater. These processes occur during the fourth, and final, stage of crater formation.

Fourth Regime of Impact Cratering

The fourth stage of crater formation is characterized by the reaction of the target material after the stress wave has been attenuated to a level that no longer causes flow or gross plastic deformation of the target material. Although this stage of crater formation is not considered in most theoretical approaches, experiments have been conducted to illustrate the three known reactions (1) elastic/plastic recovery of the crater, (2) possible brittle spalling around the surface of the crater, (3) recrystallization of the metal in an area beneath the visible crater.

In the case of the elastic/plastic recovery of the crater, Kineke[18] has shown that in the case of a target of 1100-F aluminum, the instantaneous crater depth and diameter reached a given maximum, then, in the final stages, the crater dimensions diminished; this would indicate that some recovery of the crater had occurred. The instantaneous crater dimensions were measured from sequential flash x-radiographs; in some instances, the final crater depth and/or diameter was as much as 20 percent less than the maximum reached during its formation. Other investigators[19, 20] have also reported observations on this phenomenon. Much work is described later in this report on the phenomena of crater recovery, particularly in estimating the amount of recovery for specific materials. Although a detailed analysis has not been carried out, it has been postulated that the compressed shell of material under the crater will undergo recovery R, to the degree allowed by

$$R = f \left[\frac{\sigma_y}{E} (\nu) \right] \tag{1}$$

TR64-48

where

σ_y = dynamic yield stress of the target material

E = dynamic Young's Modulus

ν = Poisson's ratio

In experiments to be described, framing-camera photographs and flash radiographs were taken of incipient craters at periodic intervals during crater formation. Careful measurement of the framing-camera photographs show that the final crater size in some materials may be less than the maximum size reached during the period of crater formation.

Many investigators have studied the third reaction observed during the fourth stage of impact cratering — the recrystallization of an "affected region" surrounding the actual crater. (This phenomenon may also occur during the third or cavitation stage of crater formation.) This "affected area" is significant for at least two reasons: First, energy that is not accounted for in the theoretical approaches is consumed in the material transformation process; second, for engineering or structural strength considerations, the affected region could have markedly different mechanical properties which would lead to total damage far in excess of that described by the immediately visible crater. Although it is not possible at this time to describe analytically the phenomena of shock-compression recrystallization, or to take into account the many variables of dynamic deformation and energy absorption, Glass and Pond[21] have calculated and made experimental measurements of the ratio of affected area to actual crater volume and have found that the ratio increased with increasing energy of the impacting projectile. Thus, it is indicated that at meteoroid impact velocities with significantly high impact energy, the volume of the affected area might be an order of magnitude larger than the actual volume of the crater.

THE RESEARCH PROGRAM

A considerable amount of basic work remains to be done in order to completely understand the role of strength of materials during the fast transient reactions discussed above, and to understand where this information can be profitably applied for the complex design of, for instance, a space ship. The purpose of the present investigation was to develop selected techniques, to measure some important parameters of hypervelocity impact, and to compare the results with existing theoretical treatments. These results will serve to determine the influence of strength of materials and, hopefully, provide a great amount of the needed basic information.

The remainder of this report has been organized into three separate sections, each containing a selected area of study in which experimental approaches, theoretical considerations, and results and discussions are presented. These three areas of investigation are:

a) Measurements of shock-wave pressures generated by impacts of aluminum projectiles into 1100-0 aluminum targets. The experimental results were obtained by measuring the free particle velocity upon the arrival of a shock wave at the rear face of each target so tested, using a "Throw-off Pellet Technique."

b) Measurement of axial momentum transmitted to aluminum semi-infinite targets upon impacts of aluminum projectiles. The measurements were obtained with a ballistic pendulum specially designed and constructed for the experiments. In addition, mass-loss measurements have been included fur comparision with "momentum multiplication" data.

c) Measurement of crater growth in various target materials. The observations were made using high-speed photography and flash x-radiography techniques. Also included are discussions on correlation of crater-lip and crater internal measurements, scaling in crater growth and correlation of cratering behavior with target properties.

TR64-48

Three appendixes are presented at the end of the report; the first two list the physical, mechanical and metallurgical properties of the projectiles targets together with cratering data; and a description of GM DRL's impact-range equipment is given in the last appendix.

SHOCK WAVE PRESSURE

Principle of Technique

Figure 3 shows the basic mechanism of the "Throw-Off Pellet" technique. A hemispherically fronted shock wave is created by the impact of an aluminum sphere into an aluminum target. After traversing a short distance through the target, the shock wave profile is essentially the one shown on the upper part of Figure 3a, its maximum value and its wavelength being, respectively, σ_M and λ . If one neglects the effects of rarefaction waves generated at the periphery of the pellet (which is essentially correct for thin pellets having a diameter-to-thickness ratio greater than 15,) the following phenomena takes place.

As illustrated in Fibure 3b, the shock wave enters the pellet through the target-pellet interface without attenuation. From simple geometrical considerations it can be shown that the portion of the shock wave which enters the pellet may be considered to be essentially a plane if the diameter, D, of the pellet is much smaller than the distance, R, of the shock front from the point of impact. After reaching the free face of the pellet, the compression wave (+) reflects as a tension wave (-) which moves now toward the left. Therefore, at the instant that the front of the tension wave reaches the target-pellet interface, the net stress at this point is in tension. Since in principle the target-pellet interface has no strength in tension, the pellet will fly off with a velocity which is determined by the implulse transmitted to the pellet during this period of interaction.

Using Newton's second law, the amount of momentum toward the right imparted to the pellet is given by
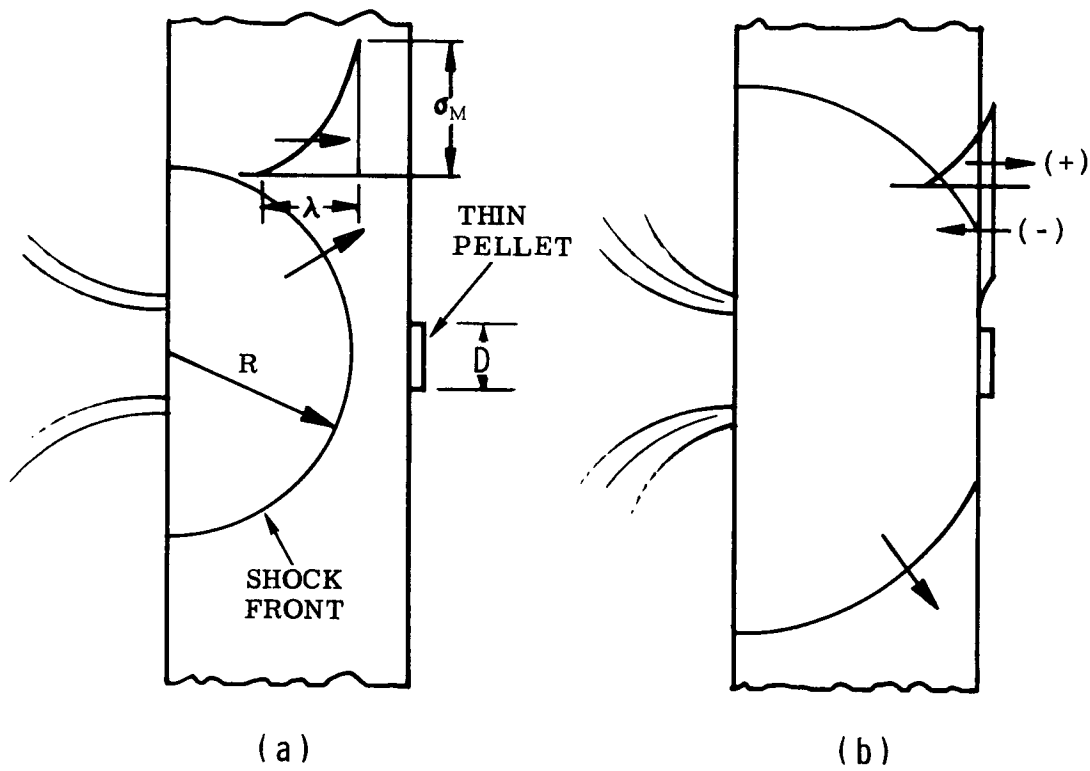
$$\int_0^t \sigma A \, dt = M_p V_p \qquad (2)$$

Figure 3 Fundamental Mechanism of the
"Throw-Off-Pellet" Technique

TR64-48

where σ is the stress level at any point on the shock-wave profile less than its maximum value; A is the cross-section area of the pellet; t is the total traverse time across the pellet of the compression and tension wave; and M_p and V_p are, respectively, the mass and the flying velocity of the pellet. Using the approximation that both compression and tension waves travel through the pellet at the same velocity U, the total traversal time t is given, therefore, by the relation

$$t = \frac{2T}{U} \qquad (3)$$

where T is the thickness of the pellet.

If the pellet is sufficiently thin, the left-hand side of Equation (2) can be re-written to give

$$\sigma_{av} At = M_p V_p \qquad (4)$$

where σ_{av} is the average stress acting on the left face of the pellet during time t . Inserting the value of t given by Equation (3) into Equation (4), one obtains Equation (5)

$$\sigma_{av} A \frac{2T}{U} = M_p V_p \; . \qquad (5)$$

Since the mass of the pellet is equal to ρAT and the stress can be expressed by the well-known relationship $\sigma = \rho Uu$, where u is the particle velocity behind the shock front in the target or in the pellet, one obtains

$$\rho Uu_{av} \frac{A2T}{U} = \rho ATV_p \qquad (6)$$

or

$$2 u_{av} = V_p \; . \qquad (7)$$

Equation (7) expresses the fact that the flying velocity of the thin pellet is twice the average particle velocity of the shock-wave portion captured by the

16

pellet during the time of interaction. In other words, if the pellet is sufficiently thin it will move at about the same maximum velocity as the free rear surface of the target upon arrival of the shock.

Experimental Approach

Figure 4 illustrates how the "Throw-Off-Pellet" technique was used at GM DRL for measuring shock-wave pressures generated by hypervelocity impacts of aluminum spheres into aluminum targets. 1100-0 aluminum projectiles (0.476-cm spheres) were accelerated to about 7.32 km/sec using the impact-range facilities described in Appendix C. The velocities of the pellets were recorded with a Beckman & Whitley framing camera, also described in Appendix C. As seen in Figure 4 the technique consisted of impacting a target at a given point and observing the motion of a thin pellet which had been previously affixed on the rear surface of the target immediately behind the point of impact. Upon arrival of the shock wave at the rear face of the target, the pellet flies off; its velocity is measured using high-speed-photographic techniques. All tests were conducted at a range pressure of about 30 mm of Hg.

The "Throw-off Pellet" technique was used for measuring pressures below 100 kbars. For higher pressures, the technique used was to observe the maximum velocity in the center of the bubble of debris behind the targets. This modified technique, which is essentially the same as the "Throw-off Pellet" technique, was used for thicknesses of targets thinner than 1.1 cm.

In order to avoid mismatch problems at the target-pellet interface, the thin pellets were also made of 1100-0 aluminum; their diameters and thicknesses were respectively 0.635 and 0.040 cm. The thicknesses of the targets were varied from 0.5 to 8.0 cm, but their side dimensions remained the same, 10 cm x 10 cm.
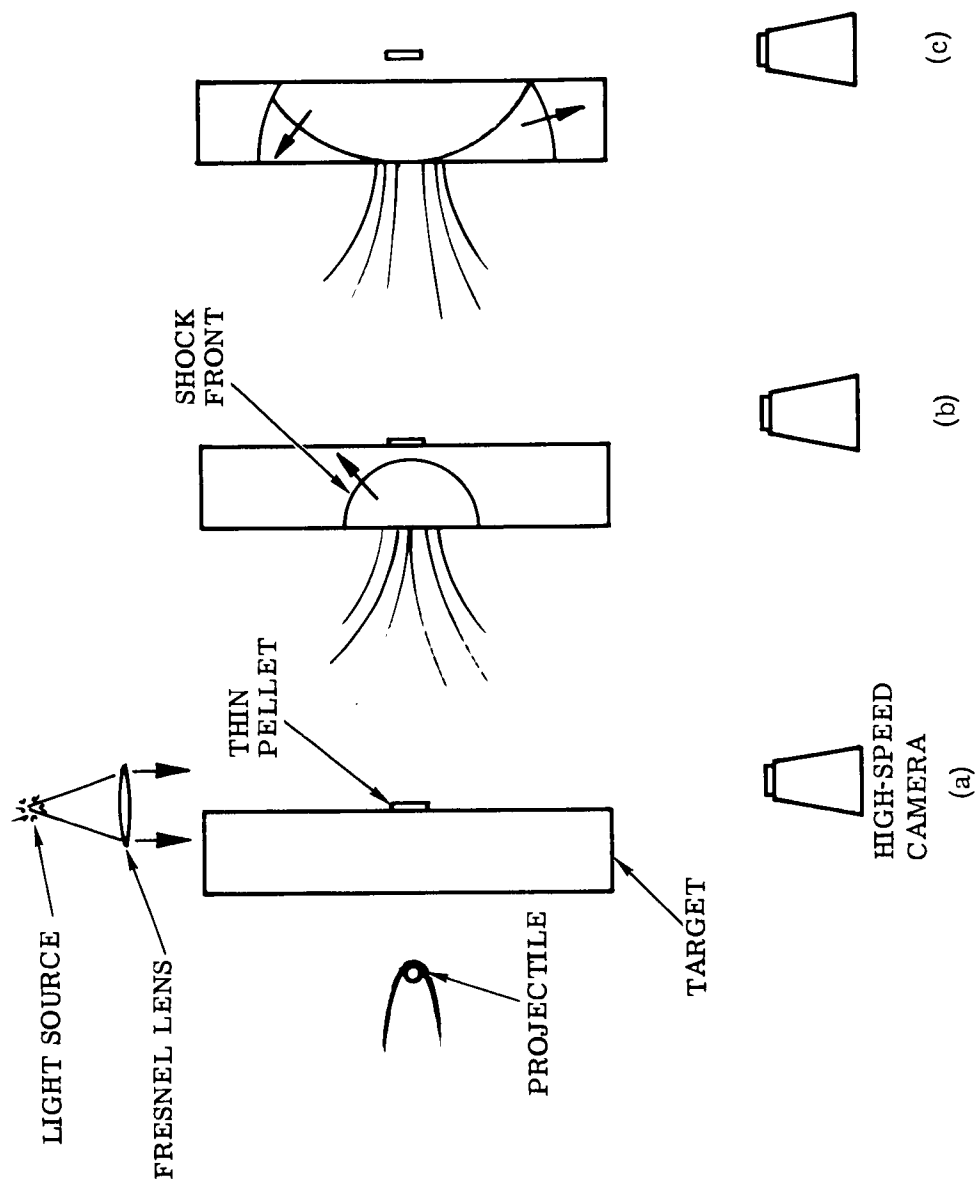
TR64-48

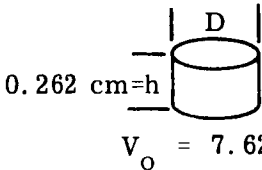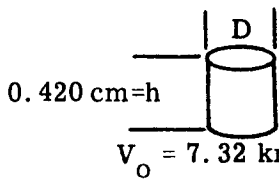Figure 4 Sequence of Events Illustrating the "Throw-Off-Pellet" Technique

Experimental Results

Table 1 shows the values of maximum shock-wave pressures predicted from hydrodynamic solution. Table 2 contains the experimental data collected during this series of tests to permit measurements of pressures. The calculated values were obtained from two different sources.[15, 22] Riney's and Heyda's[15] values were obtained considering the impact of a flat cylindrical projectile having a diameter-to-height ratio equal to 2 at an impact velocity of 7.62 km/sec. Tillotson's[22] values were obtained considering an impact of a projectile diameter-to-length ratio = 1 at an impact velocity of 7.32 km/sec. In both cases the volumes of the projectiles were equal to the volumes of the spheres used for the experiment. In order to determine from experiments the maximum shock-wave pressures generated by impacts of the projectiles, a plot was obtained from available literature[15, 22] showing pressures versus particle velocities behind shocks in aluminum. This plot is shown in Figure 5. Using the free-surface particle velocities as measured by the experiments and converting to particle velocities behind the shock in the material, it was possible to obtain Figure 6 from Figure 5. Figure 6, which shows the maximum shock-wave pressures versus distances from point of impact, is based on the assumption that the free-surface particle velocity is twice the particle velocity behind the shock in the material. The maximum error induced in the calculations using this assumption was estimated to be 3% at 500 kilobars.[23] The predicted values of pressures given in Table 1 are also presented in Figure 6 for purpose of comparison.

During this series of tests, the thickness of a target was adjusted so that incipient spall could be observed near its rear face. The thickness was calculated from previous experiments involving measurements of incipient spall threshold of 1100-0 aluminum at stress level zero (these experiments are reported in Appendix A); this value was found to be about 10.7 kbar. As shown in Figure 6, it was found that a 5.0-cm target should show an incipient spall close to its rear face if impacted at about 7.32 km/sec by a 0.476-cm aluminum sphere. A special target was made, therefore, for such observations, and its

TR64-48

Table 1

CALCULATED MAXIMUM SHOCK-WAVE PRESSURES
GENERATED BY IMPACTS OF FLAT CYLINDRICAL PROJECTILES
INTO ALUMINUM TARGETS

Heyda's and Riney's Solution		Tillotson's Solution	
0.262 cm=h D/h=2 V_O = 7.62 km/sec		0.420 cm=h D/h=1 V_O = 7.32 km/sec	
Distance cm	Pressure kbars	Distance cm	Pressure kbars
0.31	1,147	0.32	1,000
0.35	1,110	0.38	700
0.37	736	0.45	500
0.41	600	0.53	380
0.49	473	0.67	250
0.62	443	0.78	200
0.75	202		
0.78	223		
0.85	224		
0.92	211		
1.11	107		

Table 2

EXPERIMENTAL DATA USED FOR
DETERMINING MAXIMUM SHOCK-WAVE PRESSURE
GENERATED BY IMPACT OF 0.476-cm ALUMINUM SPHERES
INTO ALUMINUM TARGETS AT 7.32 km/sec

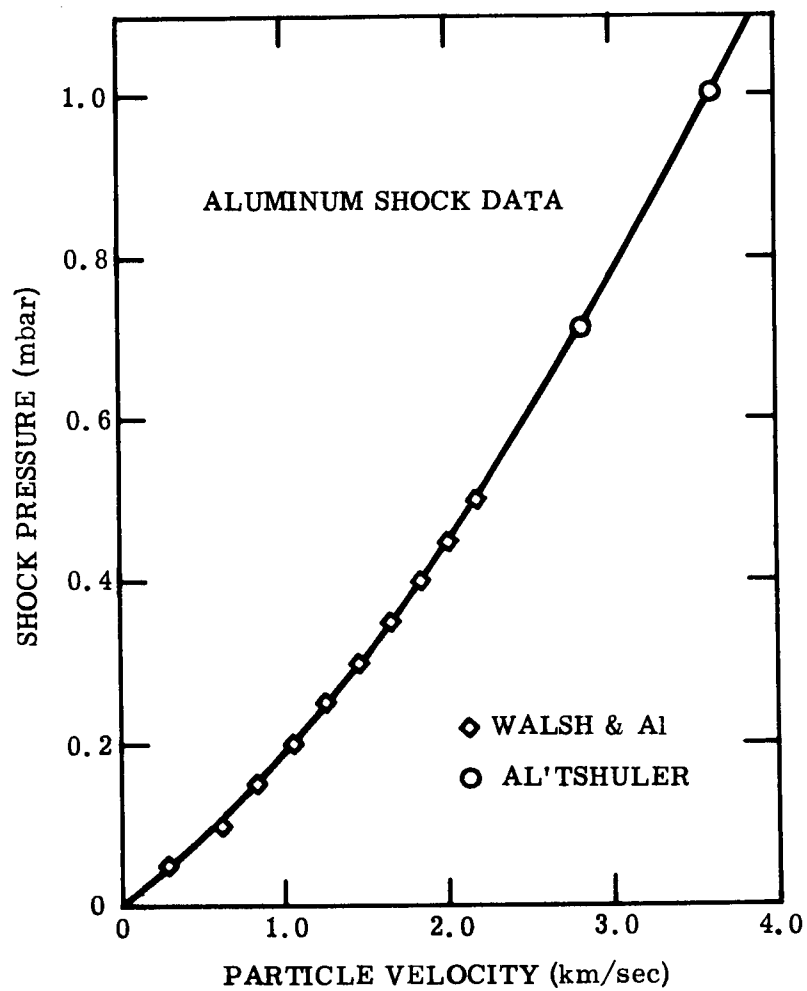| Target Thickness cm	Impact Velocity km/sec	Free Surface Particle Velocity km/sec	Measured Pressure kbars
0.51	7.41	3.300	352.0
0.76	7.11	2.170	206.0
1.02	7.26	1.622	150.0
1.02	7.33	1.431	130.0
1.53	7.26	0.894	78.6
1.91	7.39	0.590	49.6
2.54	7.20	0.372	31.5
3.05	7.36	0.283	23.9
3.55	7.41	0.245	19.8
4.80	7.62	0.160	12.0
6.40	7.62	0.093	7.6
7.61	7.03	0.040	5.3

TR64-48

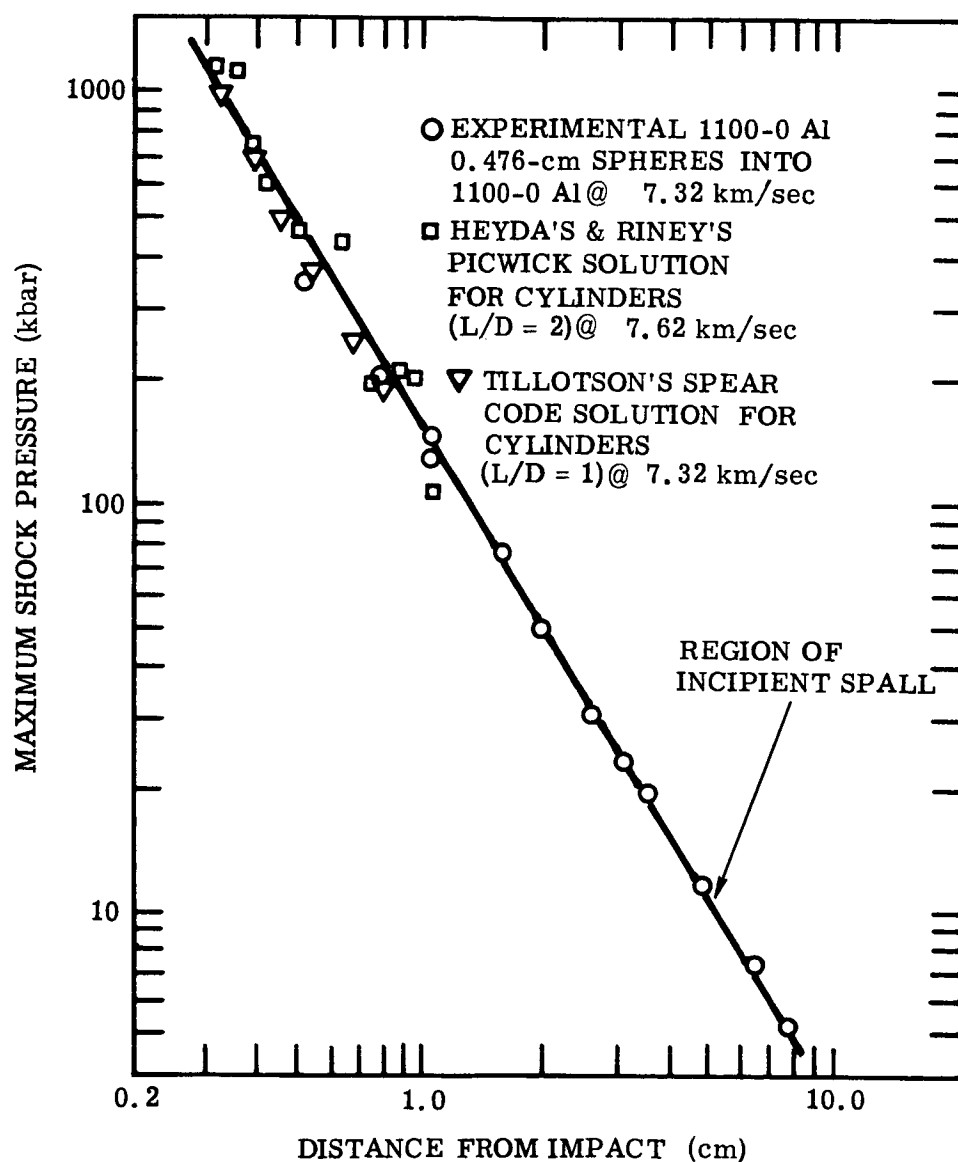Figure 5 Shock-Wave Pressure vs Particle Velocity in Aluminum

Figure 6 Calculated and Measured Maximum Shock-Wave Pressures
Generated by Impacts of Equivolume Projectiles into 1100-0
Aluminum Targets

TR64-48

configuration is shown at real scale in Figure 7. As predicted, an incipient spall was found about 4 mm from the rear face of the target. As shown in Figure 7 this special target served also to measure simultaneously the shock-wave pressure at two distances from the point of impact. From the spall thickness, it has also been possible to estimate the wavelength of the shock wave at about 5.0 cm away from the point of impact. Since in the case of incipient spall the maximum amplitude of the shock wave has the same values as the critical stress of the material, the wavelength is therefore twice the spall thickness, or 8 mm for this particular case.
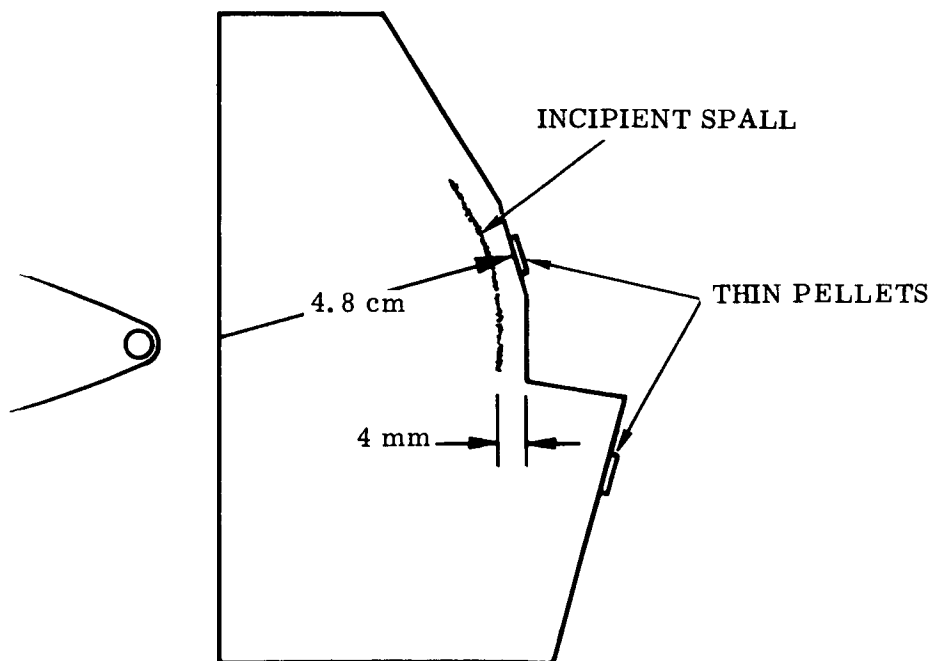

Figure 7 Special Target Used for Observing Incipient Spall

Discussion

The good agreement between the predicted and the measured shock-wave pressures shown in Figure 6 is very encouraging. First, it strongly indicates that the theoretical model assumed for the calculations was suitable for the present case. Thus, it is possible to calculate shock-wave pressures at various positions behind the impact point, thereby, permitting estimation of target damages. Also, the "Throw-Off Pellet" technique, has been demonstrated to be a promising technique for measuring shock-wave pressures in other materials and composite structures. Since there exists a unique relation between shock-pressure, particle velocity, shock velocity, and density of a material, it is possible to determine any of them once particle velocity is known. It is, therefore, also possible to accurately evaluate the arrival time of a shock wave after impact.

From Figure 4 it is possible to obtain an engineering relationship giving maximum shock-wave pressure in 1100-0 aluminum as a function of distance into the target and of the radius of the projectile. If a straight line is fitted through the calculated and experimental results, the following expression can be obtained:

$$\sigma_M = 1.234 \; \sigma_H \Big/ (R/R_0)^{1.6} \; , \quad R > 1.14 \; R_0 \tag{8}$$

where σ_H is the Hugoniot pressure corresponding to the impact velocity and R_0 is the (equivalent) effective radius of the projectile.

However, the 1.6-distance power-dependence of Equation (8) applies more specifically for pressures below 0.3 megabar. The calculated values indicate that a better fit would be obtained with a 1.8-distance power-dependence for pressure between 0.3 and 1.0 megabar. Calculations show that the distance power-dependence is changing continuously over the range of pressure reported in this work and would decay to unity in the elastic limit.

TR64-48

Equation (8) has been derived only from the results presented in this report and could be slightly inaccurate in predicting pressure with materials and projectiles other than for 1100-0 aluminum. However, until more calculations and more experimental results become available, shock-wave pressure in 1100-0 aluminum can be approximated from Equation (8) for projectiles having comparable diameters to 0.476-cm spheres. This last statement is justified by the scaling law which is found to hold in theoretical calculations.

MOMENTUM TRANSFER

Theoretical Considerations

The total axial momentum imparted upon impact to a semi-infinite target is the absolute sum of the projectile momentum and the axially projected component of the ejecta momentum. In terms of these quantities a multiplication factor M_f is defined as

$$M_f = \frac{MV}{mv_o} = \frac{mv_o + \left| \Sigma m_c\, v_e\, \cos\theta \right|}{mv_o} \tag{9}$$

where M and V are the mass and the velocity of the target after impact, $m_c v_e \cos\theta$ is the axial-momentum component of each individual mass of ejecta, and m and v_o are the mass and the impact velocity of the projectile. From Equation (9) one immediately notes that the multiplication factor is two if the impact is perfectly elastic (and if no target loss in involved).

Few investigators have attempted to predict or formulate the momentum experienced by semi-infinite targets upon hypervelocity impact. The work of Walsh, et al,[24] and of Tillotson[25] lead to the same conclusion even though they used slightly different approaches. Their hydrodynamic calculations showed that two similar projectiles of different masses and different impact velocities lead to the same late-stage hydrodynamic flow if the quantities $mv_o^{3\alpha}$ are the same. The value of α is presently evaluated at approximately .58 ± .04 . From this late-stage equivalence, the multiplication factor defined by Equation (9) was found to be

$$M_f = K\, mv_o^{3\alpha-1} \quad . \tag{10}$$

Equation (10) is not a complete determination of the total impulse imparted to the target, since it was obtained from the hydrodynamic stage of interaction only. However, the change with velocity can be learned from this relation. (By referencing to at least one experiment the proportionality constant K can be determined, and the momentum multiplication becomes explicitly defined for a given material for all velocities.)

A semi-empirical approach to the problem was made by Staniukovich.[26] He treated a hypervelocity impact as an explosive detonated at the surface of a target. He further assumed that the target mass loss in ejecta is related to the kinetic energy of the impact and by a strength factor. The momentum of ejecta was therefore given by the following relation:

$$m_c v_c = B \frac{E_o}{\sqrt{\epsilon}} \tag{11}$$

wherein E_o is the kinetic energy of the impactor, ϵ a strength factor and B a proportionality coefficient. From Equations (9) and (11) it is therefore possible to obtain the following relation:

$$MV = mv_o + K \left(1/2 \, mv_o^2\right)_{ejecta} . \tag{12}$$

A similar expression was obtained by Tillotson.[25]

Experimental Approach

Figure 8 illustrates the experimental arrangement which was specially designed and constructed to measure the momentum felt by aluminum semi-infinite targets upon impacts of 0.476-cm aluminum spheres. This experimental arrangement consisted of three components: a ballistic pendulum; a strobe light source; and a Polaroid open-shutter camera. As shown in Figure 8, the ballistic pendulum, which is a version of that used by others, consisted of a thin-wall aluminum tube 38 mm long and 15 cm in diameter. A plug was mounted at each end to permit firm attachment of cubic-block targets to the pendulum. In order to provide stability to the swing of the pendulum, a six-wire suspension system was used: three sets of two wires attached to the sides of the pendulum and to
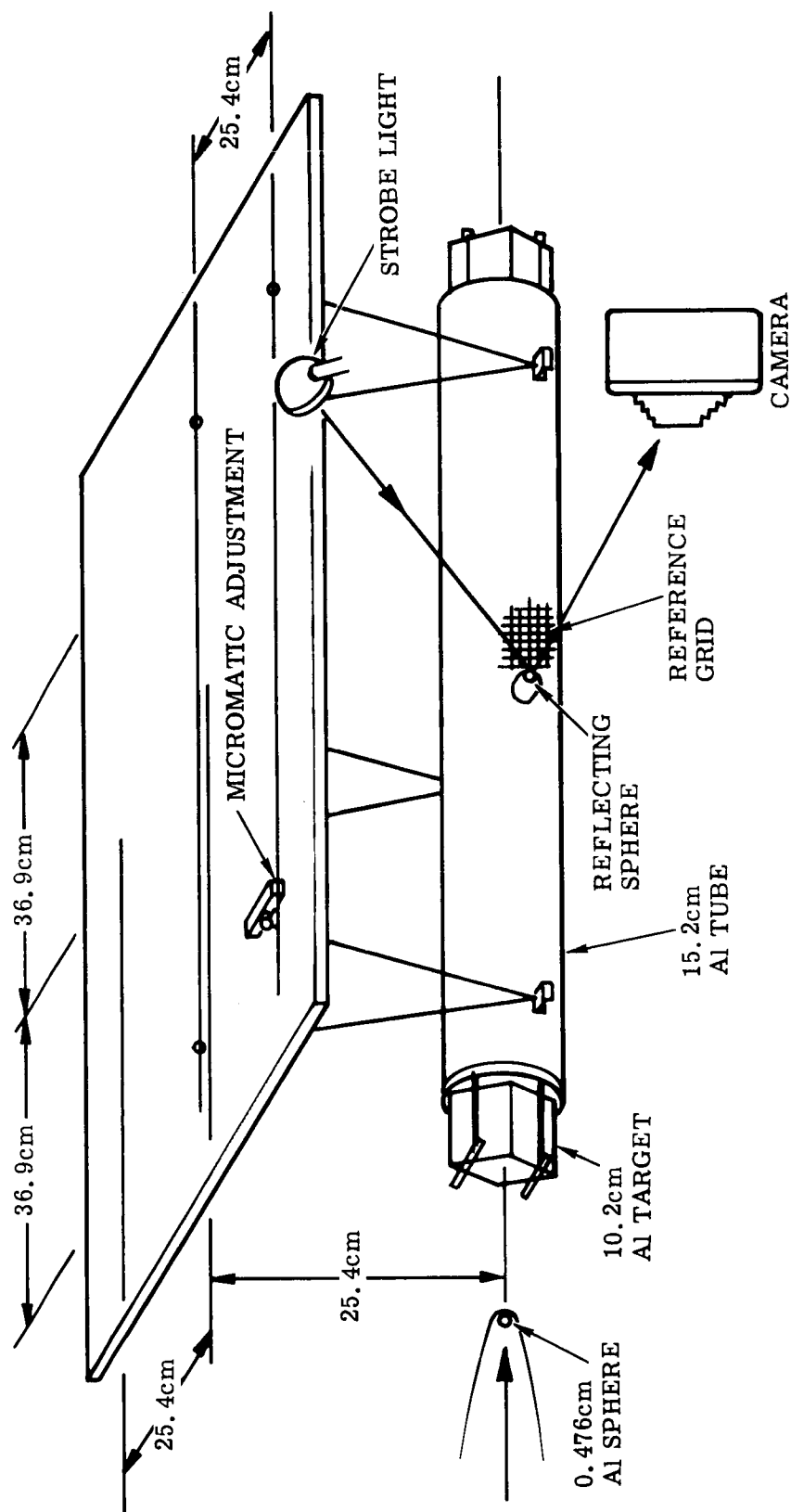
Figure 8 Ballistic Pendulum Arrangement

STROBE LIGHT

CAMERA

MICROMATIC ADJUSTMENT

25. 4cm

36. 9cm

36. 9cm

25. 4cm

25. 4cm

25. 4cm

REFERENCE GRID

REFLECTING SPHERE

15. 2cm Al TUBE

10. 2cm Al TARGET

0. 476cm Al SPHERE

the suspension plates by means of small holes and micromatic devices. This arrangement permitted controlling the effective lengths of suspension of the pendulum to within 0.1% of deviation. The same accuracy of construction was given to the rest of the system in order to give the planes, defined by each set of wires, parallellism between each other and orthogonality with respect to the line of flight of the projectiles. The ballistic pendulum was mounted inside a steel cage to permit easy manipulation between each experiment.

The swing of the pendulum was measured by flashing a series of light impulses at a tiny reflecting sphere fixed to the side of the pendulum. The light source, a General Radio Strobotac, Type 1531, was externally monitored by a special electronic circuit in order to obtain a sequence of 20 light pulses at the rate of 60 cps. This arrangement permitted observing approximately one third of the natural oscillation of the pendulum and, therefore, prevented rewriting on the photographic record.

An actual firing record consisted of a double exposure of the film. As indicated in Figure 8, a static exposure of a five-wire grid was obtained on the film while the pendulum was perfectly at rest. After removing the grid, the actual dynamic picture was obtained on the same film by triggering the flashing unit a few milliseconds before impact. A photographic record therefore consisted of a grid picture and a series of dots viewed by the camera in the same spatial plane. This arrangement permitted measurements within 3% of the absolute motion of the pendulum.

The main difficulty during this series of experiments was preventing any foreign matter (beside the projectile) from acting upon the ballistic pendulum immediately after impact. A fast-acting valve was therefore added to the impact-range facilities and successfully operated to obtain clean impacts. These tests were conducted with essentially the same range conditions reported in the preceding section.

TR64-48

Experimental Results

The experimental data collected during this series of experiments with the ballistic pendulum are presented in Table 3. Five sets of data are reported for 1100-0 aluminum targets, whereas one set is reported for 2024-T3 aluminum. As indicated in Table 3, some uncertainty is reported for the lowest velocity shot into 1100-0 aluminum. Figure 9 is a log-log plot of the momentum multiplication factor defined by Equation (9) and calculated from the data listed in Table 3. As seen by the straight line drawn through the experimental results for 1100-0 aluminum, the average slope is not the same as that predicted by Equation (10), which should be approximately unity. However, in his analysis of the results of other investigations, Tillotson[25] reported an empirical rule of thumb that could very well apply in this present case. The experimental results of momentum transfer by steel projectiles into lead targets show a break in the curve at impact velocities in the target corresponding to twice the speed of sound. For higher impact velocities, the experimental results agree with the theoretical prediction. Therefore, the dotted curve passed through the experimental results in Figure 9 could very well be of unity slope at impact velocities above 10 km/sec.

The result for a 2024-T3 aluminum target, which is also presented on Figure 9, is very significant. From this result one can see a much higher impulse transmitted to a 2024-T3 aluminum target than to an 1100-0 aluminum target at about 7.5 km/sec. As presented in Table 4, the mass loss of the 2024-T3 target was found to be approximately three times the mass loss of an 1100-0 target, although the impact conditions were the same and the crater volume of the 2024-T3 target was smaller. This result indicates that in this region of impact velocities the momentum multiplication is mostly due to the material ejected during the later phase of interaction when the strength of material controls the crater formation.

Figure 10 is a log-log plot of ejecta momentum versus impact velocity. For the range of velocity covered by the experiments, the experimental results agree very well with Equation (12) derived from Staniukovich's[26] assumptions.

30

Table 3

EXPERIMENTAL DATA OF BALLISTIC PENDULUM

Spherical Projectile (0.157 gm)	Impact Velocity (cm/sec)	Pendulum Mass (gm)	Max. Velocity of Pendulum After Impact (cm/sec)	Momentum of Pendulum (gm-cm/sec)	Momentum of Ejecta (gm-cm/sec)
0.476-cm 1100-0 Al	4.00×10^5	8,773 1100-0 Al-Tgt.	9.45	82,900[a]	20,100
0.476-cm 1100-0 Al	5.43×10^5	8,773 1100-0 Al	14.05	123,100	37,700
0.476-cm 1100-0 Al	5.95×10^5	8,773 1100-0 Al	15.2	136,100	42,600
0.476-cm 1100-0 Al	7.11×10^5	8,773 1100-0 Al	20.40	179,000	67,300
0.476-cm 1100-0 Al	7.43×10^5	9,060 2024-T3 Al Tgt.	24.38	221,000	104,200

(a) Uncertainty in momentum measurement due to extraneous matter which interacted slightly with the pendulum during impact.
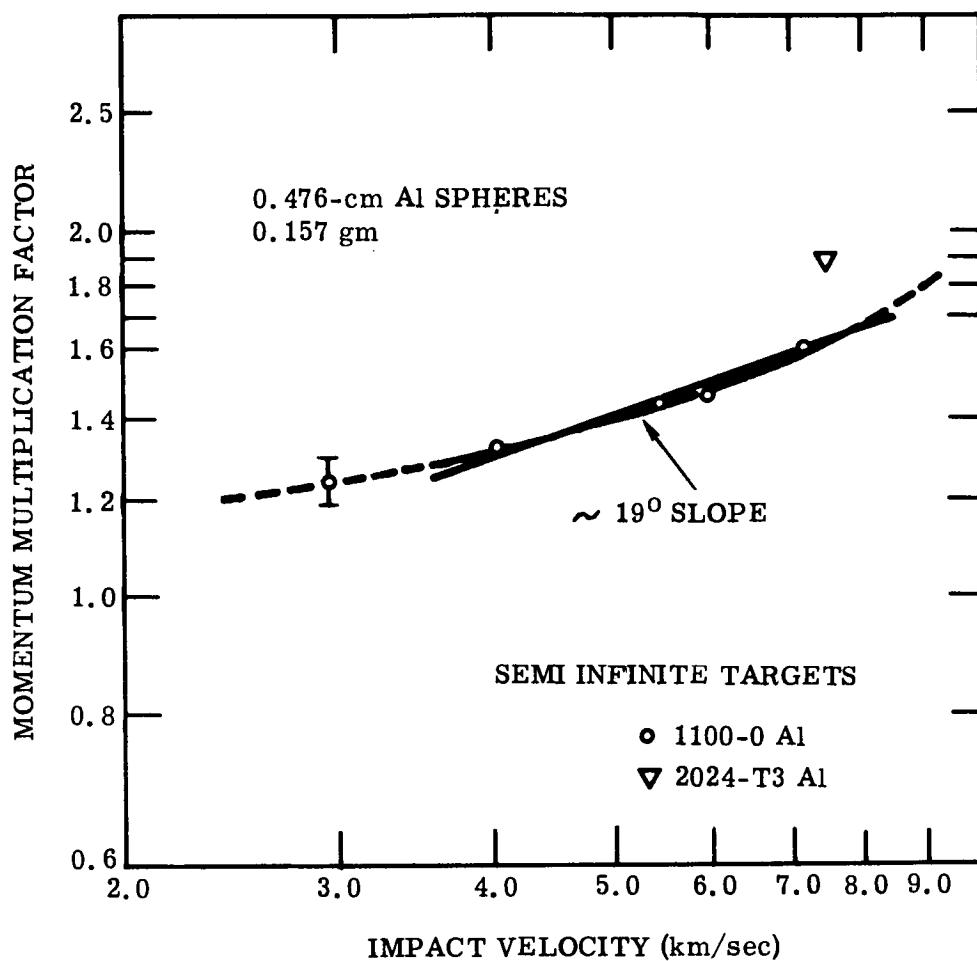
TR64-48

Figure 9   Momentum Multiplication Felt by Aluminum Semi-Infinite
Targets Being Impacted by 0.476-cm Aluminum Spheres

Table 4
TARGET MASS-LOSS DATA

Target Material and Shape	Projectile Spheres	Loss of Mass (grams)	
		GM DRL [a]	Vendor [b]
Cd - #B (A) 5. 1-cm cube [d]	1100-0 Al 0. 476-cm. D [c]	7. 59 ±. 05	7. 591 ±. 001
Cd - #B (C) 5. 1-cm cube	C1015 STL 0. 318-cm D [c]	6. 77 ±. 05	6. 742 ±. 001
Cd - #B (D) 5. 1-cm cube	C1015 STL 0. 318-cm D [c]	6. 92 ±. 05	6. 977 ±. 001
1100-0 Al 8. 9-cm hex x 10. 2-cm long	1100-0 Al 0. 476-cm D [e]	0. 99 ±. 05	– –
1100-0 Al 8. 9-cm hex x 7. 6-cm long	1100-0 Al 0. 318-cm D [e]	0. 57 ±. 05	– –
2024-T351 Al 8. 9-cm hex x 10. 2-cm long	1100-0 Al 0. 476-cm D	3. 0 ±. 1	– –

NOTES:

(a) Average of two successive readings on lab. balance

(b) Values certified by Watson Bros., Los Angeles, Calif.

(c) Projectile velocity approx. 6. 9 km/sec.

(d) Target struck by sabot fragment, causing additional weight loss

(e) Projectile velocity approx. 7. 4 km/sec.

TR64-48
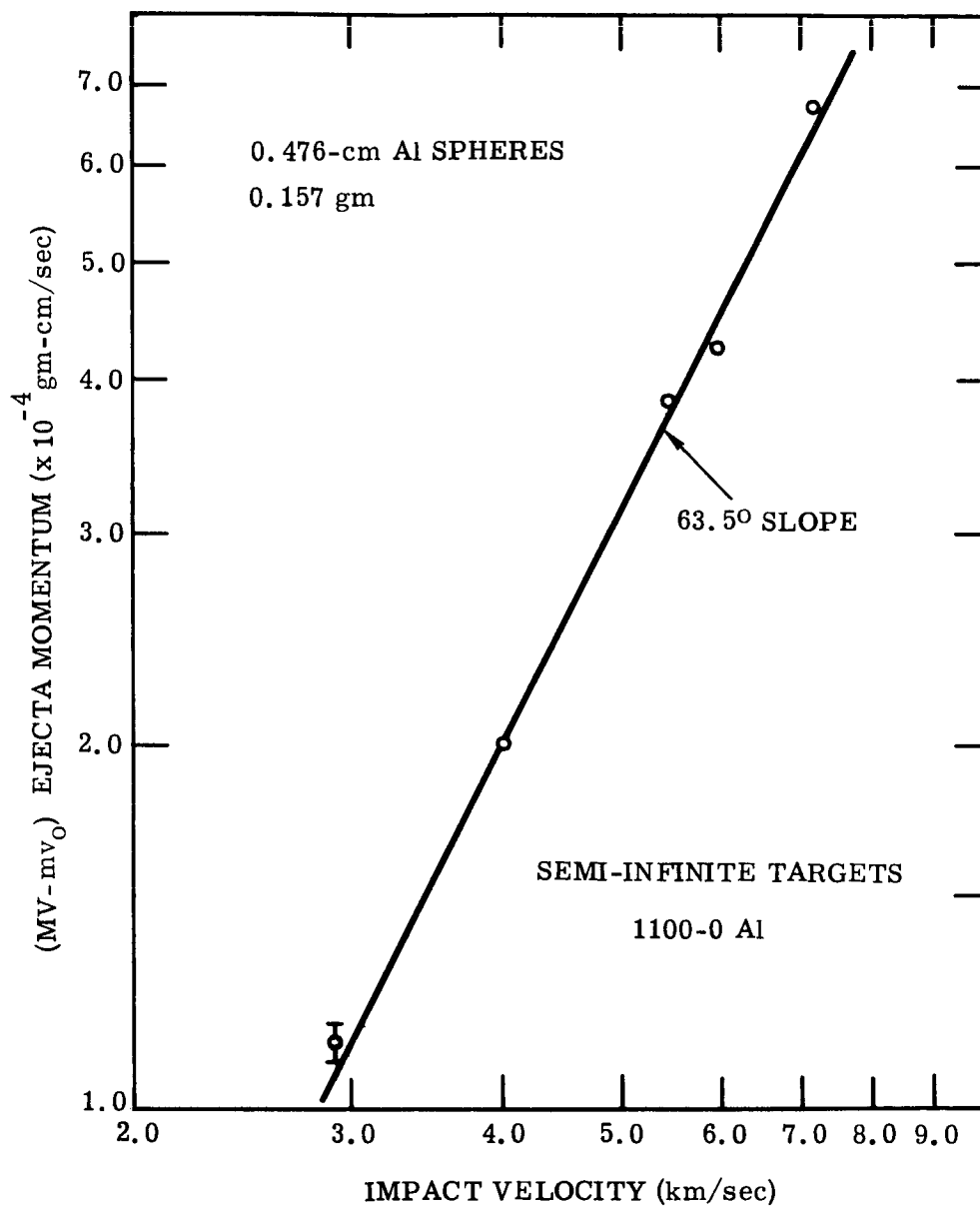

Figure 10 Momentum Increase Felt by 1100-0 Aluminum Semi-Infinite
Targets Being Impacted by 0.476-cm Aluminum Spheres

The 63. 5-degree slope indicates a variation of the ejecta momentum as the square of the impact velocity. If a plot is made of the value "multiplication factor minus one" versus impact velocity, a very good linear dependence with the velocity is found; this is indicated by Equation (12) rewritten in the following manner:

$$(M_f - 1) = K \frac{V}{2} \tag{13}$$

Discussion

A complete theoretical model of momentum transferred to semi-infinite targets by hypervelocity impacts has not yet been developed. Very few investigators have attempted to describe the flow of material which is controlled by strength effects. This is due to the high complexity of interaction, to the lack of knowledge of material behavior during this late stage of interaction to the difficulty of solving the flow equations with current computing facilities. On the other hand, the part of the problem which is treated by hydrodynamic solutions cannot always be verified experimentally because of the limitations imposed by experimental equipment. Many current programs now are being undertaken to examine the hydrodynamic regime more closely for comparison between theory and experiment.

On the basis of the observations made during this series of tests and for the range of impact velocity explored, it seems that the momentum multiplication is mostly controlled by the masses ejected during a later stage of interaction. Without having further experimental evidence, this statement seems to hold for impact velocities up to 8. 0 km/sec into aluminum targets.

CRATER GROWTH

Theoretical Considerations

The application of the hydrodynamic model in describing the initial regimes of crater growth has been confirmed experimentally by the results from the shock-pressure measurements described in the previous section. The influence of target-material properties (i. e. , mechanical and physical properties

TR64-48

characteristic of solid-state behavior) on crater formation has not been accepted generally as a significant consideration, although earlier studies have indicated that they should be important.[27, 28] It was desirable, therefore, to study further the crater-formation process and to clarify this controversial point.

In Figure 11 the anticipated effect of target strength on crater growth is depicted schematically for two aluminum-base targets differing widely in strength. During the initial stages of crater formation shown therein, the hydrodynamic model applies; no effect of solid-state properties is expected; and the growth curves for the two materials are shown to be coincident. At some later time the "hydrodynamic regimes" are replaced by the "solid-state regime," during which the growth curves are shown to diverge increasingly with time until crater formation ceases.

The objective, then, for this section of the program was the study of the crater-formation process, with particular attention to the anticipated solid-state regime, Figure 11.

Experimental Procedures

To accomplish this objective, crater-growth observations were made using very-high-speed photographic and radiographic equipment in connection with hypervelocity impact shots on GM DRL's free-flight range "D". This range and its associated instrumentation are described in Appendix C.

The experimental arrangement of the photographic and radiographic equipment for crater-growth observations is illustrated schematically in Figure 12. The photographic equipment consisted of a Beckman-Whitley Model 192 high-framing-rate camera and a Fresnel lens and light source of controlled pulse duration, triggered by a range impact-time computer a few microseconds before impact. With the above system continuous photographic records were obtained of impact, ejecta, and crater growth (following measurements on the silhouette of the minimum outside diameter, D_o, of the crater lips near the original target surface). The radiographic equipment consisted of a Field Emission Model 730

36

ALUMINUM (LOW STRENGTH)

ALUMINUM (HIGH STRENGTH)

CRATER
DIAMETER

TARGET STRENGTH EFFECTS
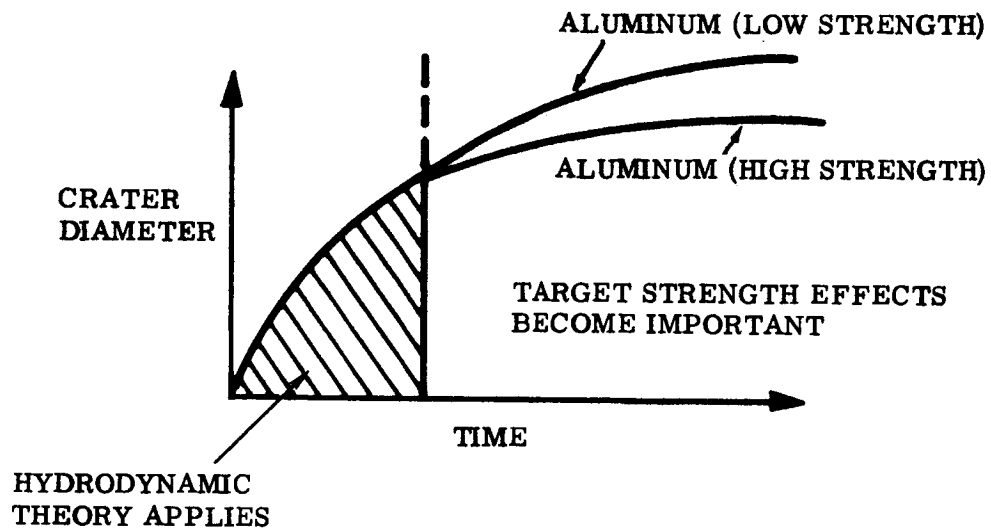BECOME IMPORTANT

TIME

HYDRODYNAMIC
THEORY APPLIES

Figure 11   Anticipated Effect of Target Strength on Target Damage
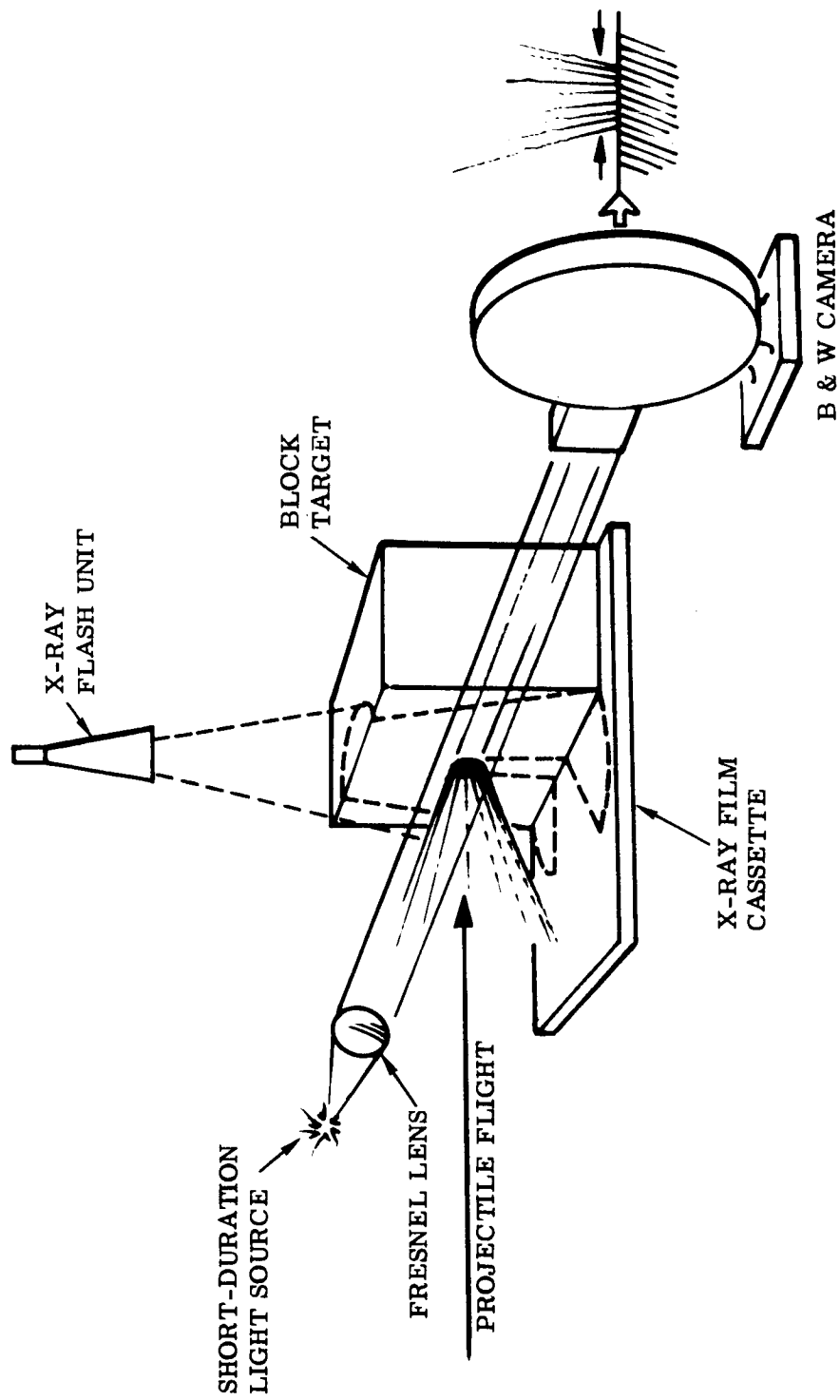Resulting from Hypervelocity Meteoroid Impact

37

TR64-48

Figure 12 Experimental Arrangement for Crater Growth Observation

unit which directs a very-high-intensity X-ray beam (duration 0.07 μsec) through the target. Measurements were made (at the original target surface) of the instantaneous values of the internal diameter, D_I, for preselected times after impact (±1 microsecond). Since the semi-infinite targets used in this program were 10.2-cm. cubes, it was possible for the X-ray beam to "see through" only the aluminum-base target materials. The values of X-ray mass absorption coefficients ($\frac{\mu}{\rho}$) with (W-Kα) radiation for the three other target materials were much larger than for the Al targets and too high to permit the recording of measurable results on the film within the casette.

The materials selected for study as hypervelocity-impact couples were: 1100-0 Al projectiles into 1100-0 Al, 2024-T3 Al, c.p. Cd, OFHC Cu, and 200 Ni targets.[*] The Cd, Cu and Ni target materials were selected for the purpose of studying the influence of such solid-state properties as melting temperature for materials having nearly the same value of specific gravity; i.e., there would be no variation in the specific gravity parameter, at least, to enhance chances of finding a correlation between cratering behavior and target solid-state properties. C1015 H/R steel projectiles were also shot into the Cd, Cu and Ni target materials. The chemical, physical, mechanical and metallurgical properties of interest for all of the projectile and target materials are presented in detail in Appendix A.

<u>Results and Discussion</u>

Target, projectile, and crater data (final dimensions) for all range tests are compiled in Table B-1, Appendix B.

    a. <u>Crater-Growth Curves</u>:

Plots of high-speed photographic observations during crater growth in Cd, Cu and Ni semi-infinite targets, impacted at projectile velocities of 4.3 and 7.0±0.3 km/sec are presented in Figures 13, 14 and 15. In Figures 16-a, -b plots for 1100-0 Al and 2024-T3 Al and for Cd semi-infinite targets are presented, along

---

[*] Material designations are defined in Table A-1, Appendix A.
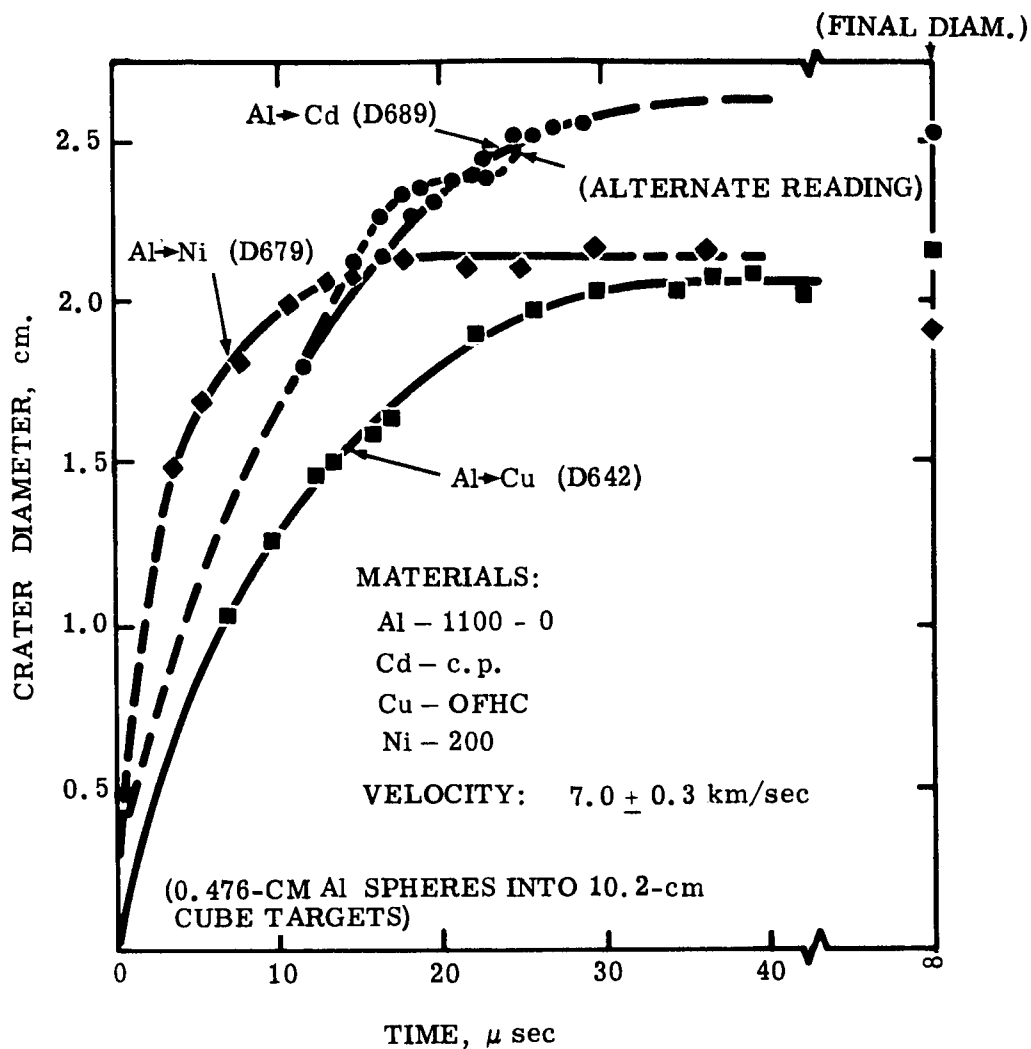
TR64-48

Figure 13 Impact-Crater Growth for Al Projectiles Against Cd,
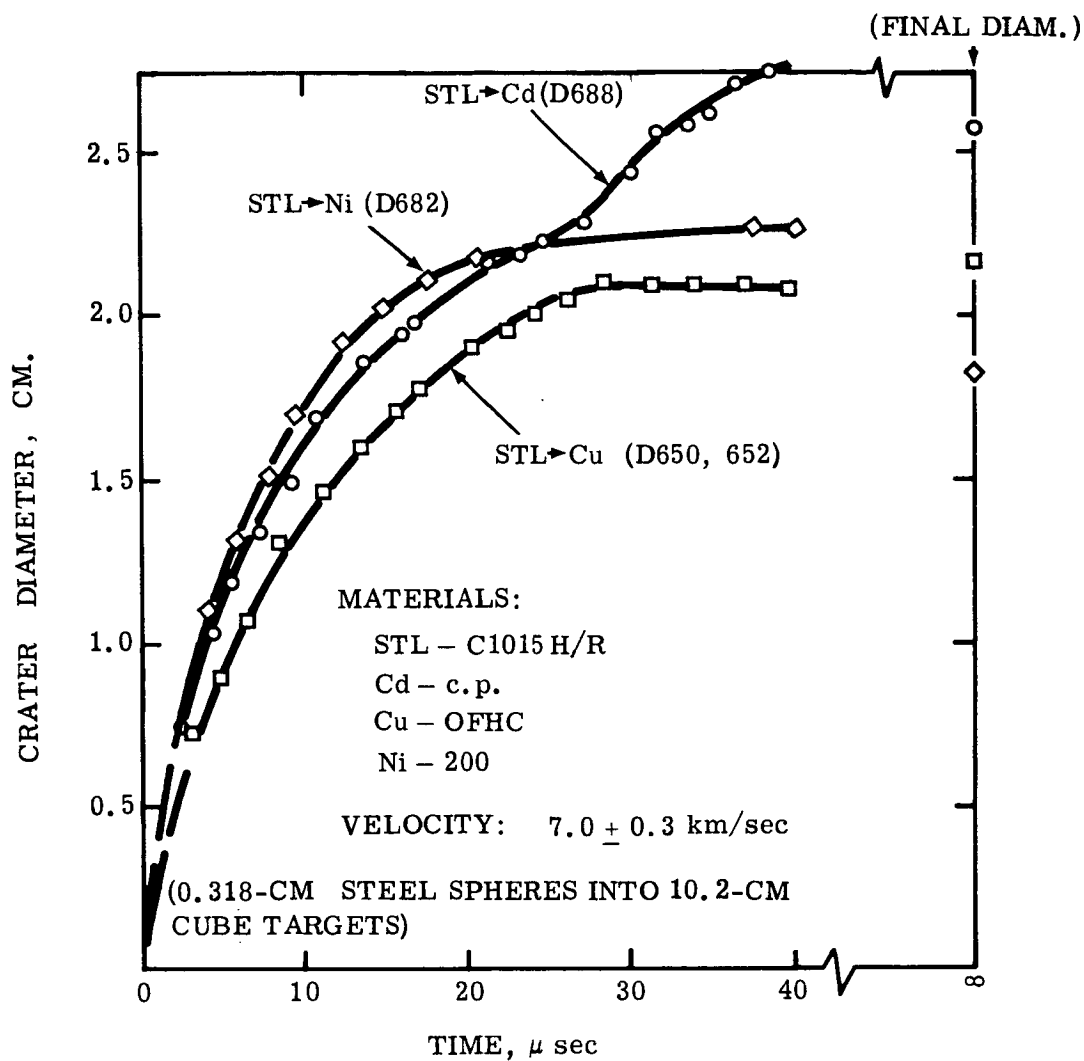Cu, and Ni Semi-Infinite Targets

TR64-48

Figure 14 Impact-Crater Growth for Steel Projectiles Against Cd,
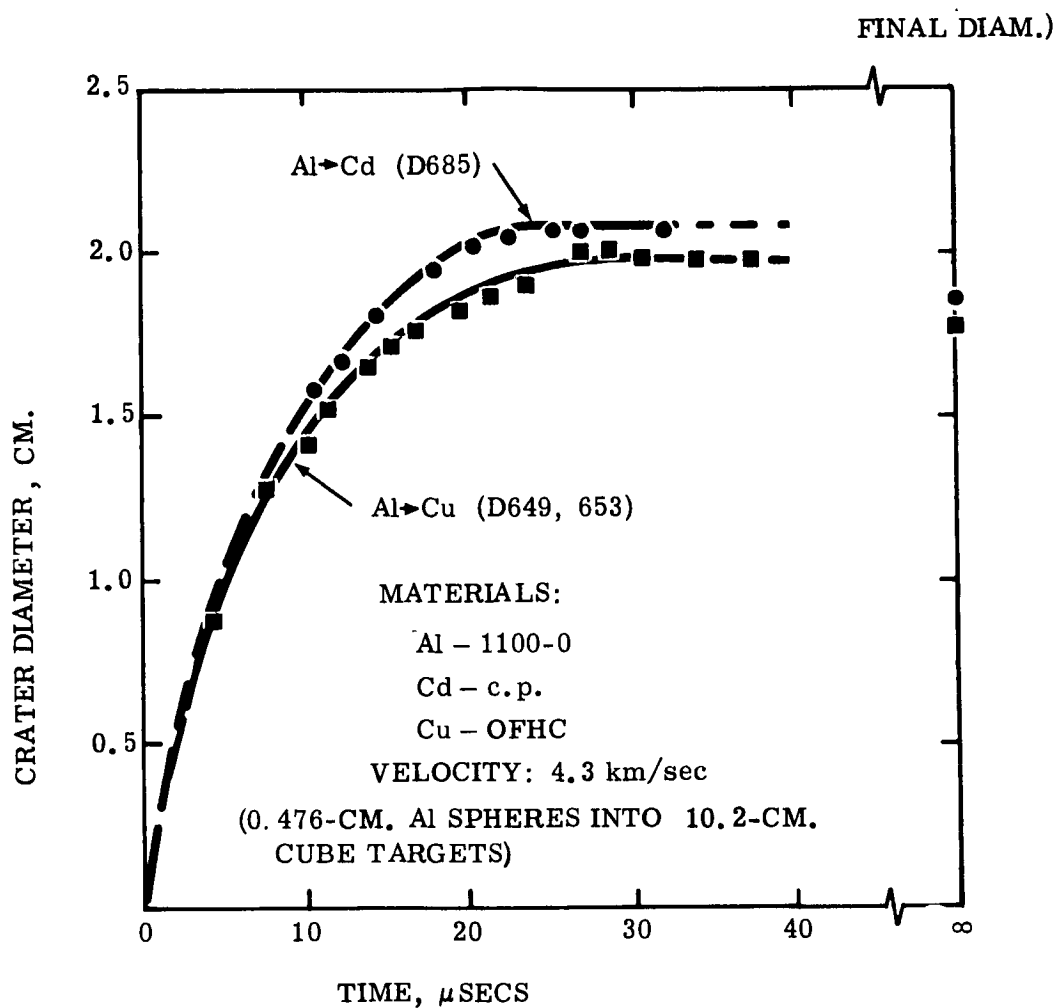Cu, and Ni Semi-Infinite Targets

TR64-48

Figure 15 Impact-Crater Growth for Al Projectiles Against
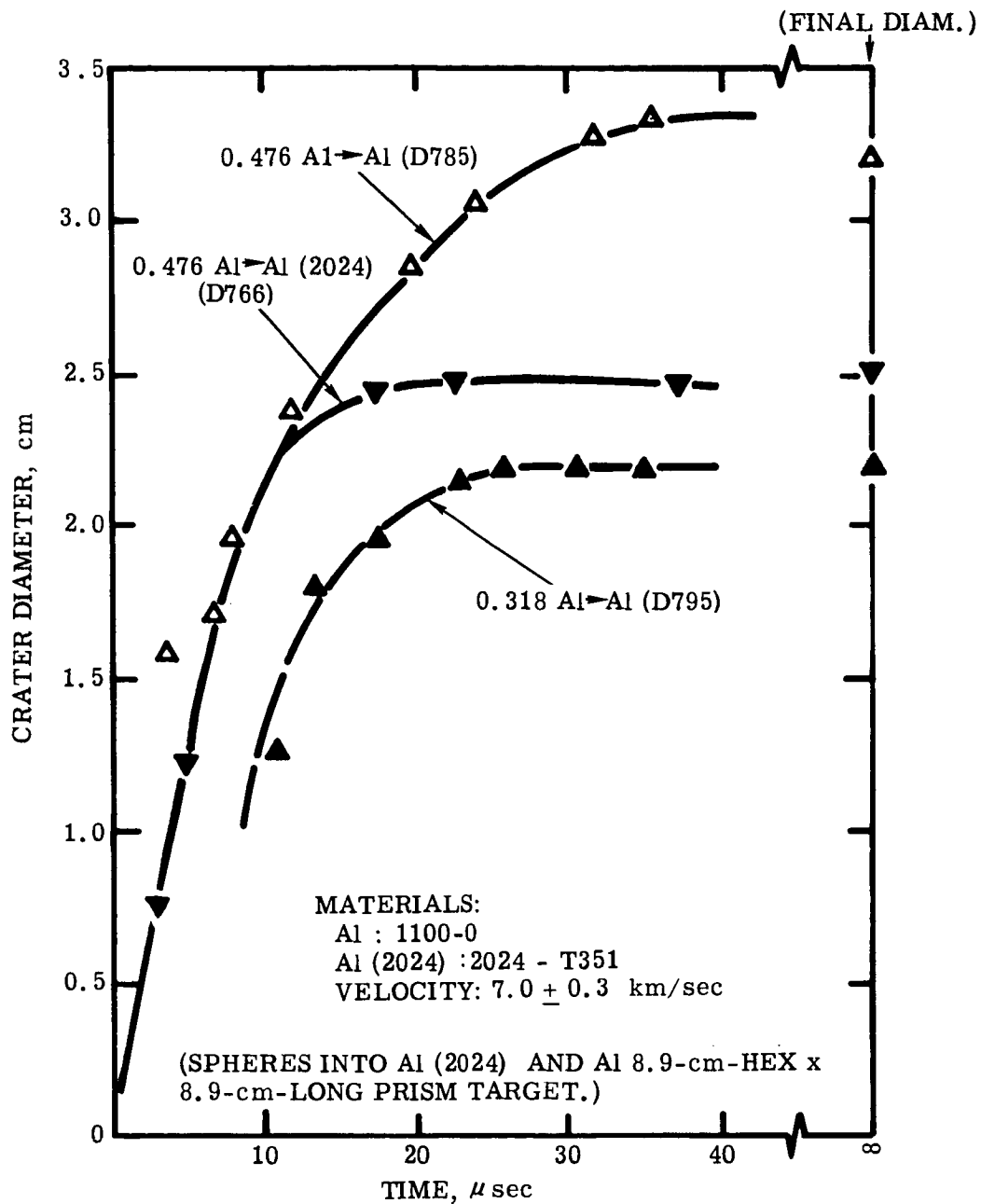Cd and Cu Semi-Infinite Targets

Figure 16a Impact-Crater Growth for Aluminum Projectiles
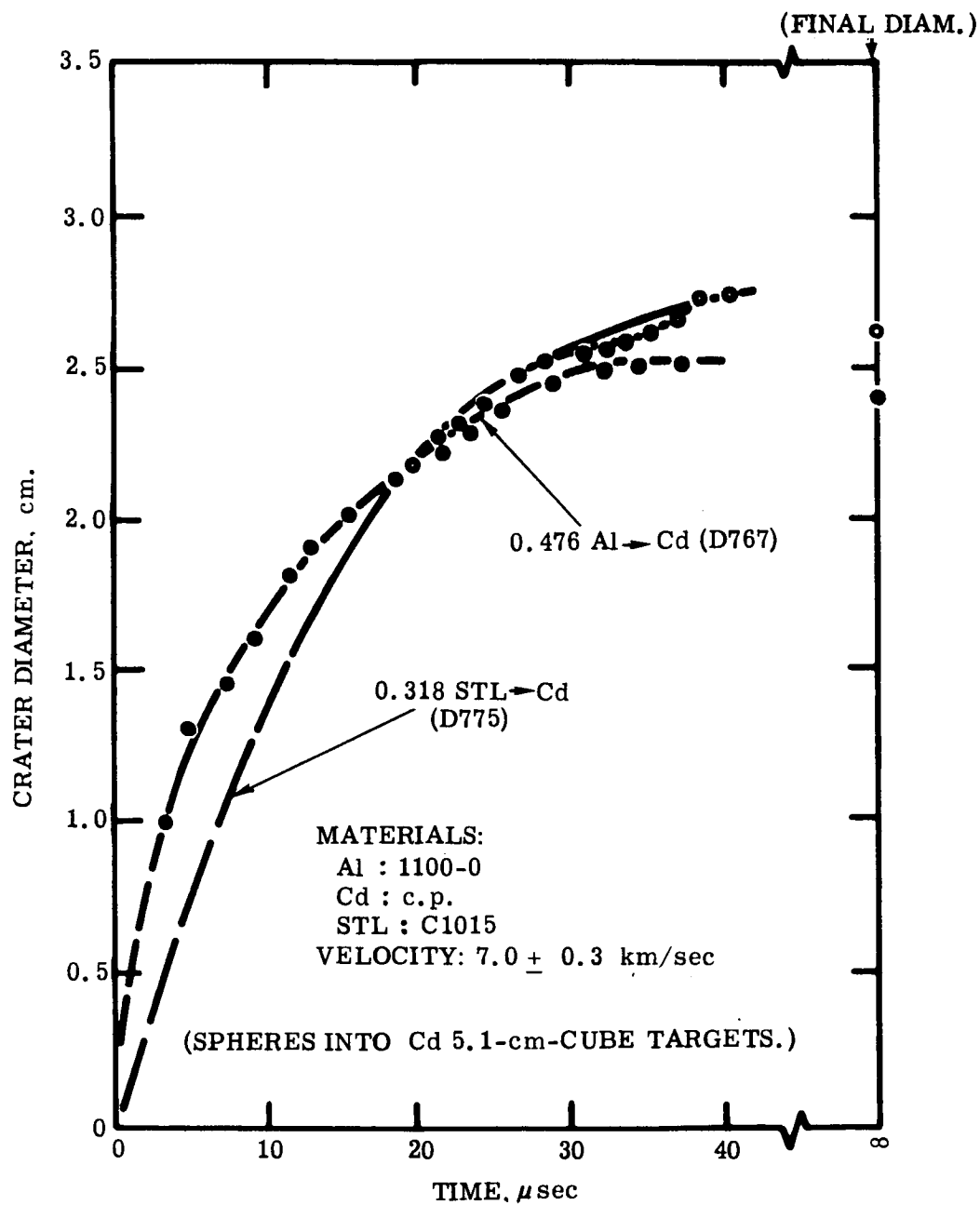Against Aluminum Semi-Infinite Targets

TR64-48

Figure 16b   Impact Crater Growth for Aluminum and Steel Projectiles
Against Cadmium Semi-Infinite Targets

with several other variations in target or projectile size or material for comparative purposes. In these figures D_o, the minimum diameter of the crater-lip silhouette near the original target surface, has been plotted as a function of time following impact. Also, in these figures the final crater diameter (minimum D_o, measured by precision micrometers) is indicated at the right-hand margin in each. A difference between the right-hand terminal of a plotted curve and the final measurement represents the dimensional recovery (elastic and anelastic) occurring during a very late stage of crater formation as impact-induced stress is released.

b. Analysis of Crater-Growth Process:

An inspection of Figures 13 − 15 reveals three distinctly separate regimes (II, III and IV as described in the Introduction) in the crater-growth process. An initial regime, regime II, is observed initially during which growth occurs at extremely high rates ($\sim$ 0. 2 cm per microsecond). A final regime, regime IV, is observed during which the growth rate is essentially nil and during which dimensional recovery (if any) occurs. An intermediate or transitional regime, regime III, is also observed during which formative mechanisms controlling growth during regime II are gradually supplanted by those controlling growth during regime IV.

c. Correlation of Crater Growth with Target Properties:

Additional examination of Figures 13, 14 and 15 reveals that during regime II, for impacts by both aluminum and steel projectiles at 4. 3 and at 7. 0 km/sec, the order of target materials for increasing growth rate and magnitude at some time during this regime is: Cu, Cd, Ni. For regime III the order of increasing crater magnitude at some time of interest is: Cu, Ni, Cd. For regime IV the order of increasing magnitude at a given time is: Ni, Cu, Cd. In connection with this last observation, the order of increasing dimensional recovery is: Cu, Ni, Cd, or Cu, Cd, Ni − the extent of recovery in Ni and Cd being nearly equal, within experimental uncertainty.

Attempts were made to correlate the orders of increasing crater magnitude presented above with several physical/mechanical properties of the target

TR64-48

materials. Properties of interest to this correlation are compiled in Table
A-3, Appendix A. All of the properties listed in Table A-3 (except specific
gravity) exhibited a decreasing order of values as follows: Ni, Cu, Cd. Thus,
a correlation is established between the solid-state target properties and
regime IV, but not with either regimes II or III.

Since the property values listed are for "equilibrium" or nearly static conditions,
it is not surprising to find that such a correlation exists only for regime IV
(during which "equilibrium" conditions are attained). The hydrodynamic model
for crater growth would be expected to apply during regime II; hence, solid-
state properties need not relate to material behavior observed during this
regime. The material behavior observed during regime III probably represents
a transition between behavior observed during the initial and final regimes and
also need not relate to physical/mechanical properties. It should be pointed out
here that the process of crater growth is without discontinuities, i. e., the
arresting of material flow in the vicinity of the impact is continuous. Consider
the radial momentum equation which determines material velocity, U_p, at each
point in the flow:

$$\rho \frac{\partial U_p}{\partial t} = \left(\frac{\partial P}{\partial r} + \frac{\partial \sigma}{\partial r} \right),$$

wherein σ is the stress-deviator tensor and P is the hydrodynamic pressure.
The velocity decreases as the terms on the right side of the equation decrease.
For hypervelocity impact $\sigma \ll P$ initially (regime II); hence, $\frac{\partial U_p}{\partial t}$ responds
mainly to the decreasing $\frac{\partial P}{\partial r}$ term. As P approaches zero in the late stage of
crater growth (regime IV), σ becomes increasingly more significant; and
eventually $\frac{\partial U_p}{\partial t}$ responds mainly to the decreasing $\frac{\partial \sigma}{\partial r}$ term. Although
this mathematical description of crater formation is, indeed, continuous, it
is more convenient to discuss it in terms of a phenomenological sequence of
"regimes," as has been done herein.

An additional point of interest is the observation that, as crater growth takes
place within the Cd, Cu and Ni target materials, Cu and Cd maintain the same
relative order throughout all three phases, while Ni shifts from highest during

regime II to intermediate during regime III and to lowest in crater magnitude
during regime IV. No explanation for this peculiar, but seemingly orderly,
behavior can be offered at this time.

d. Growth Arrest in Cd Targets:

A growth arrest or point of inflection is observed in Figure 14 for Cd (and
perhaps also in Figures 13 and 16b for Cd, although its presence therein is
open to question). However, such an arrest is not observed in Figure 15 for Cd.
In seeking an explanation for this phenomenon it was determined that phase
transformations have been observed in Cd at approximately 3 and 6 kilobars
pressure.[29] Since the initial pressures for the impacts on Cd described in
Figures 13, 14 and 16b are 1.35 Mb, 2.50 Mb and 2.50 Mb, respectively, the
possibility of a diffusionless transformation from a high-pressure phase
induced by impact back to ambient was considered as a candidate mechanism
for the growth arrest. Such a mechanism would be influenced only by impact
pressure and by target material characteristics. Target and projectile
dimensions would not be expected to directly influence such a mechanism;
however, a comparison of D688 in Figure 14 with D775 in Figure 16b reveals
a very strong dependence of the magnitude of the arrest upon target and/or
projectile dimensions. A comparison was made of the travel time for a reflected
stress wave to return to the impact zone and of the time of arrest observed in
Figure 14 (at ~ 25 usec after impact). The total distance a reflected wave would
travel was 10.2 cm in the observed 25 μsec. The average wave velocity was
computed to be 4.0 km/sec, which compares favorably with values computed
from expressions for wave velocity[30] and from physical constants[31] for Cd:
3.5 km/sec dilational wave velocity. This observation suggests the possibility
of an interaction during the late stages of crater growth between the expanding
crater wall (and lips) with a reflected tension wave from the lateral surfaces of
the target. Such an interaction might also alter internal target stresses behind
the shock front to influence the time of occurrence of the previously proposed
phase transformation mechanism. However, upon additional examination it was
realized that the proposed crater-wall reflected-wave interaction would occur
at a rather long time after the initial compression pulse had decayed essentially
to zero. Hence, it was more likely that any phase transformation would have
already taken place before the reflected wave would reach the crater wall.

Furthermore, it is difficult to devise a mechanism for the proposed interaction which adequately explains the observed behavior. Without additional study and crater-growth data, the origin of the growth arrest in Cd must remain unresolved for the present.

e. Recovery to Final Crater Dimensions:

With reference to Figures 13 – 16 again, a brief consideration of dimensional recovery should be given here for each of the target materials tested. Table 5 summarizes this data, as taken from Figures 13 – 16. Based upon this limited amount of data, crater recovery appears to depend upon impact velocity, (seemingly and unexpectedly greater for lower velocities) and upon projectile material (seemingly greater for steel than for aluminum).

A significant point of interest was observed; namely, the effect of target strength anticipated and shown schematically in Figure 11 was manifest in a comparison of the two tests, plotted in Figure 17. (The data are plotted for each test with a time resolution of ± 0. 3 μsec. and a diametral resolution of ± 0. 05 cm). During the "hydrodynamic regime" (regime II) of crater growth, the low-strength 1100-0 Al and the high-strength 2024-T3 Al materials exhibited a common leg of the two curves, confirming initial expectations of solely hydrodynamic behavior for this regime. At approximately 10 μsec a separation of the two growth curves commences, indicating the beginning of the "transition regime" (regime III), during which conventional material strength effects become progressively more important with time. Finally, at approximately 21 and 37 μsec after impact for 2024-Al and for 1100-Al, respectively, the "equilibrium regime" (regime IV) commences. Recovery may also occur during regime IV, but in this comparison it appears that none occurred in the 2024-Al and that only a small amount (~ 5%) occurred in the 1100-Al.

f. Scaling of Crater Growth:

Scaling of crater growth was briefly investigated. One form of the physical principle of similarity states that pressure and other properties of a shock wave will be unchanged if the scales of length and time, by which the parameters are measured, are changed by the same factor. [32]   Scaling of the effect of projectile size on crater growth was tested by firing 0. 318-cm and 0. 476-cm diameter 1100-0 Al spheres at ~ 7. 4 km/sec against 1100-0 Al semi-infinite

Table 5

RECOVERY BEHAVIOR[a] OF TARGET CRATERS

Target Materials	1100-Al	2024-Al	c.p. Cd			OFHC Cu			200 Ni	
Projectile Materials	1100-Al	1100-Al	1100-Al	1100-Al	C1015 Steel	1100-Al	1100-Al	C1015 Steel	1100-Al	C1015 Steel
Impact Vel. (km/sec)	7.	7.	4.3	7.	7.	4.3	7.	7.	7.	7.
Recovery, $\delta(D_o)$, cm	0.15	~0	0.25	0.1	0.25	0.2	~0.	~0.	0.25	0.5

NOTE: (a) Extent of dimensional recovery with respect to maximum crater diameter

TR64-48
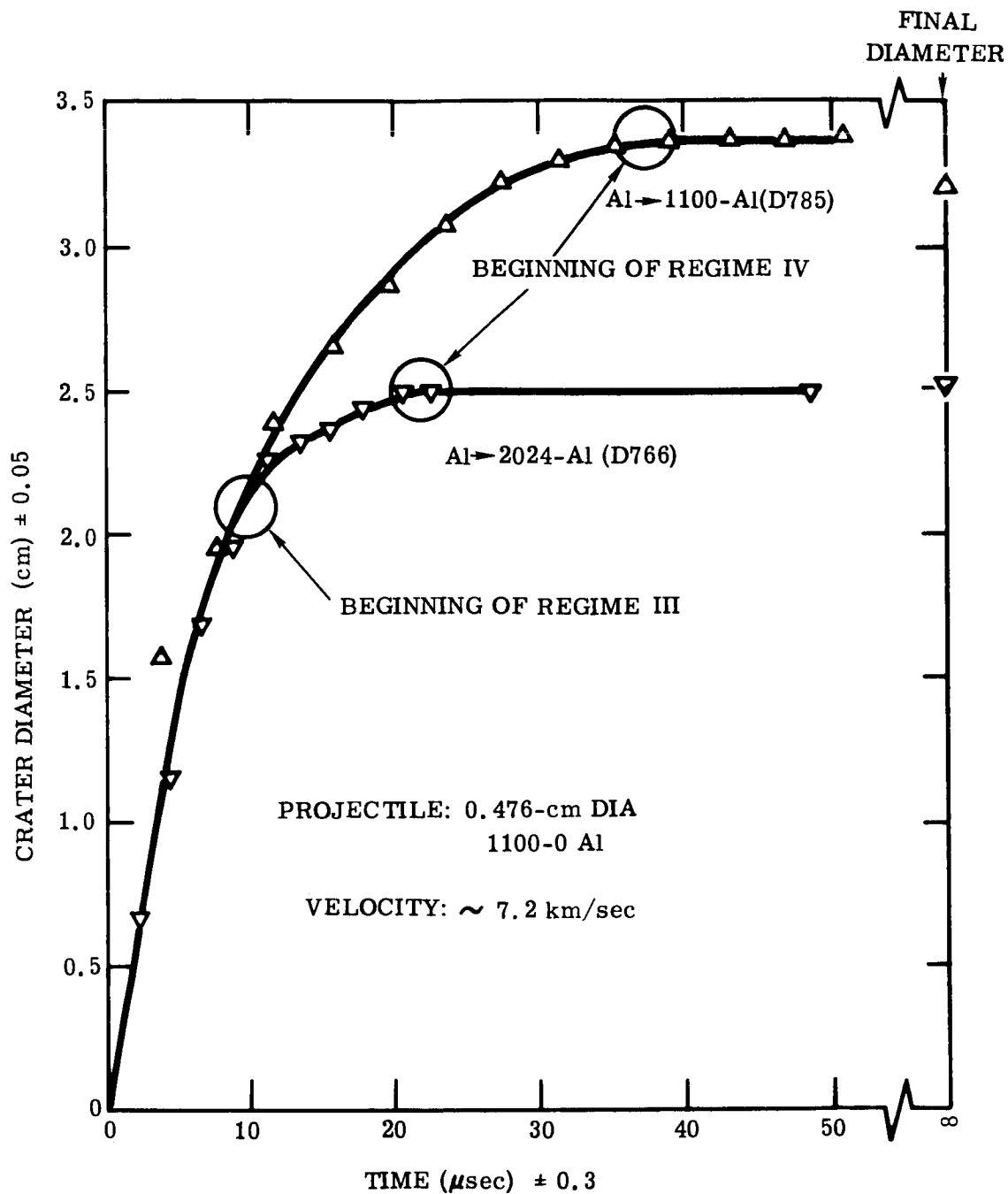
Figure 17 Effect of Target Material Strength on Crater Growth for
1100-0 Al Projectiles Against 1100-0 Al and 2024-T351
Al Semi-Infinite Targets

targets. These test results are plotted in Figure 18 according to actual and "adjusted" length and time scales. Although the initial portions do not merge as well as expected, the later and larger parts (phase IV) of the two curves do conicide very well. Hence, scaling of crater growth by scaling of projectile diameter has been tested and seems reasonably well confirmed.

g. Correlation of D_O with D_I Measurements:

Since essentially all of the observations of crater growth were made with the Beckman-Whitley camera (described in Appendix C), they were necessarily measurements of the crater outside-diameter of the lips, D_O, rather than the internal diameter, D_I, as a function of time following impact. Hence, it was necessary to determine the relationship between D_O and D_I as functions of time by taking flash X-radiographic records at certain selected times along with the B-W photographs. The experimental difficulties encountered in radiographing a 10.2-cm cube of Al during crater growth were such that only three sets of data points were obtained during the time limitation for this experimental program. Figure 19 presents the limited amount of data available at this time, together with the final "static" measurements on crater diameters. Since the available data are limited and no duplication was obtained as confirmation of the "dynamic" data points, no conclusions have been made regarding this figure.

h. Effect of Impact Velocity on Crater Parameters, $\emptyset$

In conjunction with the crater-growth results obtained during crater formation, measurements of final values of crater parameters, $\emptyset = (D_O/d,\ D_I/d,\ P/d,\ \text{or}\ V^{1/3}/d)$ were made, where

  D_O is the final minimum outside diameter of the crater lips (near the original impact surface);

  D_I is the final inside diameter of the crater at the original impact surface;

  P is the final depth of the crater, measured from the original impact surface;

  V is the final volume of the crater, measured from the original impact surface;

  d is the original diameter of the spherical projectile.

The reproducibility of the above measurements(which are recorded in Table B-1 in Appendix B) is presented in Table 6. (Measurements on initial target dimensions are within ±.01 cm; and measurements on initial projectile dimensions are within ±.003 cm.)

TR64-48
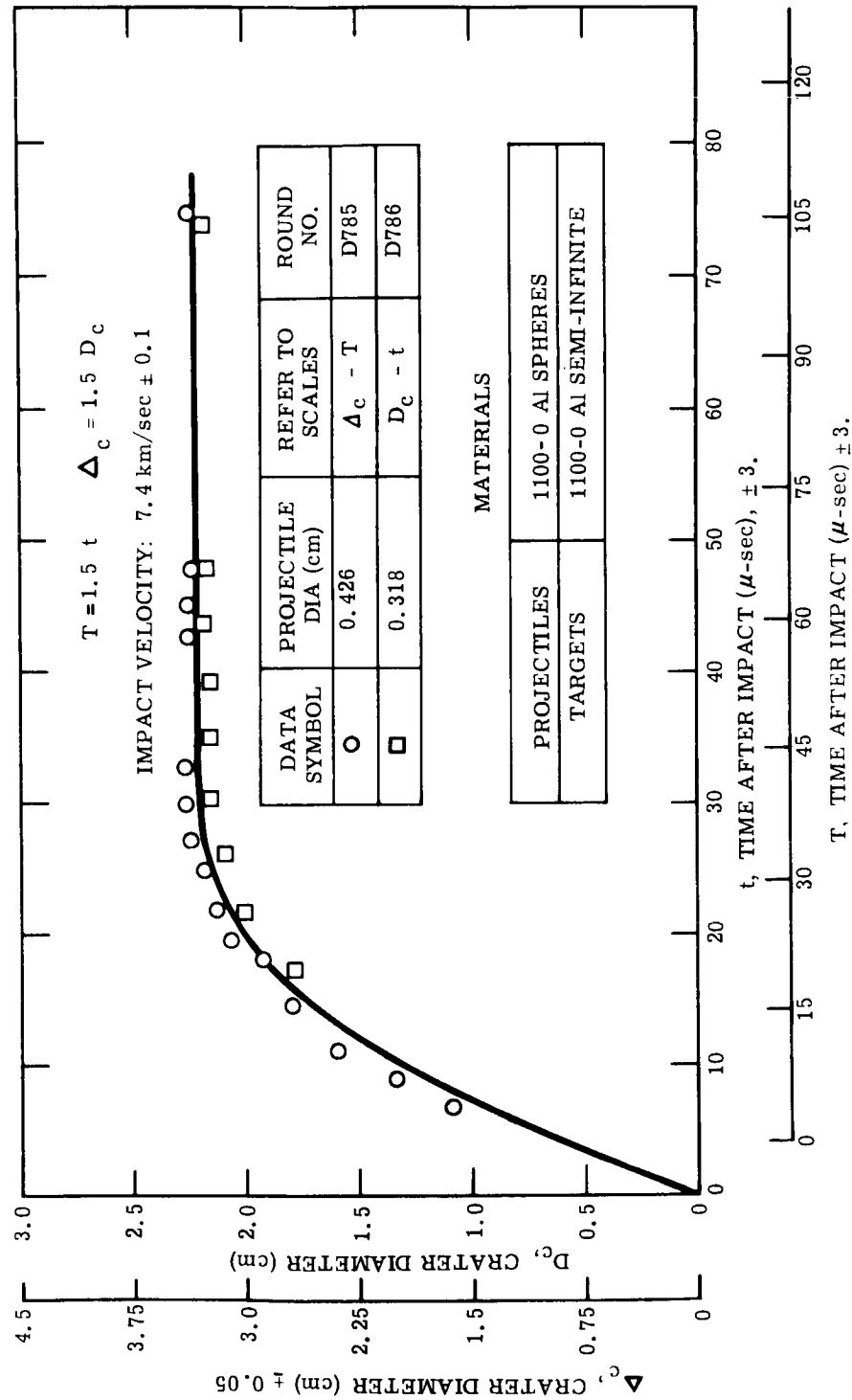
Figure 18 Scaling of Crater Growth for 1100-0 Al Projectiles Against
1100-0 Al Semi-Infinite Targets

PROJECTILE: 0.476-cm DIA.SPHERE, 1100-0 Al
IMPACT VELOCITY: ~7.3 km/sec
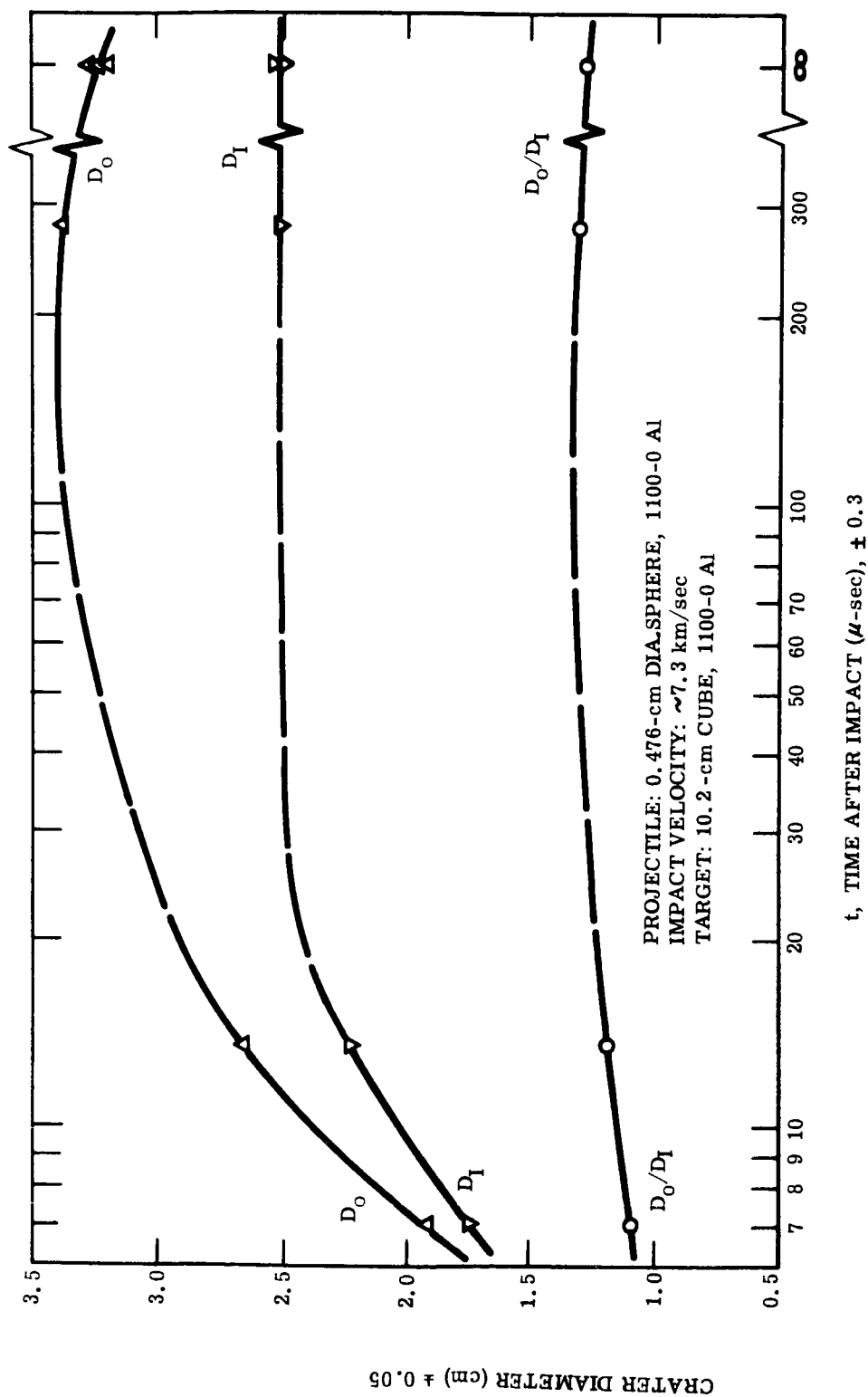TARGET: 10.2-cm CUBE, 1100-0 Al

Figure 19 Comparison of Crater Diameters and Their Ratio as Functions
of Time After Impact

TR64-48

Table 6

REPRODUCIBILITY OF

CRATER FINAL MEASUREMENTS

Measurement	Parameter	Variation[a] Noted (%)
Outside Diameter	(D_o/d)	± 1.2
Inside Diameter	(D_i/d)	± 0.8
Depth	(P/d)	± 1.1
Volume	$(V^{1/3}/d)$	± 1.1

NOTES: (a) For craters of regular, reasonable symmetrical shape; for very irregular craters (as in Cd targets) multiply these values by about "5."

The four crater parameters defined above were plotted as a function of impact velocity for Al projectiles against a variety of targets, as shown in Figures 20, 21, 22, and 23.

The following specific observations can be made in regard to the curves in Figures 20 – 23:

1) The curve for each impact couple is linear. (Where only two data points for a target metal were available, a straight line was plotted between them; justification for this procedure is based upon the linear plot of the Al-target data.)

2) The vertical descending order of the curves (order of decreasing crater parameter, ∅) was noted to match the order of increasing target material mechanical properties, as presented in Table A-3 in Appendix A. This correlation is intuitively reasonable.

3) The curve for Al ⟶ Cu in Figure 20 represents two data points for recrystallized (RX) and two for hot-worked (HW) Cu target materials. However,
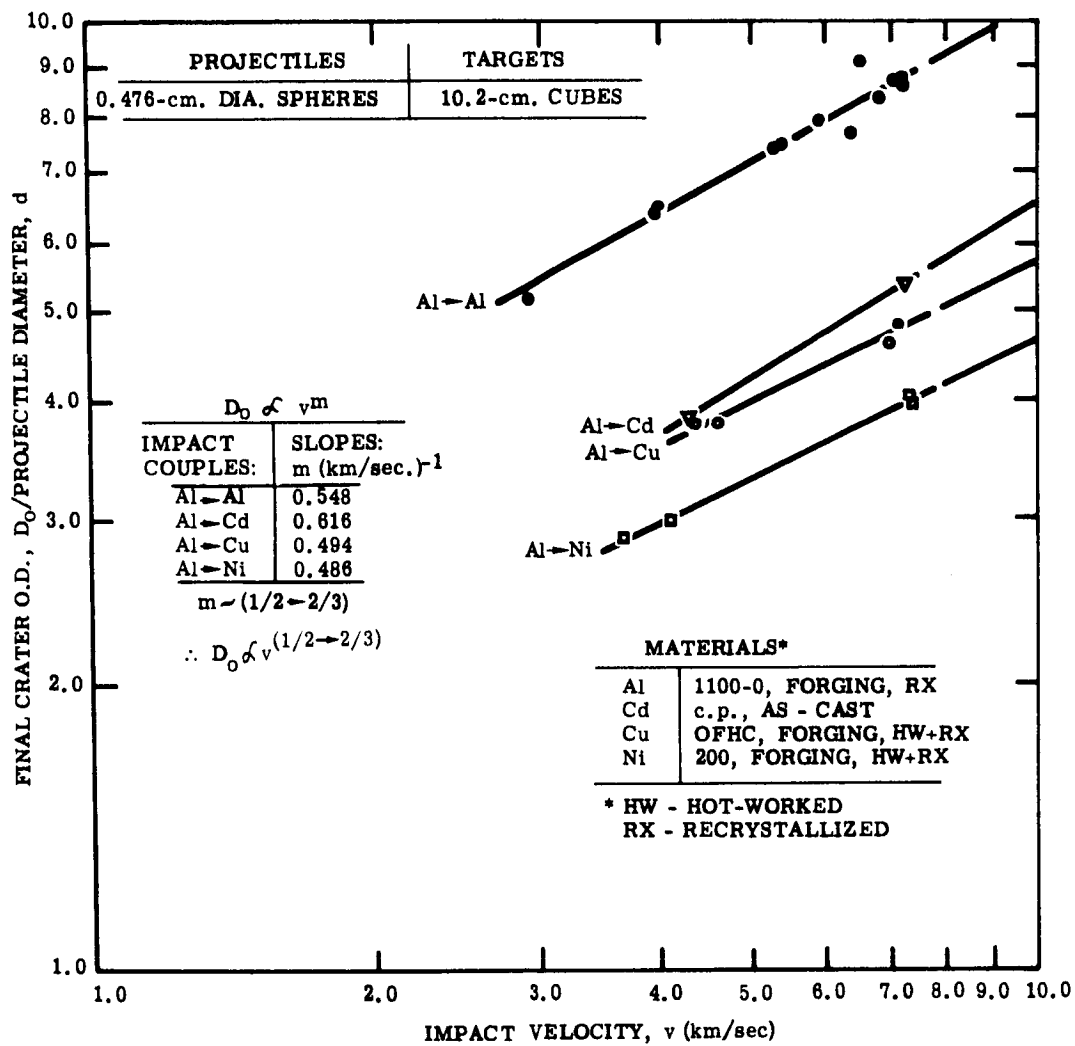
Figure 20 Crater O. D. as a Function of Impact
Velocity of Projectile
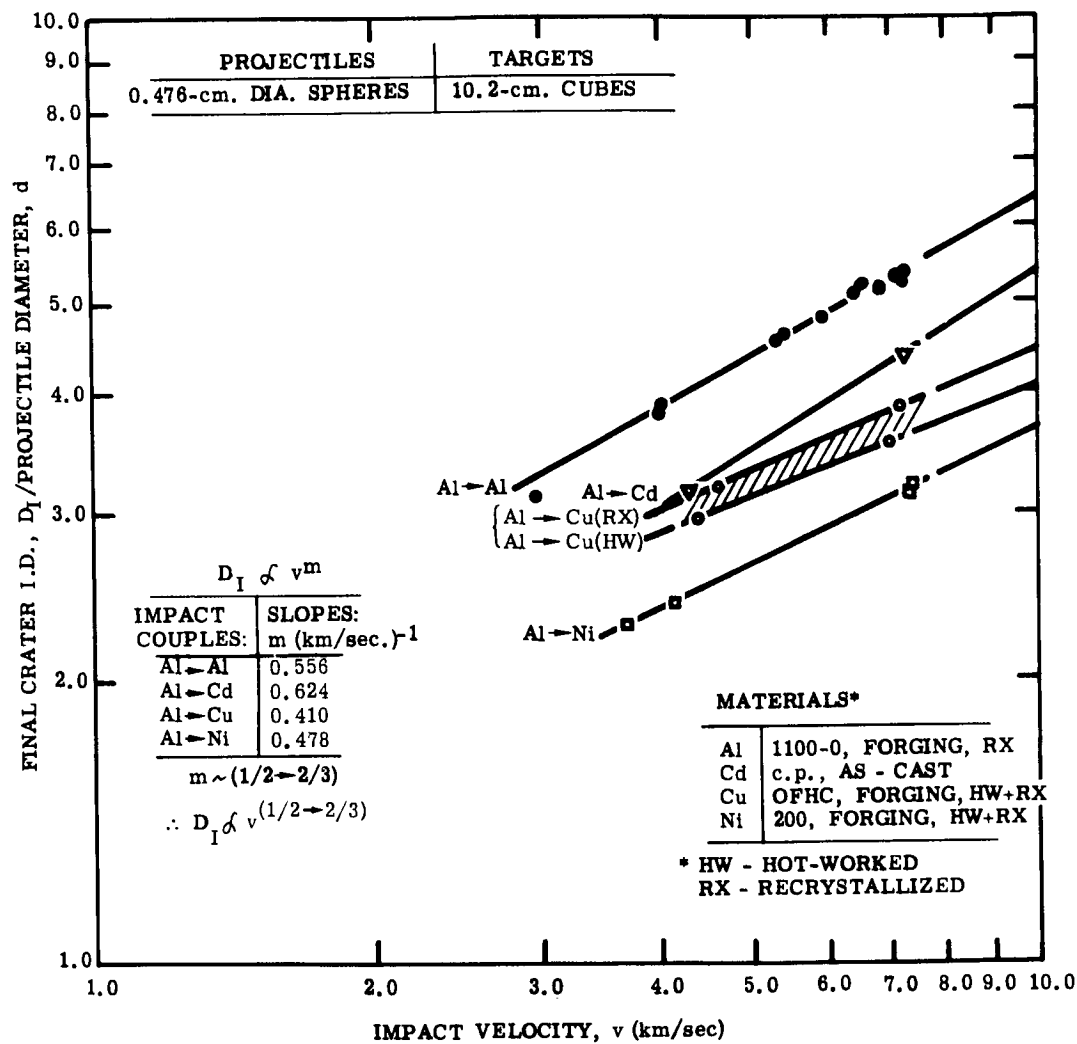
TR64-48

Figure 21 Crater I. D. as a Function of Impact
Velocity of Projectile
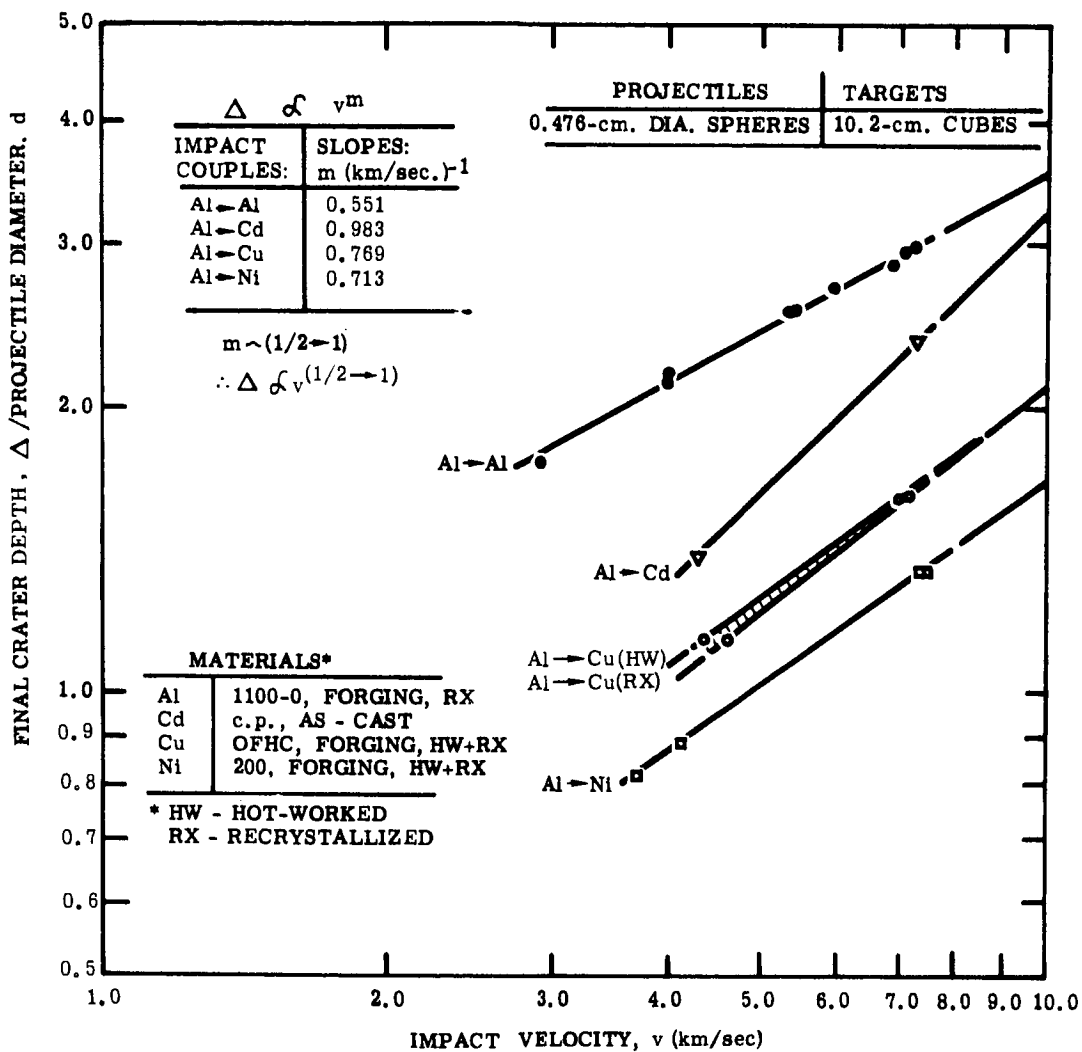
Figure 22 Crater Depth as a Function of Impact
Velocity of Projectile
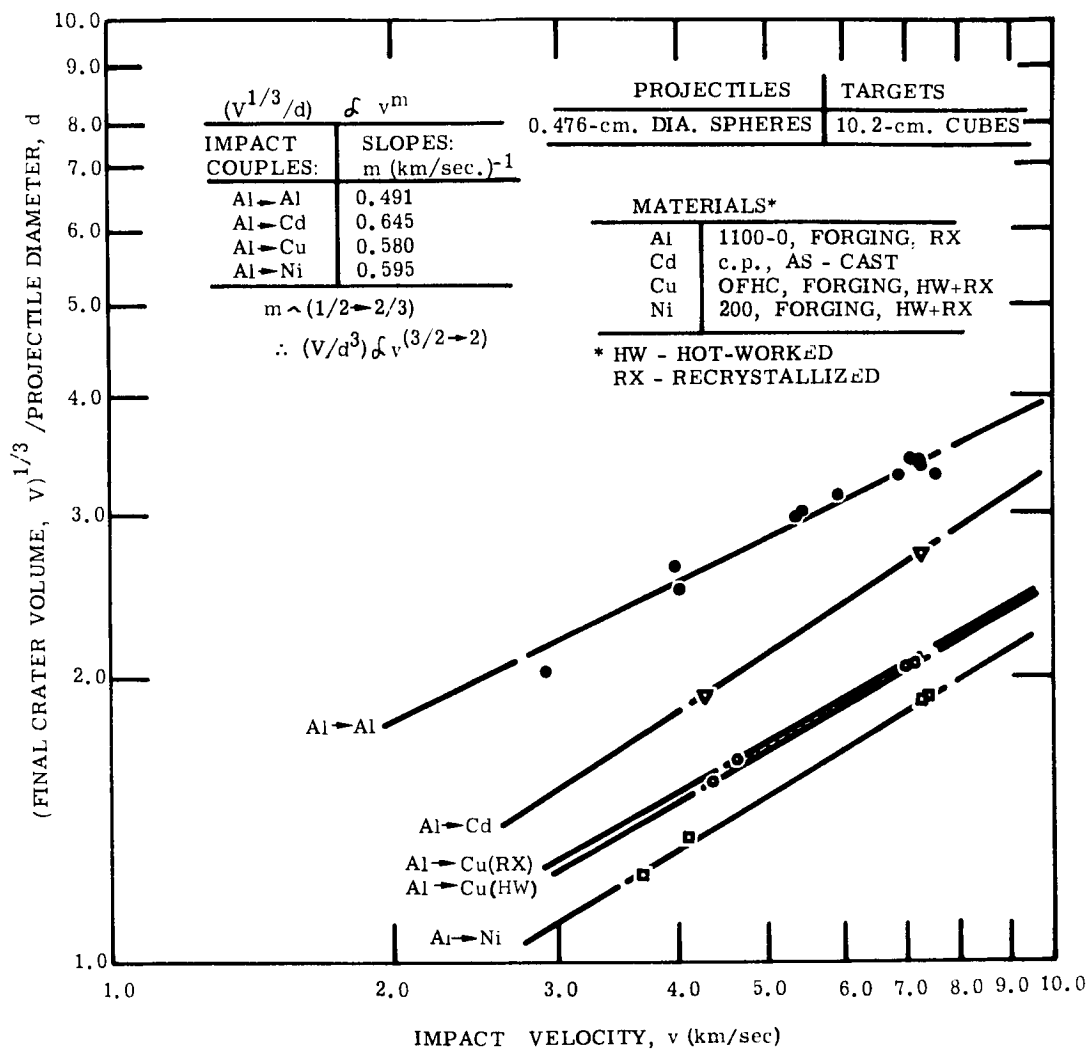
TR64-48

Figure 23 Crater Volume as a Function of Impact
Velocity of Projectile

the curves for Al→Cu in Figures 21 – 23 exhibit splitting into "doublets"; the curves in Figures 21 and 23 show Cu (RX) above the Cu (HW) material in terms of $\emptyset$ values at a given velocity, v ; the curve in Figure 22 shows the inverse order, which suggests nonhemispherical crater development. The curves for Al→Ni did not display "doublets". (A discussion of the probable origin of the "doublets" in the Al →Cu curves and the reason why Al →Ni did not also display "doublets" has been included in Appendix A).

4) The slope (velocity exponent, m) of the curves for Al→Al in Figures 20, 21 and 22 is about 0.55; but in Figure 23 it is 0.49.

5) The m-value for Al →Ni in Figures 20 and 21 is about 0.48; but it is 0.71 in Figure 22 and 0.60 in Figure 23.

6) The m-value for Al→Cu in all four figures varies appreciably, being 0.41, 0.49, 0.77 and 0.58 in Figures 20, 21, 22 and 23, respectively.

7) The m-value for Al→Cd is about 0.62 in Figures 20 and 21, and 0.98 and 0.65 in Figures 22 and 23, respectively.

On the basis of the specific observations presented above, a brief general discussion of them is made. Comparing the results of all of the four crater parameters presented in Figures 20 – 23, surprisingly good general agreement exists amongst the four. The order of the boundaries for the Al→Cu "doublet" is the same for D_I and V , but the inverse for P (and not observable for D_o – actually the Cu (RX) and Cu (HW) boundary lines intersect between 5 and 6 km/sec). The slopes of the curves in Figure 23 suggest that only for Al →Cd do we obtain $\emptyset$, (V/d^3), proportional to projectile kinetic energy, $(1/2\ mv^2)$; and that for Al →Al $\emptyset$ is proportional to $v^{1.50}$; also, that for Al→Cu $\emptyset$ is proportional to $v^{1.75}$; and that for Al →Ni $\emptyset$ is proportional to $v^{1.79}$.

i. Correlation of Final Crater Size with Target Properties:

Although the explanation for the above differences in exponents of the velocity term is not clear at this time, it is clear that the physical and mechanical properties of the target materials are significant in determining the exponent.

TR64-48

The closeness of the exponents for the Cu and Ni targets, furthermore, seems to single out yield strength (or flow stress) and/or crystal structure (both FCC) as important parameters which contrast with those for Cd targets (HCP crystal structure). The results for the Cu and Ni targets vary from those for the Al targets (also FCC crystal structure), probably due to the use of Al projectile material for all three, which would result in different initial impact pressures within the target materials. Assuming that physical/mechanical properties of the target govern regime IV of crater growth, since the value of initial impact pressure is dependent upon target material density, it is reasonable that the Al→Ni and the Al→Cu results are nearly the same, but separate from the Al→Al results, even though Al, Cu and Ni have FCC crystal structure. (Refer to Table A-3, Appendix A). Although Cd has the same density as Cu and Ni, its different crystal structure (HCP) seems to give rise to its separation from the other materials.

The results obtained for $\emptyset$ as a function of v agree generally with those of Eichelberger and Gehring.[17] They shot C1095 steel projectiles against 1100-Al Cu and Cd semi-infinite targets over a range of impact velocities (up to 12 km/sec). Their results for 1100-Al target impacts agree reasonably well with those observed in this program; however, their results for craters in Cu were reported to be slightly larger than their results for craters in Cd at a given impact velocity, seemingly inconsistent with the results reported herein. Since in this program steel projectiles were used at 7 km/sec only, it is difficult to compare more extensively the results and resolve the apparent differences.

A limited effort supplementary to this program was made to find an empirical correlation between the final crater parameters, $\emptyset$, and the physical/mechanical properties of the target materials studied. The results, though somewhat incomplete, merit a brief discussion, as follows:

1) Assume that crater parameters are proportional to kinetic energy of the impacting projectile/impact stress produced in target material; i.e., the impact energy required to produce unit impact stress in a particular material; given as:

$$\emptyset = \alpha \left(\frac{1/2 \, m_p \, v_p^2}{\sigma_I} \right) . \tag{14}$$

60

From the Hugoniots available in the literature[33] σ_I, the impact pressure, for each impact couple was determined by graphically constructing a "reflection" of the Hugoniot for the Al projectile for an impact velocity of 7. 0 km/sec which intersects with the four target materials of interest.

Table 7 compiles the results of these determinations. In this case the kinetic energy for 0. 15-gm Al projectiles impacting at 7. 0 km/sec is constant for all four couples; i. e., $(1/2 \, m_p v_p^2) = 3. 7 \times 10^4$ joules.

Table 7

IMPACT STRESS FOR VARIOUS MATERIALS AT
7 km/sec IMPACT VELOCITY

Impact Couples	σ_I, Impact Pressure (Mb)
Al $\longrightarrow$ Al	0. 98
Al $\longrightarrow$ Cd	1. 35
Al $\longrightarrow$ Cu	1. 50
Al $\longrightarrow$ Ni	1. 53

The parameters of interest were "normalized" by comparing against values for Al. Table 8 presents the raw and normalized values of $\emptyset$, the set of crater parameters. $\emptyset$ represents the average of the normalized values, which are surprisingly close.

An inspection of the last two columns in Table 8 reveals that the calculated values and the experimental values of $\emptyset$ are approaching equivalence. If one considers that the " α " term is a proportionality constant which varies in accordance with the physical/mechanical properties of the target material, then a value of " α " for each target material can be estimated to adjust the discrepancies. Table 9 summarizes the results of this effort to correlate $\emptyset$ with properties of the target material. Unfortunately, " α " represents only a forcing factor without any obvious physical significance associated with it at this time. Further sustained efforts in this direction should prove more fruitful.

TR64-48

Table 8

RAW AND NORMALIZED ϕ DATA

Impact (c) Couple	ϕ, Crater Parameter (a)				Normalized Crater Parameter, $\bar{\phi}$ (b)					$\bar{\phi}$, (d)
	D_o/d	D_i/d	P/d	$V^{1/3}/d$	$(D_o/d)_N$	$(D_i/d)_N$	$(P/d)_N$	$(V^{1/3}/d)_N$	Avg. $\bar{\phi}$	Calculated
Al→Al	6.90	5.35	2.92	3.43	1.00	1.00	1.00	1.00	1.00	1.00
Al→Cd	5.15	4.27	2.36	2.71	0.75	0.80	0.81	0.79	0.79	0.73
Al→Cu	4.68	3.75	2.01	2.08	0.68	0.70	0.69	0.61	0.67	0.66
Al→Ni	3.89	3.09	1.47	1.87	0.56	0.58	0.50	0.54	0.55	0.64

NOTES:

(a) For a 0.476-cm-diameter 1100-0 Al projectile impacting a 10.2-cm-cube target at approx. 7. km/sec; m_p = 0.15gm

(b) Crater parameter value divided by value of same crater parameter for 1100-0 Al targets.

(c) Specific gravity (simple average) for Cd, Cu and Ni is 8.84 gms/cc.

(d) Crater parameter calculated by Equation (14), and "normalized" by comparison with the value calculated for Al→Al.

Table 9

SUMMARY OF RESULTS OF CORRELATION FOR
$\bar{\phi}$ AND TARGET PROPERTIES [a]

Impact Couple	α	$\bar{\phi}$, exper'l.	$\bar{\phi}$, calc'd.
Al ⟶ Al	1.00	1.00	1.00
Al ⟶ Cd	1.08	0.79	0.79
Al ⟶ Cu	1.02	0.67	0.67
Al ⟶ Ni	1.16	0.55	0.55

NOTES: (a) 0.476-cm-diam spheres at 7.0 km/sec
against 10.2-cm cubical targets

2) A second empirical correlation has been found to give surprisingly good agreement with experiment for the FCC metals, as shown in Table 10; namely,

$$\phi = \beta\gamma \left(\frac{T}{T_m} \right) \tag{15}$$

wherein:

T is the initial test temperature;

T_m is the melting temperature of target material;

β is a proportionality factor which may be associated with target material crystal structures; and

γ is a proportionality factor which may be associated with initial impact stress.

Thus, the attempt at correlation of crater parameters with target properties using Equation (14) — although having a better physical basis for understanding — was not quite successful. However, an alternate attempt at correlation using Equation (15) — the most successful of a limited number of strictly empirical approaches attempted — was surprisingly successful. The value of the homologous temperature term, (T/T_m), acts as an indirect measure of the ease with

TR64-48

Table 10

SUMMARY OF RESULTS OF ALTERNATE CORRELATION FOR $\bar{\phi}$ AND TARGET PROPERTIES (a)

Projectile Velocity (km/sec)			7.0				4.0			
Impact Couple	Target Crystal Structure (b)	Target (T/Tm)(c)	Normalized (T/Tm)(d)	Experimental $\bar{\phi}$(e)	β	γ	Normalized (T/Tm)(d)	Experimental $\bar{\phi}$(e)	β	γ
Al⟶Al	FCC	0.323	1.00	1.00	1.0	1.0	1.00	1.00	1.0	1.0
Al⟶Cd	HCP	0.502	1.56−(2x0.78)	0.79	2.0	1.0	1.56	0.41	2.0	4.9
Al⟶Cu	FCC	0.220	0.68	0.67	1.0	1.0	0.68	0.81	1.0	1.2
Al⟶Ni	FCC	0.174	0.54	0.55	1.0	1.0	0.54	0.87	1.0	1.2

NOTES:

(a) 0.476-cm-diameter spherical projectiles against 10.2-cm cubical targets

(b) FCC: Face-centered cubic. HCP: hexagonal close-packed

(c) Homologous test temperature, (T/Tm), for the target metal

(d) Homologous test temperature for the target material "normalized" by comparison against (T/Tm) for Al

(e) Normalized values of experimental $\bar{\phi}$ from Figures 20 – 23

which target material will flow; at the test temperature the closer this term is to unity, the lower will be the target material's resistance to flow ("flow stress"); and conversely, the smaller the value of this term, the higher will be "flow stress." The significance of "β", however, is not clearly understood now, although the three FCC metals group nicely for $\beta = 1.0$, while the single HCP metal seems to require that $\beta = 2.0$ (unexpectedly also an integral value), as shown in Table 10. However, additional support for these values is to be found in the dynamic high-pressure data of Al'tshuler and his associates,[34] wherein a plot is presented of pressure as a function of relative compression (ρ/ρ_0) for a number of metals. It is significant (1) that three out of the four FCC metals reported grouped together; (2) that both of the HCP metals reported grouped together; and (3) that at a given value of relative compression, the mean value of the experimentally determined pressures shown for the FCC group is exactly twice that shown for the HCP group.

Similarly, the significance of "γ" is not clearly understood. Since γ is unity for the higher-velocity data, it is intuitively reasonable to relate γ to effects arising from "sub-hypervelocity" impacts. The initial relative dominance of the hydro-dynamic pressure term over target-strength effects is reduced considerably as impact velocity decreases below the hypervelocity range. Thus, the results at the lower velocity reflect a more complex situation (as in regime III), wherein the full effect of hydrodynamic pressure (regime II) is never fully realized. The γ term may represent the introduction of the influence of target strength, then, for "sub-hypervelocity" impact cases. As can be observed in Table 10 for 4.0 km/sec, the γ values for all three FCC target metals still are not vastly different. The Al→Cu and Al→Ni couples show higher γ values than for Al→Al, as would be expected from their initial impact stress values (derived from the Hugoniot curves for these couples). The five-fold increase in γ for Al→Cd, again, reflects the greater increase in difficulty for plastic flow in an HCP metal relative to the FCC metals.

The above correlation, based upon the factor (T/T_m), relates well to earlier experimental impact results on thin-sheet targets of Cd, Cu, and Ni and on semi-infinite targets of Cd and Cu.[35] For crater growth in these target materials T_m was found to be significant, also.

CONCLUSIONS AND RECOMMENDATIONS

A considerable amount of basic information was derived during this program from the experimental results obtained. This basic information correlates with several theoretical/phenomenological models described in the literature.

The throw-off-pellet technique, used for measuring maximum shock pressure in 1100-0 aluminum, was found to be superior to other techniques surveyed for measuring pressures of 0.3 Mbars and below. Good agreement was found between experimental values and those predicted from theoretical analyses by Riney and Heyda, thereby verifying the assumptions used in these analyses. Thus, it is possible to accurately determine the shock pressure generated by impact into aluminum and, very likely, into other materials as well. Since target material strength has been neglected for theoretical analyses of hyper-velocity impact, it is recommended that additional shock pressure measurements be made for aluminum alloys having higher strength than the 1100-0 aluminum studied herein and for other materials. Such additional data will more fully evaluate theoretical analyses available in the literature and will permit the calculation of correction factors, if necessary, for engineering purposes.

The momentum transferred to aluminum semi-infinite targets by hypervelocity impact with aluminum projectiles was measured successfully. Experimental results are in good agreement with a semi-empirical approach by Staniukovich. These results indicate also that momentum multiplication is due to the particulate mass ejected from targets mainly during the latter stages of the interaction and crater formation. It is recommended that additional hypervelocity impact studies of momentum transfer be conducted at velocities higher than 7 km/sec with aluminum and other semi-infinite target materials. Such studies would determine the velocity-power dependence of the multiplication factor such as defined by the hydrodynamic calculations.

TR64-48

Experimental data obtained during and after crater growth exhibited three distinct stages of the growth process, which correlate with the phenomenological model described in the Introduction. The effect of target strength on crater growth, as anticipated early in this program, was demonstrated to be significant and controlling in the third regime of crater formation for 1100-0 and 2024-T3 aluminum. No correlation with conventional properties is apparent for the first two regimes of crater growth. However, in the fourth (and last) regime a decreasing order of crater dimensional parameters at any velocity between 4 and 7 km/sec correlates with an increasing order of target material physical/mechanical properties. For the OFHC copper targets a small difference in strength level due to a difference in strain-hardened condition resulted in a detectable difference in crater dimensions. Two approaches to correlation of crater parameters with target properties have been presented. The semi-empirical approach correlating with target homologous test temperature was the more satisfactory of the two. The principle of self-similarity was demonstrated to be applicable to the crater-growth process for 1100-0 aluminum targets. A preliminary effort, which is only partially complete at this time, was made to correlate internal and external crater diameters. Since the bulk of the crater-growth data obtained are collected by observations of external crater diameter, it is recommended that the correlation between internal and external diameters be completed for aluminum targets and that a technique be devised to accomplish the same correlation for more dense target materials. In order to more clearly define the nature of the initial stages of crater formation, it is recommended that further study of these regimes be conducted for aluminum and other target materials.

A recommended study which includes the above recommendations is outlined as follows:

Determine pressure profiles along projectile flight axis by throw-off-pellet technique for 1100-0 and 2024-T3 aluminum targets, and observe pellet velocities as a function of angle with respect to the flight axis.

Study the crater growth process (the initial regimes especially) in 1100-0 and 2024-T3 aluminum targets using high-speed photographic and flash X-radiographic techniques.

Determine axial momentum transfer and target mass loss as a function of projectile diameter for 1100-0 aluminum targets using the ballistic pendulum system.

Compare the effect of iron projectiles with that of 1100-0 aluminum on the results obtained in the three areas recommended above.

ACKNOWLEDGEMENTS

REFERENCES

1. J. W. Gehring, "Observations of the Phenomena of Hypervelocity Impact," Proceedings of the Fourth Symposium on Hypervelocity Impact, APGC-TR-60-39, Eglin AFB, Florida Sep 1960

2. D. R. Christman, et al: "Study of the Phenomena of Hypervelocity Impact," GM Defense Research Laboratories Report No. TR63-216, Summary Report on Contract No. NAS8-5067, Jun 1963

3. F. L. Whipple, "On Meteoroids and Penetration," J. Geophys. Res., 68, No. 17, 1 Sep 1963 pp. 4929 – 4938

4. E. Opik, "Researches on the Physical Theory of Meteor Phenomena: I. Theory of the Formation of Meteor Craters," Acta et Comm. Univ. Tartuensis, 1936

5. G. Grimminger, "Probability That a Meteorite Will Hit or Penetrate a Body Situated in the Vicinity of the Earth," J. Appl. Phys., Vol. 19, No. 10, Oct 1948, pp. 947 – 956

6. E. M. Pugh, G. Birkhoff, D. P. MacDougall, and G. Taylor, "Explosives With Lined Cavities," J. Appl. Phys., Vol. 19, No. 6, Jun 1948, pp. 563 – 582

7. N. Rostocker, "The Formation of Craters by High Speed Particles," Meteoritics, Vol. 1, 1953

8. R. W. Goranson, et al., "Dynamic Determination of the Compressibility of Metals," J. Appl. Phys., Vol. 26, No. 12, Dec 1955, pp. 1472 – 1479

9. J. J. Gilvarry and J. E. Hill, "The Impact of Large Meteorites," Astrophys. J., Vol. 124, 1956, pp. 610 – 622

10. M. A. Cook, "Mechanism of Cratering in Ultra-High Velocity Impact," J. Appl. Phys., Vol. 30, No. 5, May 1959, pp. 725 – 735; also, The Science of High Explosives, Reinhold Publishing Co., New York, 1958

11. K. P. Staniukovich, "Elements of Impact Theory for Solid Bodies Having High (Cosmic) Speeds," ARS J., Russian Supplement, Vol. 32, No. 9, Sep 1962, pp. 1459 – 1473

12. M. Zaid, "Penetration by Hypervelocity Projectiles," Proceedings of the Fifth Symposium on Hypervelocity Impact, Vol. 1, Part 1, Nonr-(G)-0020-62(X), Colorado School of Mines, Apr 1962

13. R. L. Bjork, "Effects of a Meteoroid Impact on Steel and Aluminum in Space," The Rand Corporation, Report TR P-1662, 16 Dec 1958

14. J. W. Walsh and J. H. Tillotson, "Hydrodynamics of Hypervelocity Impact," General Dynamics Corporation, General Atomic Division, Report GA-3827, 22 Jan 1963 (work reported in this paper was presented at the Sixth Hypervelocity Impact Symposium, Cleveland, Ohio, Apr 30 – May 2, 1963)

15. T. D. Riney, and T. F. Heyda, "Penetration of Structures by Hypervelocity Projectiles," Proceedings of the 17th AMRAC Meeting, Apr 1964

16. J. W. Gehring and D. W. Sieck, "Reaction of the Lunar Surface to the Impact of a Lunar Probe," Progress in Astronautics and Aeronautics, Vol. 10, Technology of Lunar Exploration, pp. 97 – 136, Academic Press, New York, 1963; for a more complete discussion, see J. W. Gehring and R. L. Warnica, "An Investigation of the Phenomena of Impact Flash and Its Potential Use as a Hit Detection and Target Discrimination Technique," Proceedings of the 6th Symposium on Hypervelocity Impact, Vol. II, Part 2, DA-31-124-ARO(D)-16, Firestone Tire and Rubber Co., Aug 1963

17. R. J. Eichelberger and J. W. Gehring, "Effects of Meteoroid Impacts on Space Vehicles," ARS J., Vol. 32, No. 10, Oct 1962, pp. 1583 – 1591

18. J. H. Kineke, "Observations of Crater Formation in Ductile Materials," Proceedings of the Fifth Symposium on Hypervelocity Impact, Vol. 1, Part 2, Nonr-(G)-0020-62(X), Colorado School of Mines, Apr 1962

19. B. G. Karpov, "Transient Response of Wax Targets to Pellet Impact at 4 km/sec.," Ball. Res. Labs. Report No. 1226, Oct 1963

20. V. M. Boyle, "Transient Hypervelocity Impact Phenomena in a Transparent Target," Ball. Res. Labs. Report No. 1567, May 1964

21. C. M. Glass and R. B. Pond, "a Metallurgical Approach to the Hypervelocity Problem," Proceedings of the Fourth Symposium on Hypervelocity Impact, Vol. 3, APGC-TR-60-39, Eglin Air Force Base, Florida, Sep 1960; also, "Energy Balances in Hypervelocity Penetration" (paper presented at the Sixth Hypervelocity Impact Symposium, Cleveland, Ohio, Apr 30 – May 2, 1963)

22. J. H. Tillotson, GM Defense Research Laboratories, Private Communication

23. M. H. Rice, et al.: "Compression of Solids by Strong Shock Waves," Solid State Physics., Vol. 6, Academic Press, Inc., N. Y., 1958

24. J. M. Walsh, et al.: "Theory of Hypervelocity Impact," Quarterly Technical Report (Feb – Apr 1963), General Atomic Div., General Dynamics Corp

25. J. H. Tillotson, "Notes on Momentum Multiplication in Hypervelocity Impact," GM Defense Research Laboratories, Private Communication

26. K. P. Staniukovich, "Concerning the Impact of Solids at High Velocities," J. Exper. Theor. Phys. (USSR), 36, 1959, p. 1605

27. T. D. Riney, Proceedings of the Sixth Symposium on Hypervelocity Impact, Vol. II, Pt. 1, Cleveland, Ohio, 30 Apr – 2 May 1963, p. 138

28. W. J. Rae and H. P. Kirchner, Ibid, p. 210

29. P. W. Bridgman, The Physics of High Pressure, G. Bell & Sons, 1949, p. 235

30. J. C. Jaeger: Elasticity, Fracture and Flow, J. Wiley & Sons, N. Y., 2nd ed., 1961

31. C. J. Smithells, Metals Reference Book, Vols. I and II, Butterworth, Inc., Washington, 3rd ed., 1962

32. L. I. Sedov: Similarity and Dimensional Methods in Mechanics, Academic Press, ed. by M. Holt, English translation of 4th edition, 1959

33. R. G. McQueen and S. P. Marsh, "Equation of State for Nineteen Metallic Elements from Shock-Wave Measurements to Two Megabars," J. Appl. Phys., 31, 1960, p. 1253

34. L. V. Al'tshuler, et al.: "Dynamic Compressibility of Metals under Pressure from 400,000 to 4,000,000 Atmospheres," Soviet Physics JETP, 34(7), No. 4 (Oct. 1958); Figure 5

35. C. J. Maiden, et al.: "Investigation of Fundamental Mechanism of Damage to Thin Targets by Hypervelocity Projectiles," GM Defense Research Laboratories Report No. TR63-225, Final Report on USN Research Laboratories Contract No. 3891(00)(X), ARPA Order No. 70, May 1964

APPENDIXES

APPENDIX A

DESCRIPTION OF MATERIALS STUDIED
AND THEIR PROPERTIES

The target and projectile materials employed in this program are described and characterized in the following tabulations for the purpose of documenting the material parameters and their influence on crater growth.[*]

1. Chemical Analyses

In Table A-1 the chemical analyses provided by vendor certifications are compiled.

2. Thermal/Mechanical Processing

In Table A-2 the thermal/mechanical processing history of these metals is reported.

3. Macro-/Microstructures

In Figures A-1 through A-7 are shown typical macrostructures (at 12X) and microstructures (at 83X) resulting from the thermal/mechanical processing of the metals described above.

The 1100-Al was to have been provided by the vendor in the fully annealed (recrystallized) condition. Inspection of the microphotos in Figure A-1 reveals an unrecrystallized microstructure resulting from only partial (recovery) annealing.

OFHC copper is presented in two sets of photos (as-hot-forged in Figure A-4; as-recrystallized in Figure A-5) for the purpose of comparing the two types of copper target materials which exhibited slightly different cratering behavior. Differences in these two microstructures were subtle and were not immediately obvious; however, one important difference appears to be the relative degree

---

* Material designations defined in Table A-1.

of recrystallization in each. The "hot-worked" material was 25–50% recrystallized; whereas the intentionally "recrystallized" Cu was more than 90% recrystallized, accounting somewhat for the slightly different tensile properties reported in Table A-3 and the slight difference in cratering behavior depicted in Figures 21, 22, and 23 in the main body of this report. Allison, et al, have reported a similar behavior for the annealing of Cu targets. The 200-Ni, in the as-received "hot-worked" condition, appears to have been recrystallized almost completely by the vendor's short-time anneal immediately after hot-forging and prior to the GM DRL "recrystallization" anneal. Hence, a difference in cratering behavior did not arise for the Ni targets as a result of subjecting some of them to the latter anneal, as was the case for the Cu targets.

4. Physical/Mechanical (Static) Properties

In Table A-3 are presented the physical and the low-strain-rate mechanical properties reported by vendor certification, by measurements at GM DRL, and/ or by nominal "hand-book" values (in the absence of specific measurements on the lots of metal tested).

5. Dynamic Mechanical Properties

The incipient spall threshold was investigated for the two types of aluminum used during this investigation (1100 and 2024). The evaluation of this dynamic characteristic of materials was made by using flat plate experiments. Figure A-8 is a simplified sketch of the experimental arrangement. A thin circular plate of metal, the thin impactor, is affixed at the front part of a hollow plexiglass sabot. The sabot-thin-impactor assembly is accelerated by means of a compressed-air gun to strike a thin target located at the muzzle of the gun. If the velocity of the impactor is increased by successive steps, a critical velocity will be reached at which a tension fracture will form in the target, such as designated by "Expected Spall" in Figure A-8. If the impactor is of the same material as the target, and if it has a free rear surface, the incipient spall threshold of the target material at zero-stress level is calculated by using the following relation with experimental results from the above technique:

$$\sigma_c = \rho \cdot c \cdot \frac{v}{2} \quad , \tag{A-1}$$

wherein σ_c is the stress at which the incipient spall is observed, ρ is the density of the target, c is the elastic-wave velocity in the target,and v is the impactor velocity. The spall thickness is found to be the same as the thickness of the impactor. The values of spall thresholds of 1100-0 Al and 2024-T3 Al were found to be, respectively 10.7 and 11.9 kbars.

TR64-48
APPENDIX A

Table A-1

CHEMICAL ANALYSES OF METALS STUDIED

Metal	Principal Alloying or Impurity Elements Reported (Wt. %)
1100-Al [a]	.01 Cr, .13 Cu, .39 Fe, .01 Mg, .01 Mn, .04 Si, .01 Ti, .02 Zn; bal Al.
2024-Al [b]	.10 Cr, 3.8-4.9 Cu, .50 Fe, 1.2-1.8 Mg, .30-.9 Mn, .50 Si, .25 Zn; others: .05 Each, .15 total; bal. Al.
c.p. Cd [c]	99.9% Cd (minimum).
OFHC Cu [d]	99.92% Cu (minimum).
200 Ni [e]	.08 C, .02 Cu, .08 Fe, .32 Mn, .006 S, .09 Si, 99.38 or bal. Ni.
C1015 Steel [f]	.13-.18 C, .30-.60 Mn, .040 P (max.), .050 S (max.); bal. Fe.

NOTES:

(a) Commercial-purity aluminum is designated "1100-Al."

(b) One of the commonly used aluminum-alloy structural metals is designated "2024-Al."

(c) Commercial-purity cadmium.

(d) Commercial-purity copper; Oxygen-Free, High-Conductivity metal.

(e) Commercial-purity nickel is designated "200 Ni" (formerly "A Ni").

(f) A plain-carbon steel containing nominally .15% carbon.

Table A-2

THERMAL/MECHANICAL PROCESSING OF METALS STUDIED

Metal	Description of Processing
1100-Al	Upset-forged from 8-5/16-in. D x 7-3/4-in., rough-turned, as-cast ingot into 8-in.-sq. x 6-in. blocks; minimum reduction 2:1; annealed at ~650°F for 3 hrs., followed by air quench.
2024-Al	Bare, hot-rolled plate; two pieces: 6-in. x 8-in. x 14-1/8-in. and 6-in.-sq. x 36-in. Processing in accordance with QQA-355.
c.p. Cd	Open-cast block.
OFHC Cu	Upset-forged from 10-in. D x 5-1/2-in. round bar in range 1400° – 1600°F; water-quenched to room temperature, finishing as "hot-worked" block. Several targets recrystallized from this material by annealing for 2-1/2 hrs. at ~750°F in air, followed by furnace-cooling to room temperature.
200 Ni	Upset-forged from 8-3/4-in. D x 7-1/2-in. round bar in range 2000° – 2300°F; air-cooled to room temperature. (As-forged BHN: 100 – 170.) Annealed for 5 min. at 1400° – 1450°F; and then heated to 1700°F momentarily before air-cooling to room-temperature, finishing as "hot-worked" block. (As-annealed BHN:90 – 120.) Several targets recrystallized from this material by additional annealing for 2-1/2 hrs. at ~1400°F in air, followed by furnace-cooling to room temperature.
C1015 Steel	Hot-worked (rolled) to 1/2-in. D x 96.0-in. round bar.

TR64-48
APPENDIX A

Table A-3

PHYSICAL/MECHANICAL PROPERTIES(a) OF METALS STUDIED

Metal	Source	Heat No.	Yield Stress (psi x 10^-3)	U.T.S. (psi x 10^-3)	Elastic Modulus (psi x 10^-6)	Hardness(b) (DPH)	Specific Gravity	Bulk Modulus (psi x 10^-6)	Modulus of Rigidity (psi x 10^-6)	Crystal Structure(c)	m.p. (°K)	Heat of Fusion (cal./gm.)	b.p. (°K)	Heat of Vaporization (cal./gm.)
1100-Al (0)	E.M. Jorgenson Co.	A8-253	6.4	13.	10.2	27.	2.70	9.5	3.9	FCC	933.	93.	2723.	2510.
2024-Al (T3)	U.S. Steel Corp.	07046	36. (d)	48. (d)	10.6	~145.	2.90	9.8	4.0	FCC	~923.	~96.	~2673.	~2510.
c.p. Cd (As-cast)	Belmont Smelting &Refining Works	09533	5.3	7.3	9.0	20.	8.65	10.7	3.3	HCP	594.	13.	1038.	286.
OFHC Cu {HW(e)/RX}	E.M. Jorgenson Co.	0717	14.3(b) / 13.7(b)	28.3(b) / 28.1(b)	18.0	58.	8.96	21.9	6.2	FCC	1356.	49.	2868.	1150.
200 Ni (Recrystall'd)	E.M. Jorgenson Co.	U4213A	30.	70.	30.0	~118.	8.90	26.3	11.5	FCC	1726.	72.	3003.	1550.
C1015 Steel (Hot-Worked)	Hopper Machine Works	18344	38.	49.	29.5	~140.	~7.75	23.7	11.6	BCC	~1793.	~69.	~3273.	~1510.

NOTES:
(a) Room temperature values, except for last four columns.
(b) GM DRL measurements.
(c) FCC: face-centered cubic. HCP: hexagonal closed-packed. BCC: body-centered cubic.
(d) Vendor certification.
(e) HW: hot-worked. RX: recrystallized.
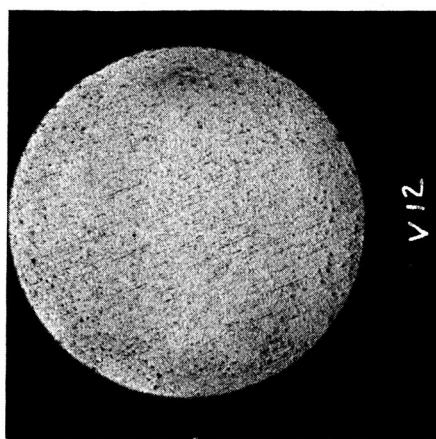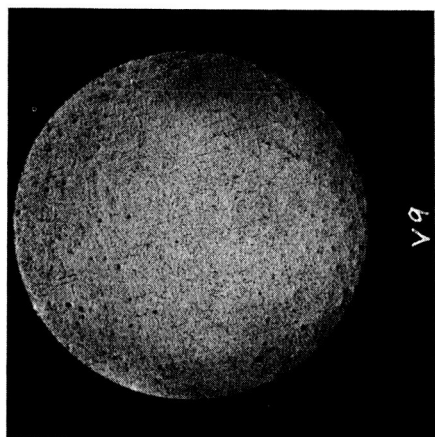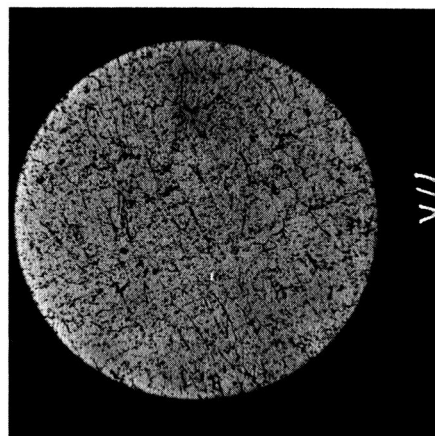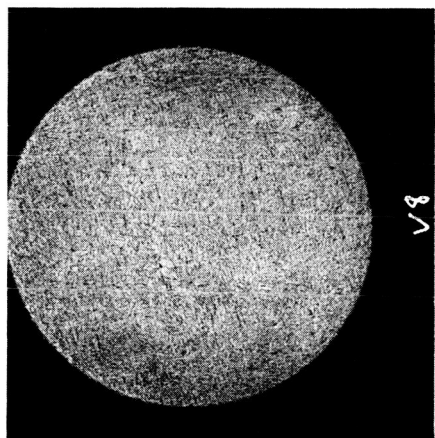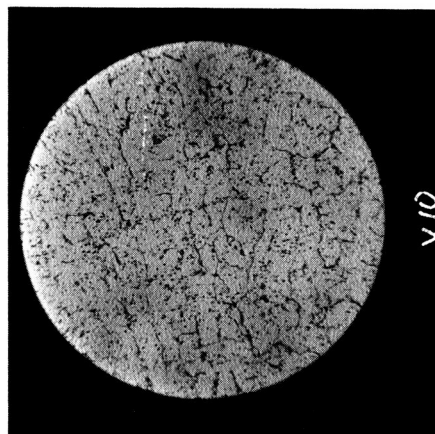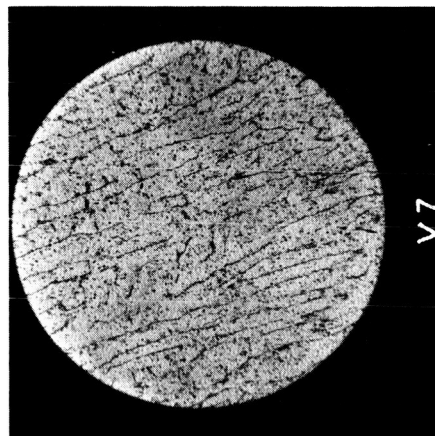
Figure A-1 "1100" Aluminum Sections, As-Forged; Three Orthogonal
Directions, Two Magnifications

TR64-48
APPENDIX A

"C" DIRECTION

"B" DIRECTION

"A" DIRECTION

12X

83X
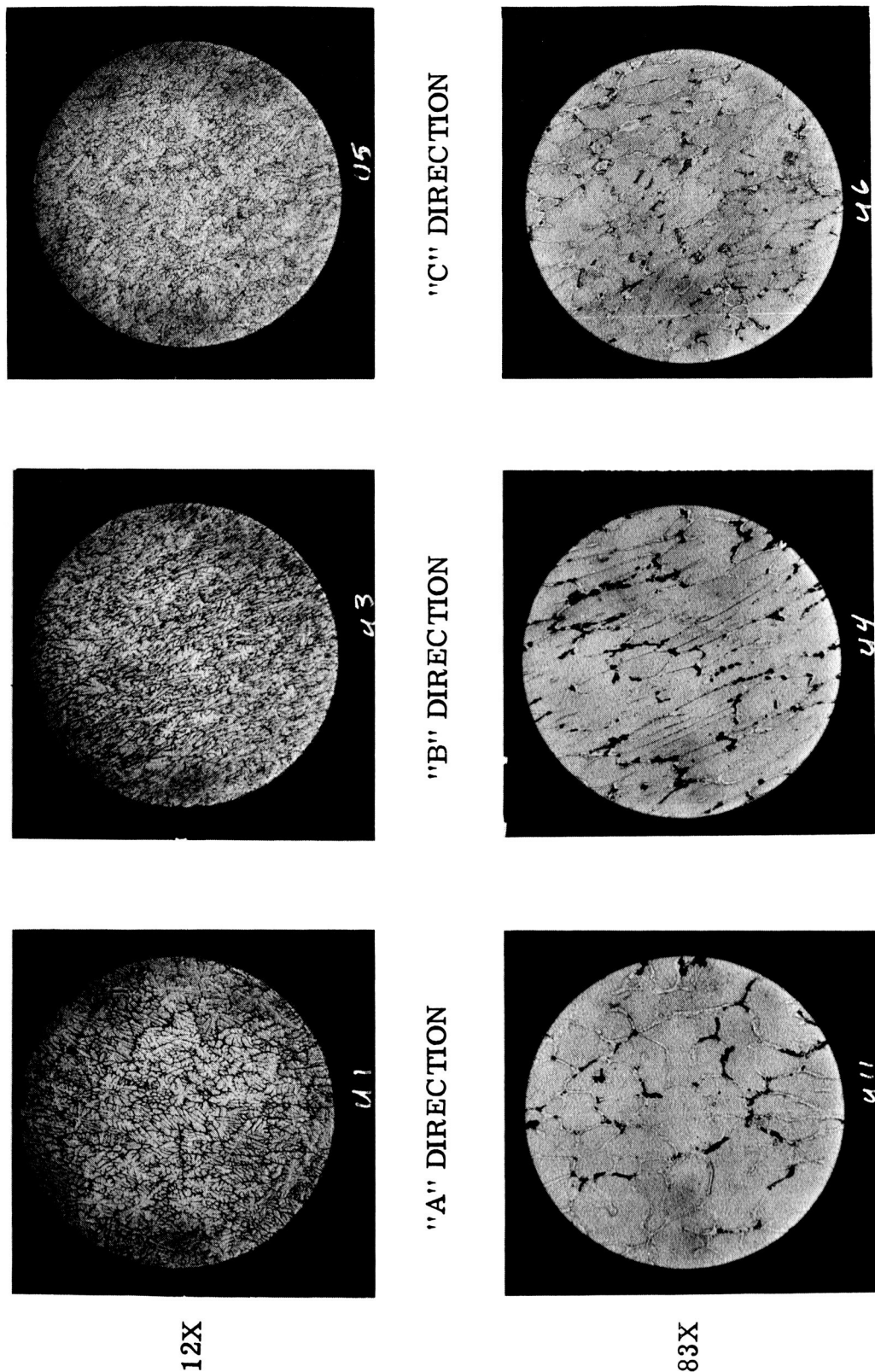
Figure A-2   "2024" Aluminum Alloy Sections, "T351" Condition; Three
Orthogonal Directions, Two Magnifications
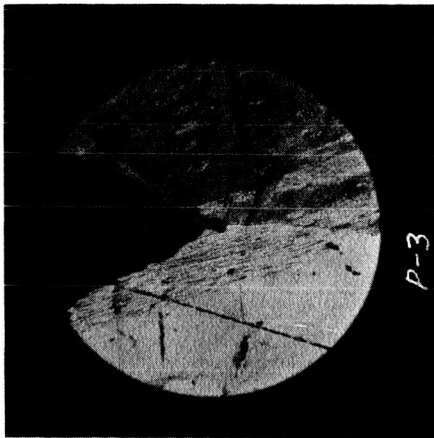
Figure A-3 "c.p." Cadmium Sections, As-Cast; Three Orthogonal Directions, Two Magnifications

TR64-48
APPENDIX A

"C" DIRECTION

"B" DIRECTION

"A" DIRECTION

12X

83X
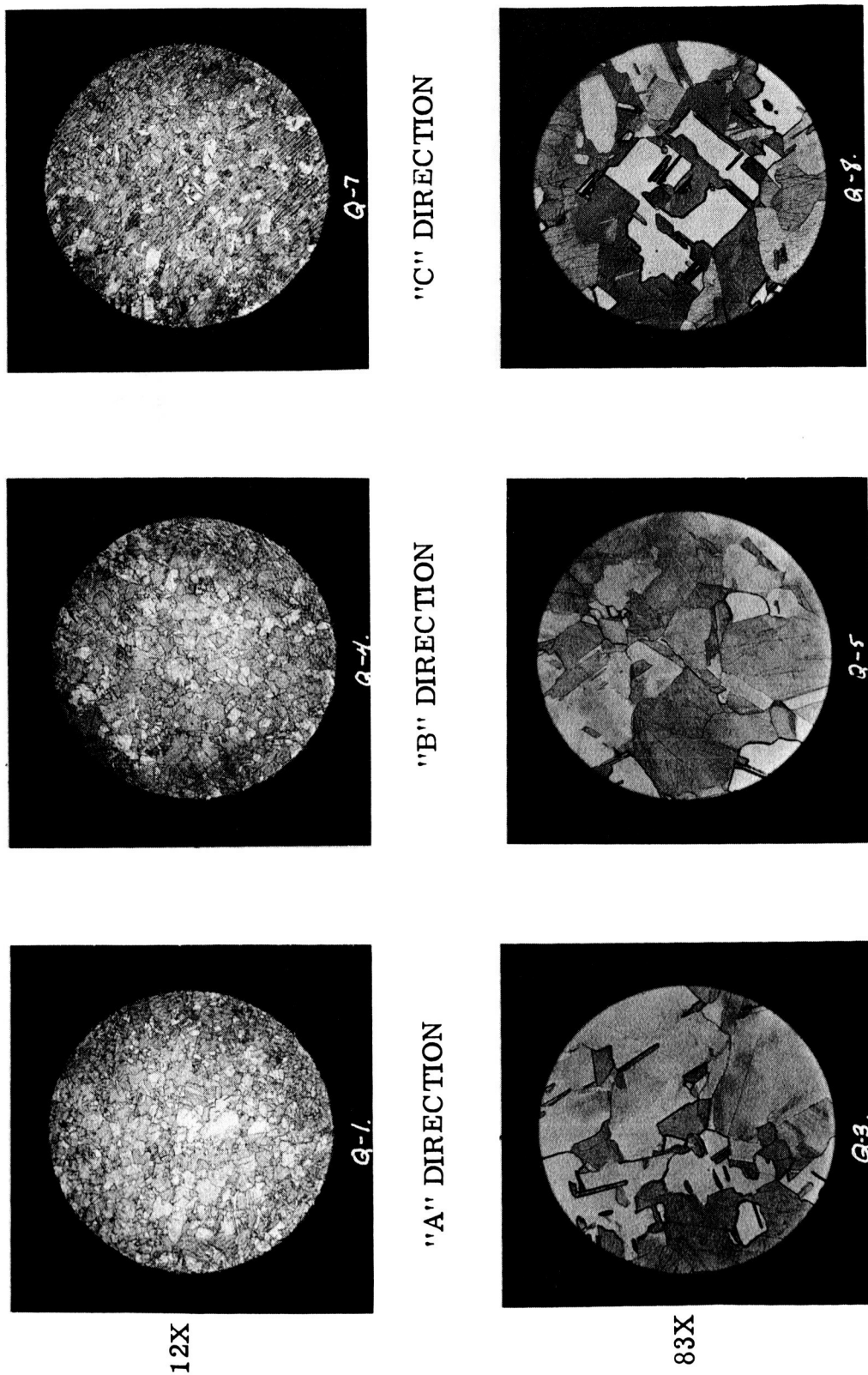
Figure A-4 "OFHC" Copper Sections, As-Hot-Forged; Three Orthogonal Directions, Two Magnifications.

"C" DIRECTION

"B" DIRECTION

"A" DIRECTION

12X
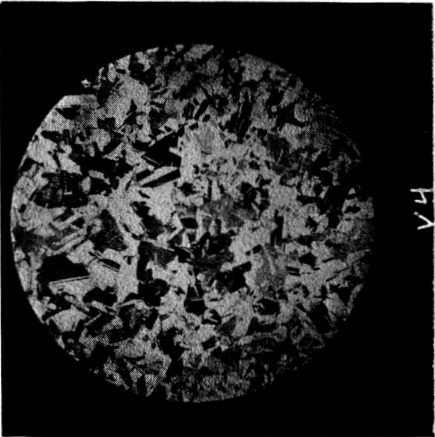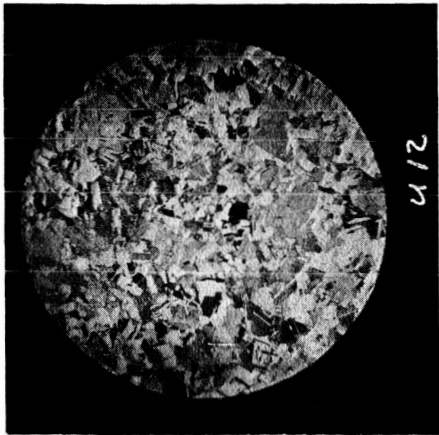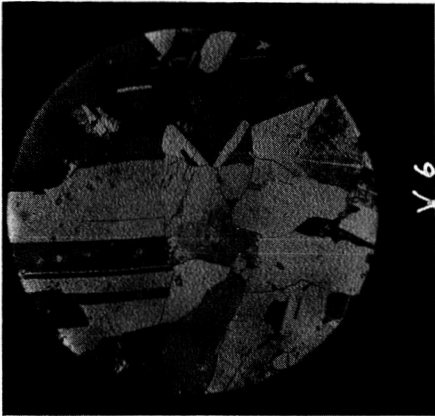
83X
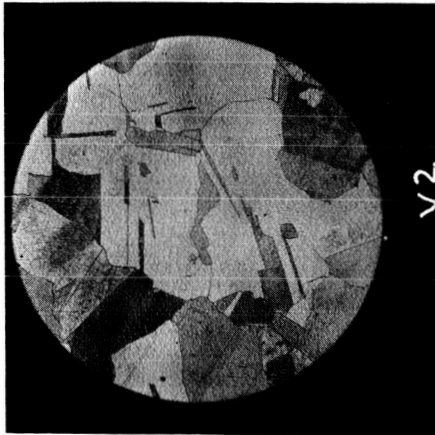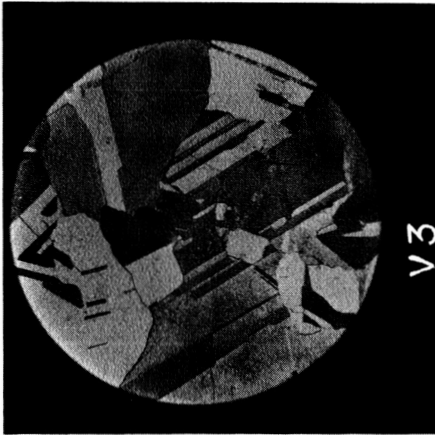
Figure A-5   "OFHC" Copper Sections, As-Recrystallized; Three Orthogonal
Directions, Two Magnifications
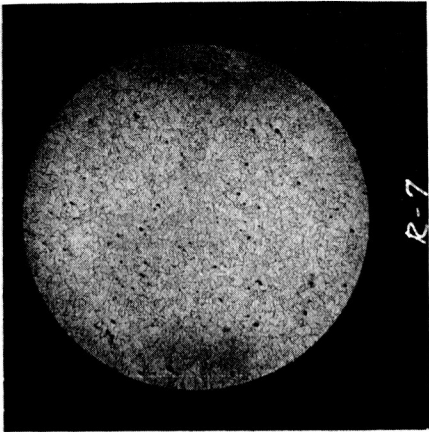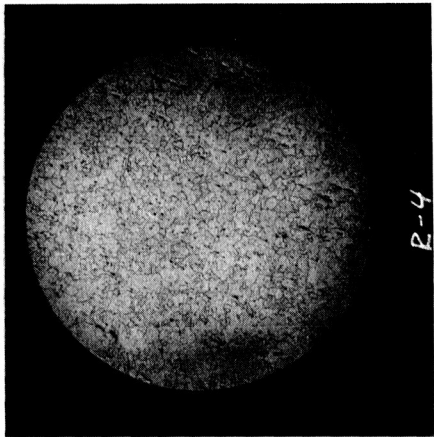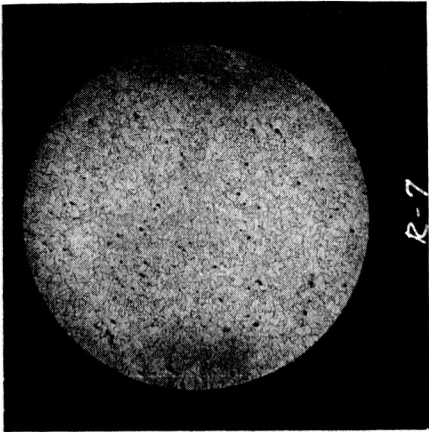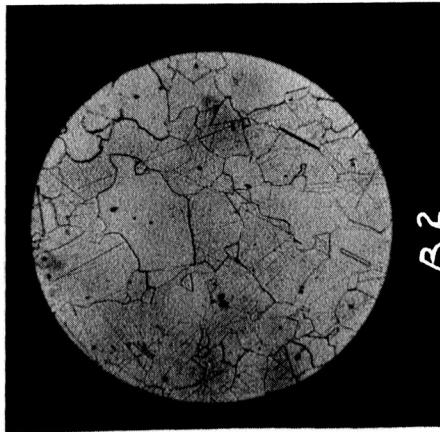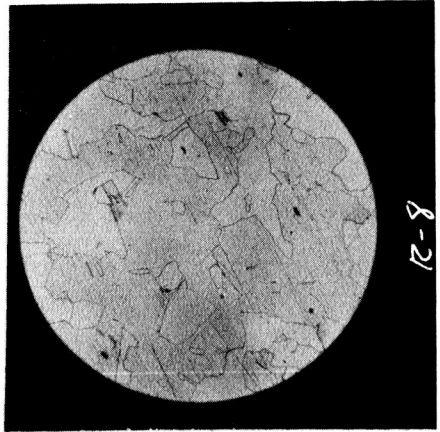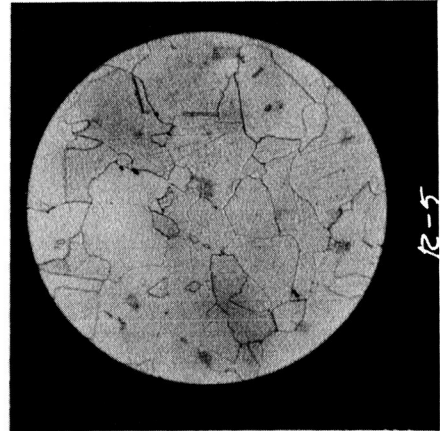
Figure A-6 "200" Nickel Sections, Recrystallized; Three Orthogonal Directions, Two Magnifications
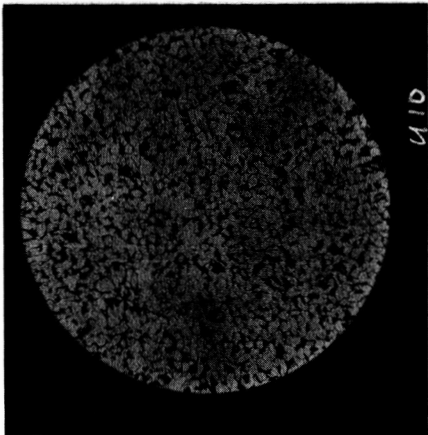
LONGITUDINAL DIRECTION

12X

83X
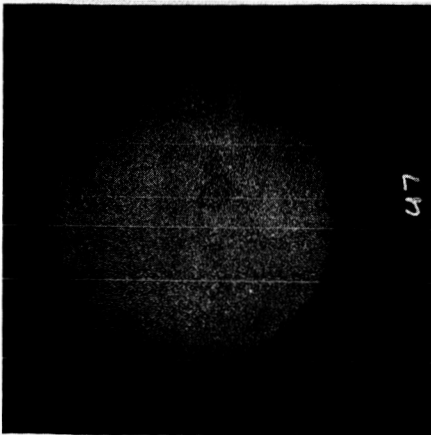
TRANSVERSE DIRECTION
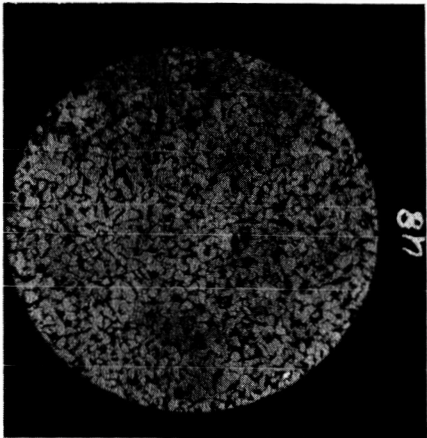
Figure A-7   C1015 Steel Sections, Hot-Worked Round Bar; Two Orthogonal
Directions, Two Magnifications
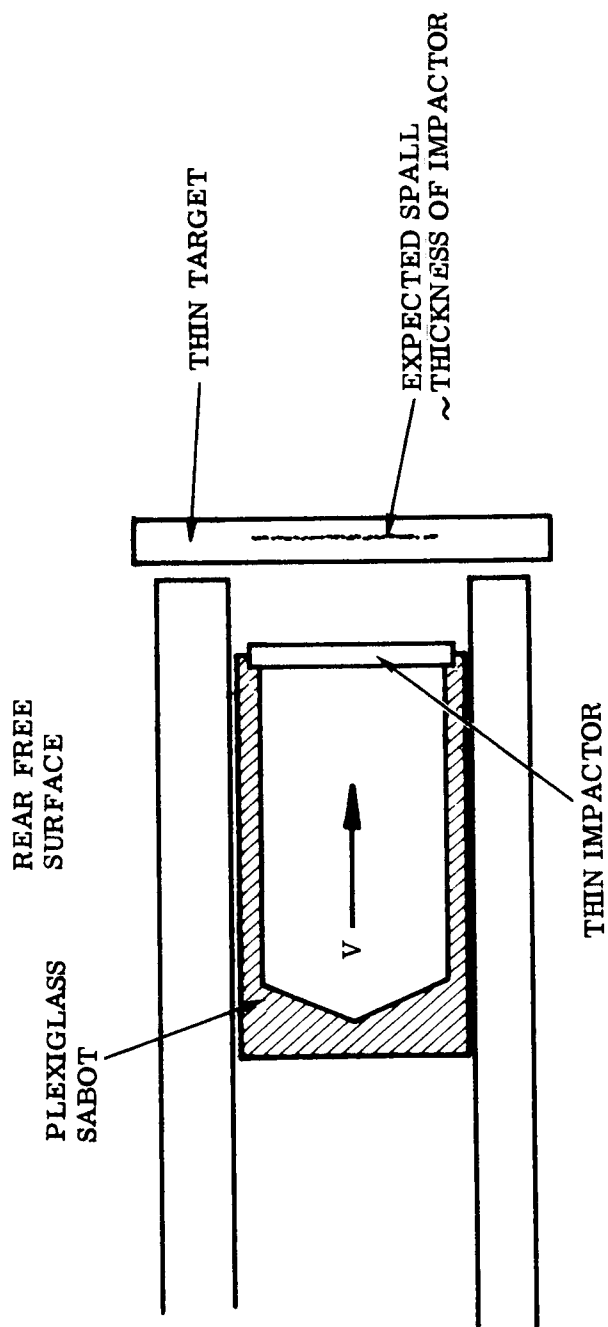
TR64-48
APPENDIX A

Figure A-8 Flat Plate Experiments

APPENDIX B

TARGET, PROJECTILE, AND CRATER DATA

(Table B-1)

TR64-48
APPENDIX B

Table B-1
TARGET, PROJECTILE AND CRATER DATA

TARGET			PROJECTILE				CRATER				
Material & Condition	Size (cm.)	Wgt. Loss (gms.)	Mat'l. & Cond'n.	Size (O.D.,cm)	Wgt. (gms)	Velocity (km/s)	Vol. (cc)	Depth (cm)	O.D.(a) (cm)	I.D.(b) (cm)	Round No. (D-)
Cu, OFHC, As-hot-forged	10.2 cube	1.5 ± .5	Al, 1100-0	0.476	0.1546	7.00	0.95	0.76	2.18	1.68	642
Cu, OFHC, As-hot-forged	10.2 cube	2.5 ± .5	Al, 1100-0	0.476	0.1542	4.39	0.40	0.54	1.78	1.40	649
Cu, OFHC, As-hot-forged	10.2 cube	(-)0.3 - 0.8 ± .5	Steel, C1015, H/R	0.318	0.1319	6.77	1.19	0.92	2.19	1.65	650
Cu, OFHC, As-recrystall'd.	10.2 cube	0.8 ± .5	Steel, C1015, H/R	0.318	0.1293	6.80	1.13	0.90	2.14	1.63	652
Cu, OFHC, As-recrystall'd.	10.2 cube	0.7 ± .5	Al, 1100-0	0.476	0.1535	4.61	0.46	0.54	1.80	1.52	653
Cu, OFHC, As-recrystall'd.	10.2 cube	---	Al, 1100-0	0.476	0.1539	(No impact. Bad Shot)					654
Cu, OFHC, As-recrystall'd.	10.2 cube	(-) 0.5 ± .5	Al, 1100-0	0.476	0.1532	7.19	0.96	0.77	2.28	1.83	656
Al, 1100-0	10.2 cube	(on Ball. Pend.)	Al, 1100-0	0.476	0.1574	4.03	1.65	1.03	2.38	1.85	657
Al, 1100-0	10.2 cube	(on Ball. Pend.)	Al, 1100-0	0.476	0.1577	(No impact. Bad Shot)					658
Al, 1100-0	10.2 cube	(on Ball. Pend.)	Al, 1100-0	0.476	0.1577	(No impact. Bad Shot)					659
Al, 1100-0	10.2 cube	(on Ball. Pend.)	Al, 1100-0	0.476	0.1578	3.99	1.75	1.02	2.36	1.82	660
Al, 1100-0	10.2 cube	(on Ball. Pend.)	Al, 1100-0	0.476	0.1577	5.31	2.83	1.20	2.77	2.16	661
Al, 1100-0	10.2 cube	(on Ball. Pend.)	Al, 1100-0	0.476	0.1577	5.43	2.97	1.21	2.80	2.19	662
Al, 1100-0	10.2 cube	(on Ball. Pend.)	Al, 1100-0	0.476	0.1577	5.95	3.32	1.27	2.95	2.29	663
Al, 1100-0	10.2 cube	(on Ball. Pend.)	Al, 1100-0	0.476	0.1577	6.41	(Sabot Hit. Crater Spoiled.)		~2.86	~2.42	664
Al, 1100-0	10.2 cube	(on Ball. Pend.)	Al, 1100-0	0.476	0.1577	6.56	(Sabot Hit. Crater Spoiled.)		~3.39	~2.46	665
Al, 1100-0	10.2 cube	(on Ball. Pend.)	Al, 1100-0	0.478	0.1577	6.87	3.85	1.35	3.12	2.45	666
Al, 1100-0	10.2 cube	(on Ball. Pend.)	Al, 1100-0	0.476	0.1577	7.29	~4.10	(Sabot Hit)	3.29	2.55	667
Al, 1100-0	10.2 cube	(on Ball. Pend.)	Al, 1100-0	0.476	0.1577	(No impact. Bad Shot)					671
Al, 1100-0	10.2 cube	(on Ball. Pend.)	Al, 1100-0	0.476	0.1576	7.10	4.35	1.39	3.26	2.52	672
Al, 1100-0	10.2 cube	(on Ball. Pend.)	Al, 1100-0	0.476	0.1577	(No impact. Bad Shot)					673
Al, 1100-0	10.2 cube	(on Ball. Pend.)	Al, 1100-0	0.476	0.1582	(Sabot hit. Crater Spoiled.)					674
Al, 1100-0	10.2 cube	(on Ball. Pend.)	Al, 1100-0	0.476	0.1581	2.91	0.90	0.83	1.92	1.48	675

NOTES: (a) Minimum O.D. of crater lips. (b) Average I.D. of crater at original surface.

Table B-1 (continued)

TARGET			PROJECTILE				CRATER				Round
Material & Condition	Size (cm.)	Wgt. Loss (gms.)	Mat'l. & Cond'n.	Size (O.D.,cm)	Wgt. (gms)	Velocity (km/s)	Vol. (cc)	Depth (cm)	O.D.(a) (cm)	I.D.(b) (cm)	No. (D-)
Ni, 200, As-hot-forged	10.2 cube	---	Al, 1100-0	0.476	0.1535	4.12	0.26	0.42	1.42	1.14	678
Ni, 200, As-hot-forged	10.2 cube	---	Al, 1100-0	0.476	0.1544	7.33	0.72	0.64	1.91	1.49	679
Ni, 200, As-hot-forged	10.2 cube	---	Steel, C1015, H/R	0.318	0.1316	(Sabot hit. Crater Spoiled.)					680
Ni, 200, As-hot-forged	10.2 cube	---	Steel, C1015, H/R	0.318	0.1345	6.84	0.70	0.79	1.80	1.41	681
Ni, 200, Recrystallized	10.2 cube	---	Steel, C1015, H/R	0.318	0.1323	6.84	0.73	0.78	1.80	1.42	682
Ni, 200, Recrystallized	10.2 cube	---	Al, 1100-0	0.476	0.1533	7.40	0.65	0.64	1.88	1.51	683
Ni, 200, Recrystallized	10.2 cube	---	Al, 1100-0	0.476	0.1553	3.69	0.20	0.39	1.36	1.08	684
Cd, c.p., As-cast	10.2 cube	---	Al, 1100-0	0.476	0.1548	4.29	0.75	0.66	1.82	1.50	685
Cd, c.p., As-cast	10.2 cube	---	Al, 1100-0	0.476	0.1548	(Vel. not obtained. Bad Shot)					686
Cd, c.p., As-cast	10.2 cube	---	Steel, C1015, H/R	0.318	0.1345	(Vel. not obtained. Bad Shot)					687
Cd, c.p., As-cast	10.2 cube	---	Steel, C1015, H/R	0.318	0.1339	6.77	2.55	1.12	2.57	2.02	688
Cd, c.p., As-cast	10.2 cube	---	Al, 1100-0	0.476	0.1549	7.29	2.15	1.12	2.52	2.09	689
Al, 2024-T351	8.9 hex x 10.2 long	2.87 ± .25	Al, 1100-0	0.476	0.1551	7.13	2.22	0.95	2.51	1.91	766
Cd, c.p., As-cast	5.1 cube	7.59 ± .02	Al, 1100-0	0.476	0.1551	6.87	Sabot Hit	~1.50	~2.39	~2.05	767
Cd, c.p., As-cast	5.1 cube	---	Steel, C1015, H/R	0.318	0.1295	(Vel. not obtained. Bad Shot)					773
Al, 1100-0	10.2 x 10.2 x 3.55 slab	---	Al, 1100-0	0.476	0.1545	7.04	"Throw-off-Pellet Shot"				774
Cd, c.p., As-cast	5.1 cube	6.77 ± .02	Steel, C1015, H/R	0.318	0.1306	6.99	~2.25	~1.21	~2.63	~2.11	775
Al, 1100-0	8.9 hex x 10.2 long	1.17 ± .02	Al, 1100-0	0.476	0.1547	7.25	4.22	1.41	3.21	2.51	785
Al, 1100-0	8.9 hex x 8.9 long	---	Al, 1100-0	0.318	0.0458	7.28	Sabot hit. Crater Spoiled.				786
Al, 1100-0	10.2 x 10.2 x 2.5 slab	---	Al, 1100-0	0.476	0.1538	7.20	"Throw-off-Pellet Shot"				791
Cd, c.p., As-cast	5.1 cube	6.92 ± .02	Steel, C1015, H/R	0.318	0.1332	6.82	~2.87	~1.18	~2.54	~2.09	792
Al, 1100-0	10.2 x 10.2 x 3.05 slab	---	Al, 1100-0	0.476	0.1543	7.36	"Throw-off-Pellet Shot"				793
Al, 1100-0	10.2 x 10.2 x 3.55 slab	---	Al, 1100-0	0.476	0.1547	7.42	"Throw-off-Pellet Shot"				794
Al, 1100-0	8.9 hex - 7.62 long	0.58 ± .02	Al, 1100-0	0.318	0.0463	7.52	3.82	1.07	2.19	1.98	795

TR64-48
APPENDIX B

Table B-1 (continued)

TARGET			PROJECTILE				CRATER				
Material & Condition	Size (cm.)	Wgt. Loss (gms.)	Mat'l. & Cond'n	Size (O.D., cm)	Wgt. (gms)	Velocity (km/s)	Vol. (cc)	Depth (cm)	O.D.(a) (cm)	I.D.(b) (cm)	Round No.(D-)
Al, 2024-T351	10.2 cube	---	Al, 1100-0	0.476	0.1562	7.41	"Ball.Pend.Valve Trial Shot"				797
Al, 1100-0	10.2 x 10.2 x 1.91 slab	---	Al, 1100-0	0.476	0.1555	7.37	"Throw-off-Pellet Shot"				803
Al, 1100-0	10.2 x 10.2 x 1.52 slab	---	Al, 1100-0	0.476	0.1543	7.28	"Throw-off-Pellet Shot"				804
Al, 1100-0	10.2 cube	---	Al, 1100-0	0.476	0.1568	(Vel. not obtained. Bad Shot)					813*
Al, 1100-0	10.2 cube	---	Al, 1100-0	0.476	0.1551	7.38	(No X-Ray/B&W. Bad Shot)				815*
Al, 1100-0	10.2 cube	---	Al, 1100-0	0.476	0.1557	7.30	(No X-Ray/B&W. Bad Shot)				826*
Al, 1100-0	10.2 x 10.2 x 0.76 slab	---	Al, 1100-0	0.476	0.1554	5.40	"Throw-off-Pellet Shot"				828*
Al, 1100-0	10.2 cube	---	Al, 1100-0	0.476	0.1551	7.08	"X-Ray/B&W Correlation Shot"				832*
Al, 1100-0	10.2 x 10.2 x 1.02 slab	---	Al, 1100-0	0.476	0.1541	7.29	"Throw-off-Pellet Shot"				833*
Al, 1100-0	10.2 x 10.2 x 0.76 slab	---	Al, 1100-0	0.476	0.1545	7.11	"Throw-off-Pellet Shot"				834*
Al, 1100-0	10.2 cube	---	Al, 1100-0	0.476	0.1559	7.19	"X-Ray/B&W Correlation Shot"				835*
Al, 1100-0	10.2 cube	---	Al, 1100-0	0.476	0.1558	(Vel. not obtained Bad Shot)					836*
Al, 1100-0	10.2 cube	---	Al, 1100-0	0.476	0.1545	7.16	"X-Ray/B&W Correlation Shot"				837*

* Shots made on GM DRL funds.

APPENDIX C
DESCRIPTION OF GM DRL IMPACT RANGE EQUIPMENT

This research program was conducted predominantly by tests on free-flight range "D" at GM DRL. This range utilizes an accelerated-reservoir light-gas gun, normally with a 0.30-inch-diameter launch tube.

1. RANGE D

Impact Range D is used only for horizontal launches with the ARLG gun. This range, shown in Figures C-1 and C-2, consists of the following major components:

     (1) 1.0-in. inside diameter by 18-ft long pump tube

     (2) accelerated-reservoir high-pressure coupling

     (3) 0.30-in. inside diameter by 6-ft long launch tube

     (4) 16-ft long section with blast tanks

     (5) velocity station section

     (6) 5-ft long by 3-ft diameter impact chamber.

Performance characteristics of the 0.30-caliber ARLG gun are given in Figure C-3.

2. VELOCITY MEASUREMENT

After being fired from the ARLG gun, the projectile passes through an instrumented flight chamber, where the velocity, position, attitude, and condition of the model during its flight are recorded by spark shadowgraph photographs. Spark shadowgraph instrumentation stations (velocity stations) are located along the flight axis of the range, and orthogonal shadowgraphs are taken at each of these stations. The optical axis of each station is located in a plane perpendicular to the range axis, and the orthogonal axes are at an angle of 45° from the vertical axis, allowing each station to record longitudinal, lateral, and vertical direction as well as the model's attitude about the pitch and yaw axes.
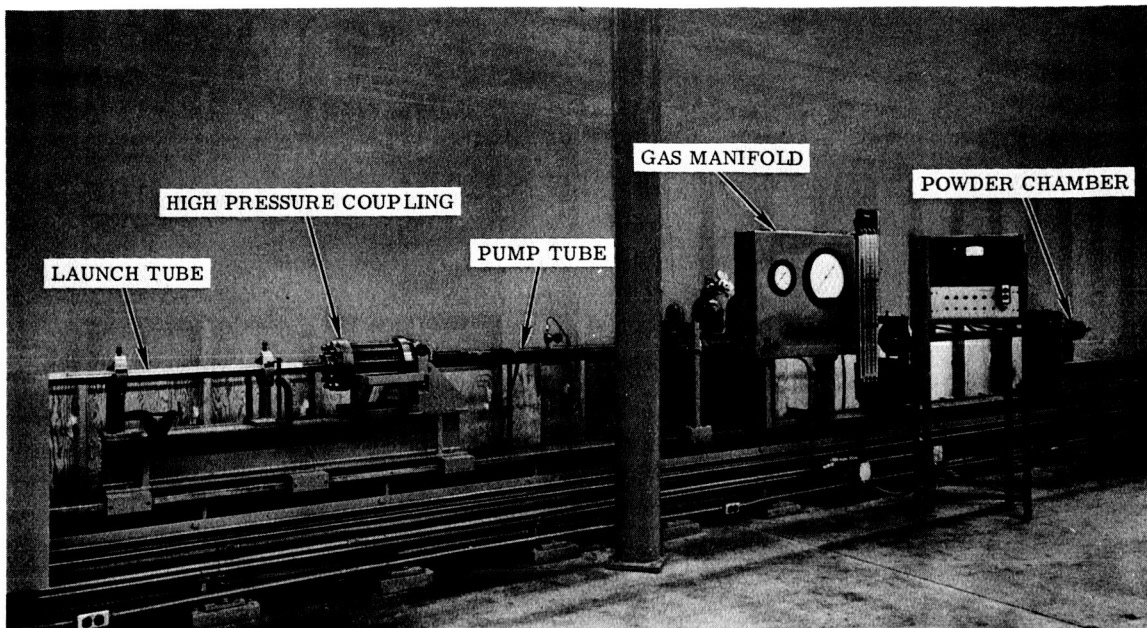
Figure C-1   Impact Range D, .30-Caliber ARLG Gun
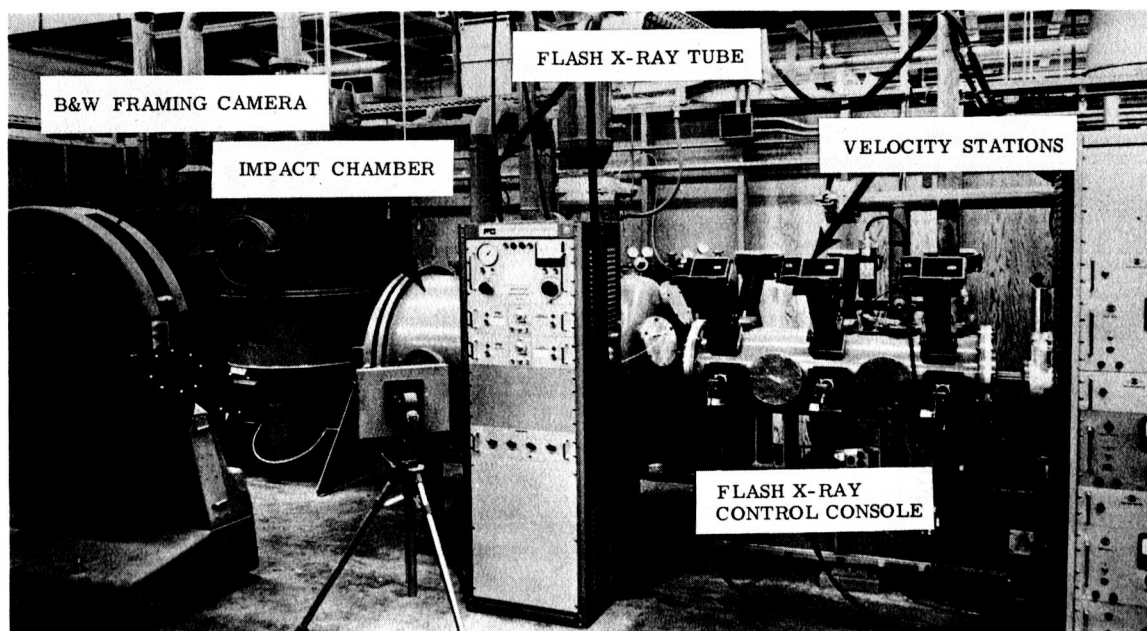
Figure C-2   Impact Range D, Free-Flight and Impact Section

0.30 - In. AR-LG GUN
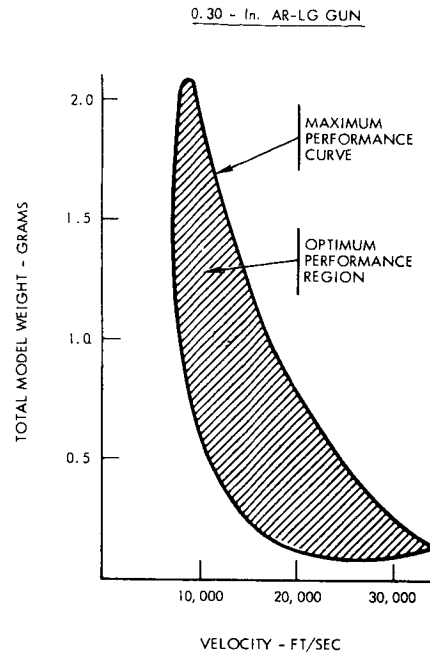
Figure C-3   Performance Characteristics, Impact Range D
with 0. 30-Caliber Launch Tube

The ranges are oriented in such a way that the flight axis is generally north
to south, so the optical planes for the shadowgraph stations are east to west.
Accordingly, Polaroid cameras mounted at the end of each optical axis are
referred to as East and West Cameras, and an "E" or a "W" on the shadow-
graphs identifies the cameras.

Figure C-4 indicates the geometric arrangement of the shadowgraph stations
used on the ranges.

GM DEFENSE RESEARCH LABORATORIES ⊗ GENERAL MOTORS CORPORATION

TR64-48
APPENDIX C
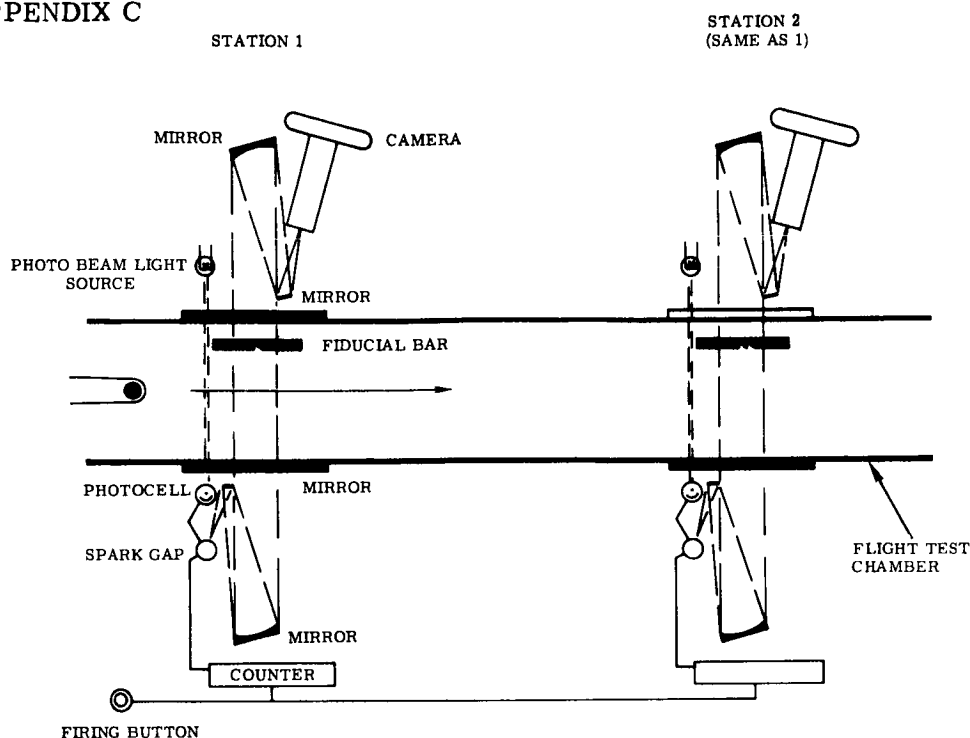
Figure C-4 Schematic of Velocity Station Instrumentation
on Flight Physics Range

Shadowgraph photographs are taken by means of spark-gap light sources triggered by the passage of the model. As the model travels downrange, it itercepts a light beam across the flight path at the shadowgraph station. The light beam intensity is attenuated by the model and this change is detected by a photocell and used to trigger the spark-gap light source for the station (East and West). The distance along the flight path is indicated by reference fiducial marks at each of the camera stations (Figure C-5).
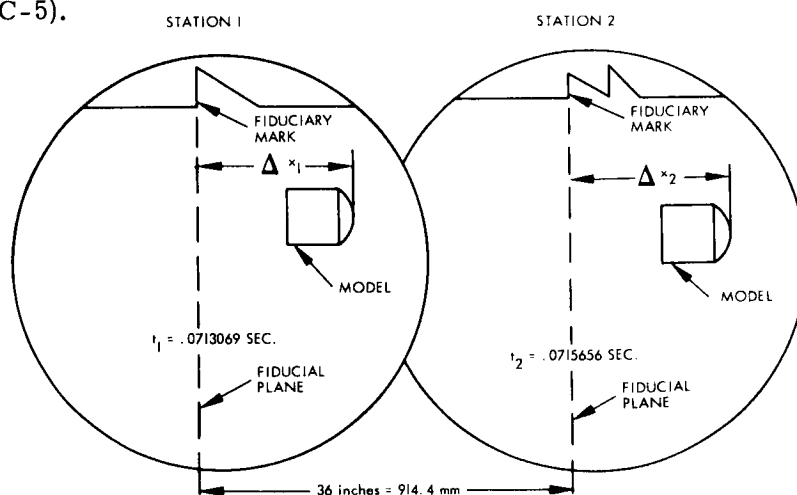
Figure C-5 Sketches of Typical Spark Photographs of Blunt-
Nosed Model

C-4

A relative time-history of the model's flight is determined by use of electronic counters, a 10-megacycle Beckman counter comprising a basic part of each of the shadowgraph systems. The counters for all of the shadowgraph systems are started by the firing pulse of the gun launching the model, and each counter is stopped individually by the current discharge of the spark-gap light source. Thus, the counters are started at the same instant and stopped individually by the light source for the photograph of the model. In this way, time counts corresponding to each shadowgraph are obtained and an absolute relative time- and position-history of each flight is recorded; the velocity of the model can then be computed by time and distance differences.

3. DIAGNOSTIC EQUIPMENT

The phenomena associated with the impact of a hypervelocity projectile on a target occur over a very short time span — normally less than 100 microseconds; consequently, the instrumentation is designed for the most part to obtain time-resolved records which may be analyzed after a test.

High-Speed Framing Camera

A Beckman-Whitley Model 192 continuous-writing framing camera is used to record photographically the phenomena associated with impact on both solid and thin targets. The camera is shown at the left in the photograph of Range D, Figure C-2. This recently developed instrument has the unique capability of achieving framing rates as high as 1.4 million frames per second. Figure C-6, a schematic of the optical system, and Figure C-7, a photograph of the interior of the camera, illustrate the complexity of the camera, which contains over 400 optical components.
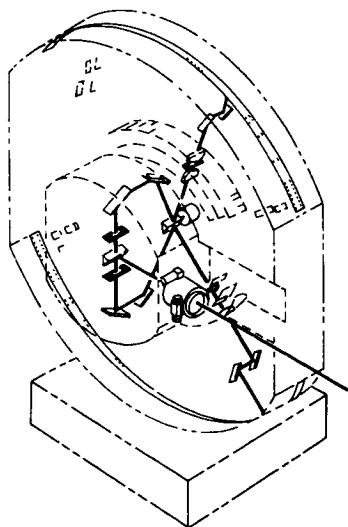
Figure C-6 Optical System Schematic
of High-Speed Framing
Camera
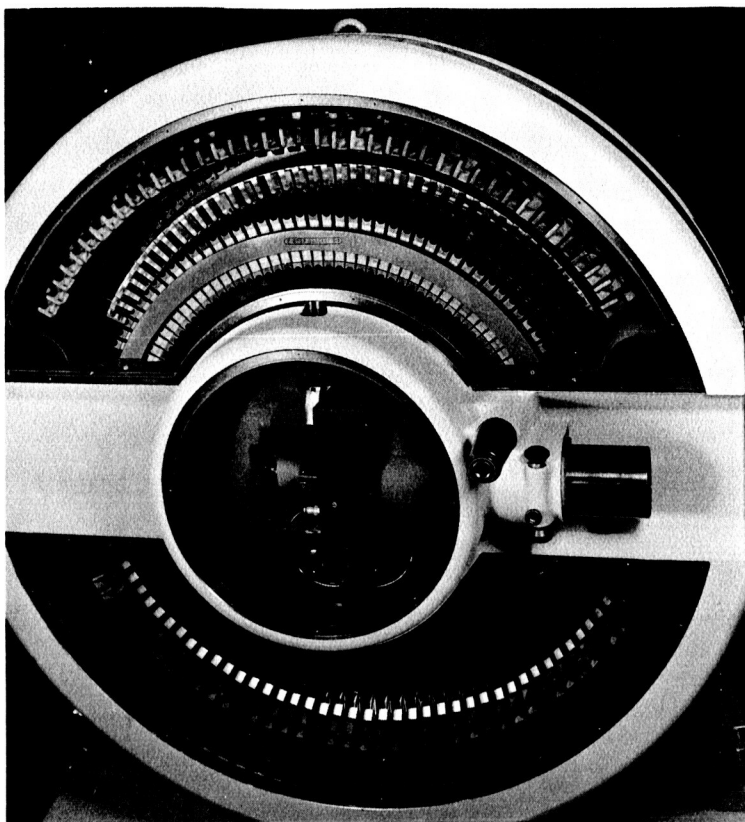
Figure C-7   High-Speed Framing Camera Lens System

The operational characteristics of this camera are listed below:

Number of frames	-	82
Frame size	-	17 x 25 mm
Frame rate	-	up to 1.4 million frames per second
Aperture	-	at the film f/26
Resolution	-	dependent on film used, but between 20 − 24 lines/mm
Optical distortion	-	less than 1%
Exposure time	-	dependent on frame rate; 0.1μ sec at 1.4 million frames per second
Writing time	-	55 μ sec at maximum framing rate

The Beckman-Whitley camera is operated remotely from a control panel in the range control room. Framing rate is adjusted pneumatically, and the turbine speed is monitored on an electronic counter which receives signals from magnetic pickups on the turbine.

Since the camera is continuous writing, rewrite can occur if measures are not taken to prevent it. The light source used is an exploding bridgewire which is mounted at the focal point of a 6-1/2 in.-diameter plano-convex lens. Adequate light intensity is obtained over the entire range of framing rates, and the problem of rewrite is minimized by proper timing of the pulse which fires the exploding wire. The light source can be triggered by a photobeam or through the use of a "Pre-Impact Computer".

The Pre-Impact Computer is a transistorized, digital-computer device that operates in the following manner:

(1) The actual elapsed time for the projectile to travel between adjacent velocity stations is fed into the computer from the velocity station photocell amplifiers.

(2) Since the distance between the velocity stations is predetermined and fixed, the computer can calculate actual projectile velocity.

(3) Since, for any given shot, the distance from velocity station to target and the point at which trigger of the light source is required are known and can be preset into the computer, the velocity calculated in (2) can be applied to this distance to obtain a delay time.

(4) After the delay time calculated in (3) has elapsed, the computer triggers the light source.

The entire sequence outlined above, (1) through (4), normally takes place in less than 200 microseconds. Since use of the Pre-Impact Computer permits timing on the basis of actual velocity rather than estimated velocity, there is no chance of missing observation of an impact when actual velocity differs from expected velocity.

TR64-48
APPENDIX C

Multi-Flash X-Ray Unit

Since internal crater dimensions, very fine debris, and dust are opaque to the
framing camera, it is desirable to have other means of observing discrete
ejecta particles that may be obscured by this fine debris or dust. This can be
accomplished with a multi-flash X-ray unit, which is also capable of observing
crater growth in thick targets. The four-channel X-ray unit (see Figure C-2)
available at GM DRL has a flash duration of 0.07 microseconds.

The Pre-Impact Computer previously described can also be used with the
multi-flash X-ray unit, with the computer triggering the X-ray tube instead
of a light source.

GM Defense Research Laboratories, General Motors Corp., Santa Barbara, California SUMMARY REPORT OF RESEARCH ON THE PROPERTIES OF OPTIMUM METEOROID SHIELDS by C. L. Meyers, J. A. Charest, J. W. Gehring, and C. J. Maiden; TR64-48, September 1964, prepared for George C. Marshall Space Flight Center under Contract No. NAS8-11118; 106 pp. inc. 38 illus., 14 tbls., 35 refs.

Unclassified Report

This report describes experimental studies on the measurement of shock-pressure maximum amplitudes, on the measurement of momentum transfer, and on a phenomenological model of crater formation. This model is divided into four regimes of cratering: 1) the initial transient regime,

(Unclassified)

1. Meteors – Physical effects
2. Blast effects – Cratering
3. Impact shock – Measurement
4. Hypervelocity projectiles – Test results

I. NAS8-11118
II. TR64-48
III. Meyers, C. L.
IV. Charest, J. A.
V. Gehring, J. W.
VI. Maiden, C. J.

(Descriptors) Space environmental conditions,

Cratering, Penetration,
Fragmentation, Shockwaves,
Meteors, Models (simu-
lations), Metallography,
Projectiles, Impact flash,
Terminal ballistics.

including impact flash; 2) the primary pene-
tration regime; 3) the cavitation regime; and
lastly, the recovery regime, including surface
spallation and release of pressure on the
crater walls. Detailed experimental data are
presented covering the last three of the four
regimes described above; in each case the
data are directly related to the extent to which
it contributes to the cratering process and to
the relationship of this portion of the pheno-
mena to theoretical models of impact crater-
ing. The experimental results are organized
into three separate discussions of the principal
topical areas studied: shock-pressure meas-
urements; momentum-transfer (with mass-
loss) measurements; and crater-growth meas-
urements. In addition, the materials (physical
mechanical and metallurgical properties) and
the experimental equipment used are de-
scribed in appendixes to the report.

including impact flash; 2) the primary pene-
tration regime; 3) the cavitation regime; and
lastly, the recovery regime, including surface
spallation and release of pressure on the
crater walls. Detailed experimental data are
presented covering the last three of the four
regimes described above; in each case the
data are directly related to the extent to which
it contributes to the cratering process and to
the relationship of this portion of the pheno-
mena to theoretical models of impact crater-
ing. The experimental results are organized
into three separate discussions of the principal
topical areas studied: shock-pressure meas-
urements; momentum-transfer (with mass-
loss) measurements; and crater-growth meas-
urements. In addition, the materials (physical
mechanical and metallurgical properties) and
the experimental equipment used are de-
scribed in appendixes to the report.

Cratering, Penetration,
Fragmentation, Shockwaves,
Meteors, Models (simu-
lations), Metallography,
Projectiles, Impact flash,
Terminal ballistics.

Cratering, Penetration,
Fragmentation, Shockwaves,
Meteors, Models (simu-
lations), Metallography,
Projectiles, Impact flash,
Terminal ballistics.

including impact flash; 2) the primary pene-
tration regime; 3) the cavitation regime; and
lastly, the recovery regime, including surface
spallation and release of pressure on the
crater walls. Detailed experimental data are
presented covering the last three of the four
regimes described above; in each case the
data are directly related to the extent to which
it contributes to the cratering process and to
the relationship of this portion of the pheno-
mena to theoretical models of impact crater-
ing. The experimental results are organized
into three separate discussions of the principal
topical areas studied: shock-pressure meas-
urements; momentum-transfer (with mass-
loss) measurements; and crater-growth meas-
urements. In addition, the materials (physical
mechanical and metallurgical properties) and
the experimental equipment used are de-
scribed in appendixes to the report.

including impact flash; 2) the primary pene-
tration regime; 3) the cavitation regime; and
lastly, the recovery regime, including surface
spallation and release of pressure on the
crater walls. Detailed experimental data are
presented covering the last three of the four
regimes described above; in each case the
data are directly related to the extent to which
it contributes to the cratering process and to
the relationship of this portion of the pheno-
mena to theoretical models of impact crater-
ing. The experimental results are organized
into three separate discussions of the principal
topical areas studied: shock-pressure meas-
urements; momentum-transfer (with mass-
loss) measurements; and crater-growth meas-
urements. In addition, the materials (physical
mechanical and metallurgical properties) and
the experimental equipment used are de-
scribed in appendixes to the report.

Cratering, Penetration, Fragmentation, Shockwaves, Meteors, Models (simulations), Metallography, Projectiles, Impact flash, Terminal ballistics.

including impact flash; 2) the primary penetration regime; 3) the cavitation regime; and lastly, the recovery regime, including surface spallation and release of pressure on the crater walls. Detailed experimental data are presented covering the last three of the four regimes described above; in each case the data are directly related to the extent to which it contributes to the cratering process and to the relationship of this portion of the phenomena to theoretical models of impact cratering. The experimental results are organized into three separate discussions of the principal topical areas studied: shock-pressure measurements; momentum-transfer (with mass-loss) measurements; and crater-growth measurements. In addition, the materials (physical mechanical and metallurgical properties) and the experimental equipment used are described in appendixes to the report.

Cratering, Penetration, Fragmentation, Shockwaves, Meteors, Models (simulations), Metallography, Projectiles, Impact flash, Terminal ballistics.